A STUDY OF SLIPPER AND RAIL WEAR INTERACTION AT LOW SPEED

THESIS

Greg V. Cavallaro, Major, USAF

AFIT-ENY-T-14-J-31

DEPARTMENT OF THE AIR FORCE
AIR UNIVERSITY

AIR FORCE INSTITUTE OF TECHNOLOGY

Wright-Patterson Air Force Base, Ohio

The views expressed in this thesis are those of the author and do not reflect the official policy or position of the United States Air Force, the Department of Defense, or the United States Government.

AFIT-ENY-T-14-J-31

A STUDY OF SLIPPER AND RAIL WEAR INTERACTION AT LOW SPEED

THESIS

Presented to the Faculty

Department of Aeronautical Engineering

Graduate School of Engineering and Management

Air Force Institute of Technology

Air University

Air Education and Training Command

in Partial Fulfillment of the Requirements for the

Degree of Master of Science in Aeronautical Engineering

Greg V. Cavallaro, B.S.A.E.

Major, USAF

June 2014

AFIT-ENY-T-14-J-31

A STUDY OF SLIPPER AND RAIL WEAR INTERACTION AT LOW SPEED

Greg V. Cavallaro, B.S.A.E.
Major, USAF

Approved:

//signed//	27 May 2014
Anthony N. Palazoto, PhD (Chairman)	Date
//signed//	30 May 2014
William P. Baker, PhD (Member)	Date
//signed//	30 May 2014
Rodolfo G. Buentello-Hernandez, PhD (Member)	Date

AFIT-ENY-T-14-J-31

Abstract

The wear research presented in the work consists of results gathered from utilizing a 3-D ABAQUS model of a slipper and rail system based on a Holloman High Speed Test Track mission executed in January 2008. The system consists of a VascoMax slipper in contact with a AISI-1080 steel rail. The slipper is slid along the rail at speeds of $20\,\mathrm{m\,s^{-1}}$ and $40\,\mathrm{m\,s^{-1}}$ with complementary vertical velocities of $-0.079\,\mathrm{m\,s^{-1}}$ and $-0.059\,\mathrm{m\,s^{-1}}$, respectively. The surface roughness caused by features such as asperities and valleys of the materials, is simulated in this model by five asperities, $1\,\mu\mathrm{m}$ to $5\,\mu\mathrm{m}$ on the rail and a slipper with a leading edge radius of $6\,\mu\mathrm{m}$. The free space between the surfaces, caused by the interaction of the asperities and valleys, is approximated by three gap spacings of $0.5\,\mu\mathrm{m}$, $1.0\,\mu\mathrm{m}$, and $1.5\,\mu\mathrm{m}$. This study also explores three different mesh sizes in the wearing portion of slipper to uncover any mesh dependency on the amount of wear. In addition to the eighteen simulations encompassed by two speed increments, three mesh refinements, and three gap spacings, an additional group of nine simulations were completed at the $40\,\mathrm{m\,s^{-1}}$ speed. Six simulations were used to highlight the effects of more accurate material definitions such as tables of specific heat capacities instead of static values, more applicable lower strain rate Johnson Cook plasticity parameters in place of the high strain rate parameters, and then applying both updates together in the same model. This was done for two mesh refinements. Finally, three more simulations with the fine mesh were carried out containing filleted asperity blocks. Instead of the asperity hemispheres meeting the rail at a right angle, the two are joined by a $1\,\mu\mathrm{m}$ fillet. These results were compared to the original model not using asperity fillets. The goal of this research is not only to validate and improve a 3-D wear model, but to also bracket the amount of wear for a slipper and rail system for the low speed regime.

Acknowledgments

First, I would like to thank my Lord and Savior Yeshua Messiah for watching over my family and I during this demanding season in my life. I would also like to thank Him for strengthening and enabling me to complete this research. With Elohim all things are possible. I would also like to thank my wife who has had to shoulder the the lion's share of the day to day requirements of taking care of the boys, a house and a dog and for not getting discouraged. I pray that they will learn as I have how important it is to ensure Yahovah, El Shaddai, the Elohim of Avraham, the Elohim of Yitzchak, and the Elohim of Yaakov is placed above all. I would also like to thank my kids for being understanding and not getting angry when "daddy was gone so much". I would also like to sincerely thank my advisor Distinguished Professor Dr. Anthony N. Palazotto for his encouragement, invaluable contributions, mentorship and tireless work ethic through this journey. His dedication to higher education is matchless. There wasn't a day that went by where he did not make himself available for questions, comments or help. I wanted to thank Dr. William Baker for reviewing my research and writing only making it better. Thank you for being on my committee, for your patience and interesting ideas. This work would not have been possible without the support and documentation provided by Major Dr. Rodolfo G. Buentello Hernandez the creator of the original wear model. Thank you for your time and for answering the modicum of my inane Abaqus questions. My prayer for these three gentlemen, their families and extended families is that the Elohim, El Shaddai will bless and protect them, that His provision will be upon them. I also pray that they will receive an incredible understanding of who He is and how much He loves each and everyone of us.

Greg V. Cavallaro

Table of Contents

Page

List of Figures

List of Tables

List of Symbols

V_{SA-r-v}	Definition
A	Initial Yield Stress (Pa)
B	Strain Hardening Coefficient (Pa)
c_0	Mie-Grüneisen Material Parameter ($\mathrm{km\,s^{-1}}$)
C	Strain Rate Coefficient
C_P	Specific Heat Capacity ($\mathrm{J\,g^{-1}\,K^{-1}}$)
$d_1 - d_5$	Johnson Cook Fracture Model Coefficients
D	Damage
D_s	Distance Slid (mm)
E	Young's Modulus (Pa)
E_m	Internal Energy Per Unit Mass ($\mathrm{J\,kg^{-1}}$)
F_f	Force of Friction (N)
F_N	Normal Force (N)
$\tilde{F}$	Normalized Pressure ($\mathrm{N/m^2/N/m^2}$)
l_c	Length of Contact Area (mm)
r	Radius of Asperity (μm)
s	Mie-Grüneisen Material Parameter
T	Material Temperature (K)
T_0	Reference Temperature (K)
T_{melt}	Melt Temperature (K)
T_{room}	Room Temperature (K)
T^*	Homologous Temperature (K/K)
U_s	Shock Velocity ($\mathrm{m\,s^{-1}}$)
U_p	Particle Velocity ($\mathrm{m\,s^{-1}}$)

V_{SA-r-v}	Definition
v	Velocity ($\mathrm{m\,s^{-1}}$)
V_{d-v}	Interval Wear for Distance Slid ($\mathrm{mm^3}$)
V_{SA-r-v}	Simulate Wear Volume For Asperity Radius, r and Velocity, v ($\mathrm{mm^3}$)
V_{uA-v}	Wear Volume Per Unit Area, A, for Velocity v ($\mathrm{mm^3/mm^2}$)
$\tilde{v}$	Normalized Velocity ($\mathrm{m\,s^{-1}/m\,s^{-1}}$)
w_c	Width of Contact Area (mm)
W_{uA}	Normalized Wear Volume ($\mathrm{mm^3/mm^3}$)
$\#Asp_{uA}$	Number of Asperities Per Unit Area, A ($\mathrm{\#/mm^2}$)
$\%Asp_r$	Percent of Asperities of Size, r, For a Unit Area (%)
$\%Cont_v$	Percent Contact For Velocity, v (%)

Greek Symbols

Γ_0	Mie-Grüneisen Material Parameter
δt	Time Increment (s)
$\dot{\varepsilon}$	Strain rate ($\mathrm{s^{-1}}$)
$\dot{\varepsilon}^*$	Dimensionless Johnson Cook Strain rate (/s//s)
$\bar{\varepsilon}^P$	Accumulated Plastic Strain (m/m)
$\bar{\varepsilon}_0$	Reference Strain Rate ($\mathrm{s^{-1}}$)
η	Nominal Volumetric Compressive Strain ($\mathrm{s^{-1}}$)
μ	Coefficient of Friction
ν	Poisson Ratio
π	Pi
ρ	Density ($\mathrm{kg\,m^{-3}}$)
ρ_0	Reference Density ($\mathrm{kg\,m^{-3}}$)
σ_{eq}	Equivalent Stress (Pa)

V_{SA-r-v}	Definition
σ_m	Average of Three Normal Stresses (Pa)
$\bar{\sigma}$	Von Mises Equivalent Stress (Pa/Pa)
σ^*	Johnson Cook Pressure-Stress Ratio (Pa/Pa)
$\dot{\sigma}^*$	Johnson Cook Dimensionless Strain Rate (Pa)

Subscripts

r	Radius of Asperity (μm)

Superscripts

n	Johnson Cook Strain Hardening Exponent
m	Johnson Cook Thermal Softening Exponent

List of Acronyms

Acronym	Definition
BC	boundary condition
B-H	Buentello Hernandez
CTH	Coupled Hydrodynamics and Radiation Transport Diffusion
DADS	Dynamic Analysis of Dynamic Systems
EOS	Equation of State
FEM	finite element model
HHSTT	Holloman High Speed Test Track
JC	Johnson Cook

A STUDY OF SLIPPER AND RAIL WEAR INTERACTION AT LOW SPEED

I. Introduction

1.1 Background and Motivation

THE objective of this research is to adapt a high speed mechanical wear model created by B-H[30] for use at speeds of $20\,\mathrm{m\,s^{-1}}$ and $40\,\mathrm{m\,s^{-1}}$. The model created by B-H is based on the refined Dynamic Analysis of Dynamic Systems (DADS) data obtained during the January 2008 Holloman High Speed Test Track (HHSTT) rocket sled mission. The raw data obtained from "sled borne" instrumentation, such as accelerometers and angular rate sensors are processed using DADS and the raw data is filtered with the end result being a digital model sled performance for that sled run. The DADS output includes test times, contact forces, contact time, displacement, velocities and accelerations[11]. From this mission, a VascoMax 300 slipper was recovered from stage three for wear research. The results of this modeling effort are compared to experimental wear data such as that compiled by Lim and Ashby[23] in their 'wear map' research as well the simulated wear data computed by B-H[30] with his high speed wear model.

1.2 Holloman High Speed Test Track

The HHSTT, a Major Test Range Facility Base, is one of America's premier test facilities. The "Track" has been around since the 1950s and has only become more capable and critical test facility ever since. High Speed testing, up to Mach 10, is undertaken at the Track at about 10% the cost[13] of comparable flight testing. The Track's test facility is a 10 mile long rail used for various testing activities such as egress (ejection seats/system components), munition dispense (from bombs or aircraft bays), guidance and

navigation, rain field and impact (bunker busters/kinetic kill). Sleds or “sled trains”are thrusted “downtrack” by means of rocket motors and are constrained to the rail by slippers. In the image below of the 2008 “Sled Train“, stages one through four can be seen, with stage one on the left[30].

Figure 1.1: Hypersonic Mission Sled Train

Slippers wrap around the rail allowing the sleds to slide downtrack but not depart vertically or laterally. Below is an image of a VascoMax 300 slipper from the Track’s 2008 hypersonic mission. It can be seen how the slipper wraps around the rail. The slipper gap can also be seen between the rail and the flange of the slipper. This gap allows the slipper to traverse any irregularities it may encounter along the rail; reducing unnecessary loads in the sled. Since there is a gap, the sled is free to float vertically and laterally, a few millimeters, under the various loads to which the sled is subjected. By allowing the sled to bounce, impact forces are generated between the slipper and rail. At high speeds, these impacts induce collisions between asperities in the rail and slipper potentially wearing out the slipper.

A slipper experiencing excessive wear could potentially ruin a multi-million dollar test mission, destroy one-of-a-kind test articles and jeopardize the lives of personnel; as a worn slipper could allow the sled to depart the rail careening off into the desert in a

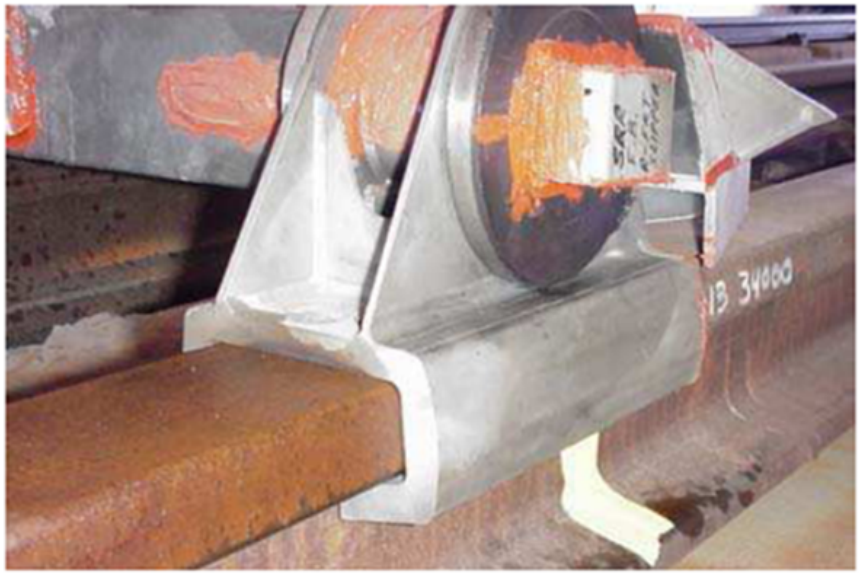

Figure 1.2: VascoMax300 Slipper[14]

remarkable display of rapid unplanned disassembly. Understanding and combating wear is of great import to the Track. Wear even at low speeds is important for many other fields and industries as well. Ensuring accurate modeling and simulation of wear at the lower speed regimes is potentially more difficult than at high speeds. The lower speeds directly relate to lower strains and strain rates and longer model run times. The longer run times can, if not modeled correctly, cause a propagation of errors from integration point to integration point causing model instabilities or complete inaccuracies in results.

1.3 Brief Wear History

The study of wear or tribology grew out of the field of friction research. Many people throughout history have sought out ways to limit or remove the damaging effects of friction between surfaces that are in contact and sliding against each other. Ancient drills fashioned with antler or bone bearings were used with bows to drill holes or to create fire with tinder[6]. In a fresco from 1880 BC shown by[6] over 170 Egyptian slaves are

depicted dragging a large stone statue into place on sleds with men pouring lubricants under the sled as it moves. The use of lubricants was found even before the previous statue example, as an Egyptian tomb dated at 3000 BC, was discovered containing a chariot with animal fat lubricant still remaining in it's wheel bearings[6]. There are endless examples from antiquity of people trying to mitigate the effects of friction. In the intervening years, the study of friction progressed, Leonardo Di Vinci was credited with studying friction, discovering that the force needed to drag a load across a surface doubled when the mass of the load doubled. He also concluded that the frictional force was not dependent on the area of contact. However, in 1699, Amontons a French scientist published what Da Vinci already studied calling them the the rules of friction. Amontons did make a third distinction from that of Da Vinci, that the friction force is independent of velocity once motion starts, thereby defining static and kinetic friction. Coulomb added to Amontons discovery by noting that kinetic friction does not depend on sliding speed[8]. It wasn't until about 300 years later that micro-scale surface properties were studied by Bowden[7], Tabor[7], and Archard[5] among others.

The industrial revolution of the early 1900s drove the field of Tribology as many machines with a myriad of moving parts containing surfaces that wore against each other, continued to be invented and used. Ensuring that these machines were built to last was of great import. In 1946, Ragnar Holm made the first substantial contributions to the study of wear. "Holm produced the first published account of a mechanism of wear in terms of an atomic transfer process occurring at the real areas of contact formed by plastic deformation of the contacting asperities"[29]. This is generally accepted as the genesis of Tribology. In Holm's work, the surface characteristics of the materials in contact, asperities and valleys, as well as the material's plasticity properties are combined to yield a contact area that is related to the ratio of load to yield pressure of the material. The concept of wear is first attributed to Holm. Bowden and Tabor followed up Holm's work.

In 1950, Bowden and Tabor published their theory of friction called 'plastic junction'. In their theory they propose that "the real area of contact between two surfaces is very small, and as a consequence, the contact pressure at those asperities in contact is very high. This results in plastic deformation of the asperities during contact so the real area of contact...can be calculated from the material's indention hardness value"[9].

In 1952, Burwell and Strang[19] came to the conclusion that the wear rate of materials in contact is proportional to the applied load and wear rate is independent of the apparent (geometric) area of contact. They also proposed that the average size of the individual contact areas is constant while the number of contact areas increases with increasing load[29] and valleys, the material hardness, and the loading situation all contribute greatly to the wear of materials in contact. Many researchers from Holm to Bowden to Tabor and others all recognize the fact that, at the micro-scale, the asperities drive the frictional response via visco-plasticity, and as Wedberg states "...materials exhibit different strain hardening and softening characteristics at different strains, strain rates, and temperatures."[32]. Combining all of these properties are important to successfully model wear.

Many researchers have proposed analytical models where single asperities contact a surface. Mishra et Al[25] in 2012 propose a nano-scale model based on molecular dynamics simulations to uncover the wear properties of adhesion at a speed of $150\,\mathrm{nm\,s^{-1}}$. In 2004, Cha et Al[28] showcased their research on a nano-scale asperity model. In 1997, K. L.. Johnson reported on his nanotribological research, again a nano scale model of a single asperity contacting a surface. These models all have one thing in common, the ultra small scale at low speeds. They all look at material interactions at the atomic level, where as this modeling effort is focused at the micro-scale level at a somewhat higher speed level.

1.4 Air Force Institute of Technology Wear Research

In 2007, Cameron[10] led the way with a two pronged assault on the problem of wear. The first technique adapted the analytical model developed by Lim and Ashby in their 1987 work. Cameron applied normalized DADS data to the model to develop a wear volume and a wear rate for the HHSTT scenario. Since the Lim and Ashby model was based on the 1976 wear research performed by Montgomery[27], in which a range of speeds, pressures and sliding distances were investigated, the applicability to the HHSTT scenario seemed appropriate. Appropriate in the fact that the sled slippers experience multiple speed regimes, pressures, and sliding distances throughout a sled run. Cameron[10] also developed a numerical model utilizing the Hydrocode: Coupled Hydrodynamics and Radiation Transport Diffusion (CTH) developed by Sandia National Laboratories. This technique adapted a plane strain-2D CTH model developed by Laird[21] in 2002, modifying it by applying the sleds speeds, vertical and horizontal, and downward forces given in the DADS data. What Cameron found is that the CTH model did not produce melt wear, since the slipper temperature never reached the melting temperature of VascoMax. However, the Lim and Ashby model did produce the melt wear for the entire sled run. Cameron concluded that there is indeed melt wear happening and that the CTH model would need the actual vertical velocities to possibly account for the melt wear, not just an average downward velocity for the whole sled run.

In 2009, Hale[11] developed a 2D plane strain Abaqus model to evaluate mechanical wear rates continuing this HHSTT wear research. Hale's model included three semicircular asperity sizes of 2 μm, 4 μm, and 6 μm in an attempt simplifying the 3-D problem into a 2-D problem and then combine the results into a 3-D solution. In the image below, from Hale's work, it can be seen how the asperity was sliced into layers.

In this approach, a slipper with no gap under it impacted the asperity on the rail. The resulting stress levels were used to determine the extent of damage as compared to the

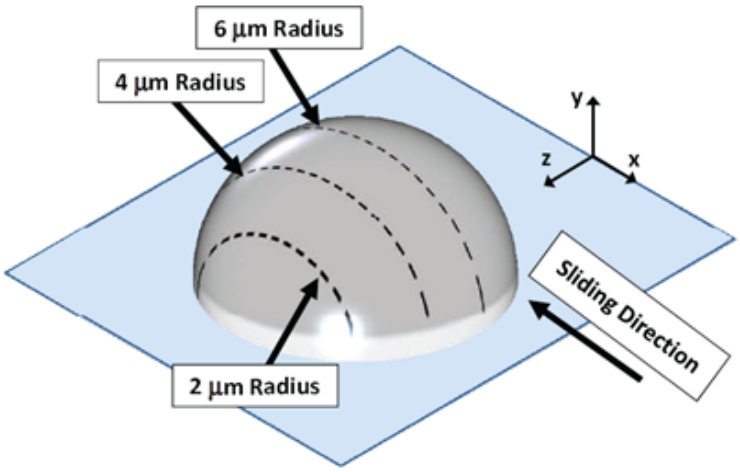

Figure 1.3: Hale Asperity

maximum Von Mises stress. Once the damage results for each layer were collected, they were combined with by applying "three-dimensional proportion factor" calculated by Hale to be 11.77. This factor was used to convert the 2-D results to 3-D, by multiplying the mechanical and melt wear produced numerically by this factor. Below, in the depiction of the model from Hales work, the modeled layers for 2 µm, 4 µm, and 6 µm can be seen with the stress fields in red.

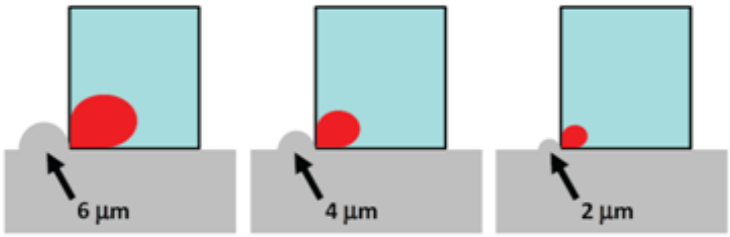

Figure 1.4: Hale Model Depiction

Once the damage for a single asperity was known, the wear rates for that asperity are calculated by dividing the damage by the assumed damage distance, which is 110% of the

asperity size. Since a slipper would in all actuality, impact multiple asperities, Hale utilized a calibrated scaling method that would extrapolate the damage from a single asperity to that of multiple asperities. Hale then multiplied the wear rates by the distance slid for each speed increment. Then added the wear for each increment together to get the total wear. This modeling technique showed roughly 36% of the measured wear as compared to the recovered slipper measurements.

Following Hale's work, B-H[30] using the lessons learned built a 3-D wear model–the basis for this research. In his work, a 3-D model shown below, contained five asperities on the rail, the bottom assembly. The rail asperities sizes are 1 μm, 2 μm, 3 μm, 4 μm, and 5 μm to mimic the findings of Voyiadjis'[31]. The slipper block with five slipper wedges has a leading edge radius of 6 μm again to mimic the average slipper asperity radius 6.1 μm found by Voyiadjis in the same study mentioned earlier. This slipper assembly can be found in Figure 1.5 below. The slipper below has a slipper block (light blue top) and slipper wedges (under slipper block). The slipper block has a coarse mesh applied to it while the wedges have a much finer mesh to register the wear as it develops.

Figure 1.5: B-H Slipper Assembly

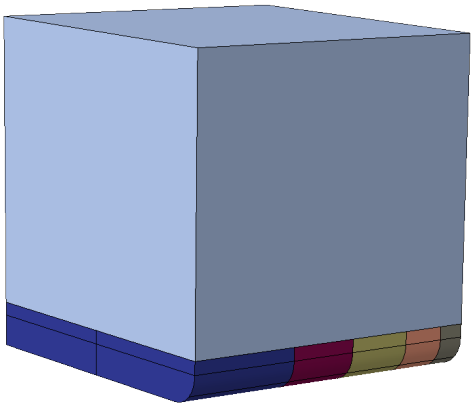

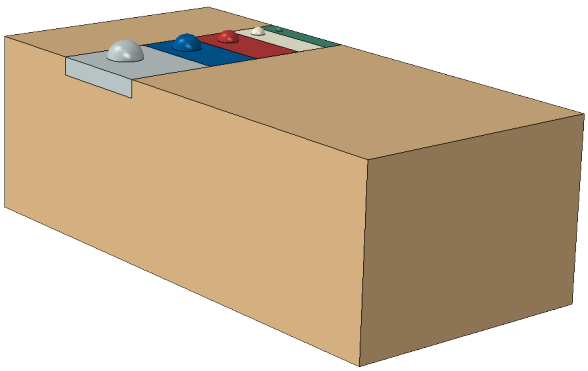

Figure 1.6: B-H Rail Assembly

The rail assembly above has a rail block (tan bottom) and asperity blocks set into the rail block. The rail block has a coarse mesh, much like the slipper block, and the asperity blocks have a much finer mesh. The asperities are designed to impact the slipper wedges, damaging themselves in the process.

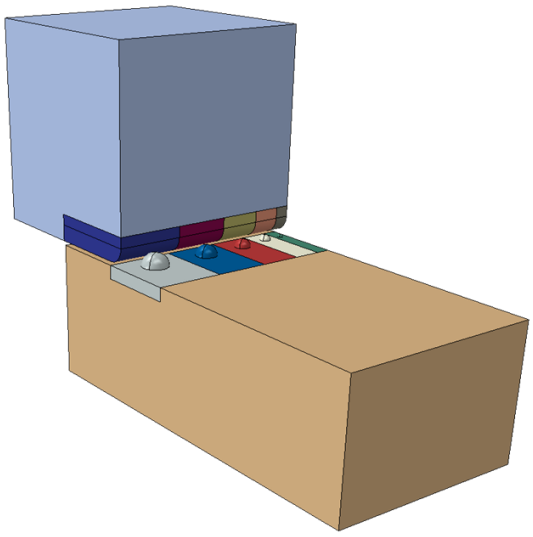

Figure 1.7: B-H Model Assembly

Figure 1.7 above, is the model assembly containing the rail assembly and the slipper assembly. This model includes Johnson Cook (JC) plasticity and fracture dynamics, Coulomb friction model with a Montgomery friction coefficient in the general contact algorithm, and the Mie-Grüneisen equation of state to govern the material's behavior during shock compression. The model is run at speed increments based on the HHSTT 2008 mission. The sled mission is divided into 100 m s^{-1} increments. The model sets the slipper in motion at a prescribed speed and impacts it into the asperities on the immovable rail. The impact damages both the asperities and the slipper wedges. This wear is tabulated from damaged elements within the slipper wedges. For each slipper wedge, the original volumes of the failed elements is summed, yielding the wear volume per wedge due an asperity. The wear volume for a specific speed increment, for a specific asperity size is multiplied with, the number of asperities per square millimeter, the percentage of that asperity size in the distribution and the outcome for all five asperities is summed up. This yields a normalized wear in mm^3/mm^3. This result is then multiplied by the distance slid, D_s, the wear contact area under the slipper, and the percent contact for that speed increment. The figure below shows this wear calculation for a 25 m s^{-1} simulation.

The wear for each speed increment or wear interval is summed up to yield the slipper wear for the entire sled run. Since the specific heat capacity for VascoMax 300 at high temperature is not known, B-H assumed that the specific heat capacity for VascoMax 300 is the same as AISI-1080 steel at high temperatures. This analysis yielded total wear volumes of 16 623 mm^3 for the low temperature VascoMax 300 C_P = 4.5 mm^2 /Ks^2 and 13 635 mm^3 for the high temperature C_P = 7.0 mm^2 /Ks^2. These results are roughly 22.5% and 12.9% higher than the wear volume measured on the recovered slipper. These wear numbers calculated are well in the ballpark as far as modeling and simulation is concerned. It is because of the accuracy of this model that it was assumed to be a good tool to start with for a low to medium speed study.

$$V_{uA-v} = \#Asp_{uA} \sum_{n=1}^{n=5} \%Asp_n V_{SA-n-v}$$

n (µm)	V_{SA-n-v} (mm^3)	#Asp /mm^2	$\%Asp_n$	V_{uA-v} (mm^3/mm^2)
1	0.00E+00	601	25.0%	0.00E+00
2	0.00E+00	601	30.6%	0.00E+00
3	0.00E+00	601	27.8%	0.00E+00
4	2.25E-08	601	11.1%	1.50E-06
5	3.04E-08	601	5.6%	1.02E-06
			Σ V_{uA-v}	2.52E-06
			W_{uA}= 2.5E-06	mm^3/mm^3

Table A-1 Normalized Wear at 25 m/s

$$V_d = \sum_{1}^{v} W_{uA_v} \times l_{c_v} \times w_{c_v} \times D_{s_v} \times \%Cont_v$$

v (m/s)	T (°K)	l_c (mm)	w_c (mm)	D_s (mm)	W_{uA}	%Cont	Interval Wear (mm^3)
25	297	11.1	90	6.E+03	2.52E-06	89.02%	13.9

Figure 1.8: B-H Wear Calculation for 25 m/s[30]

1.5 Wear Experimentation

Many researchers have pain stakenly carried out various empirical pin on disk tests or pin on drum tests. In 1987, S. C. Lim and M. F. Ashby published their work ”Wear-Mechanism Maps”[23]. In this exhaustive work, Lim and Ashby, compiled the emperical results of dozens of researchers to build their ”Wear Maps” of six different kinds of steels, pure iron/low carbon steels, medium carbon steels, high carbon steels, low alloy steels, high alloy steels, and tool steels. They highlighted various schools of wear mechanisms as the data suggested, such as: ultra mild wear, delamination wear, seizure wear, melt wear, severe oxidational wear and adhesive wear. Adhesive wear comprised of three zones: low speed delamination wear, mild oxidational wear, and high speed delamination wear. As

can be seen in the below figure[1] from the Lim and Ashby's more recent work[22], Lim and Ashby have mapped out the various types of wear.

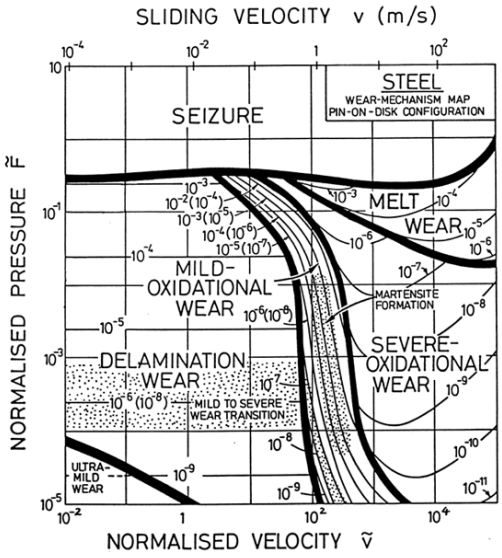

Figure 1.9: Lim and Ashby Wear Map

The purpose of comparing the results of this modeling effort to the Lim and Ashby results are two fold, first this will serve as a validation on the wear rates obtained at low velocities and also define the type wear based on where these results fall on the wear map.

1.6 Thesis Scope

The goal of this research is to add capability and knowledge to the field of finite element modeling of dry mechanical wear in the "medium" speed regime. Where "medium" is defined as above $10\,\mathrm{m\,s^{-1}}$ but below $50\,\mathrm{m\,s^{-1}}$. The original model was designed for high strain-rate interactions at speeds from $0\,\mathrm{m\,s^{-1}}$ to $1500\,\mathrm{m\,s^{-1}}$ and as such, only one set of plasticity parameters were utilized throughout the original study. At the lower speeds for this study, the strain-rates are considerably lower, possibly requiring a

[1]Reprinted from Tribology International, Vol 31/edition number 1-3, S. C. Lim, Recent developments in wear mechanism maps/ Developments in various groups of wear maps, Page No. 90, Copyright (1998), with permission from Elsevier.

different set of JC plasticity parameters for the model. Therefore, a slipper and rail interface will be modeled in ABAQUS incorporating fracture dynamics, visco-plasticity, friction, and shock effects. The original plasticity and specific heat parameters for both materials will be modeled and compared to simulations with updated ones. This will be done by using five hemispherical asperities ranging in size from 1 μm to 5 μm to simulate the surface roughness features of the HHSTT rail as discovered in a study by Voyiadjis et al[31]. Below is a figure highlighting the dominant asperity sizes and their relative distribution from the study.

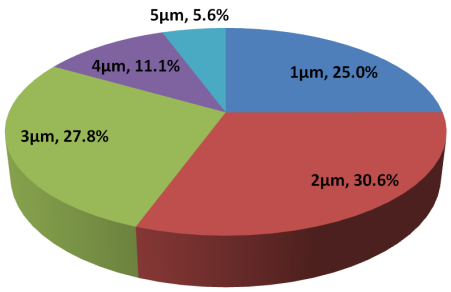

Figure 1.10: Dominant Asperity Sizes in HHSTT Rail

The slipper, comprised of VascoMax300 maraging steel, has a leading edge with a radius of 6 μm, which can be seen in figure below. Since the slipper in this model is plowing through the asperities, and not resting on them at the start of the model, only the leading edge has a radius to mimic the average asperity size of the slipper surface roughness.

This leading edge corresponds to the results shown in the figure below, re-created from a report by Voyiadjis et al[31].

This is done to simulate the average asperity size of the slipper bottom surface also discovered by Voyiadjis et al[31]. To simulate the free space between the slipper and rail due to the roughness coefficient between the two surfaces, various gap spacings from

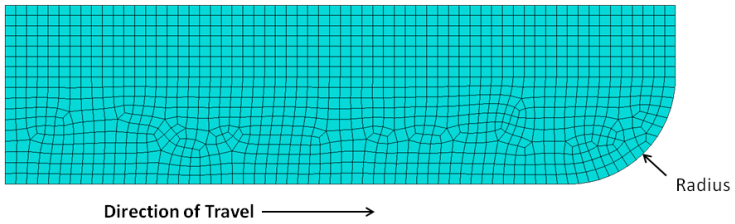

Figure 1.11: Slipper Wedge Leading Edge

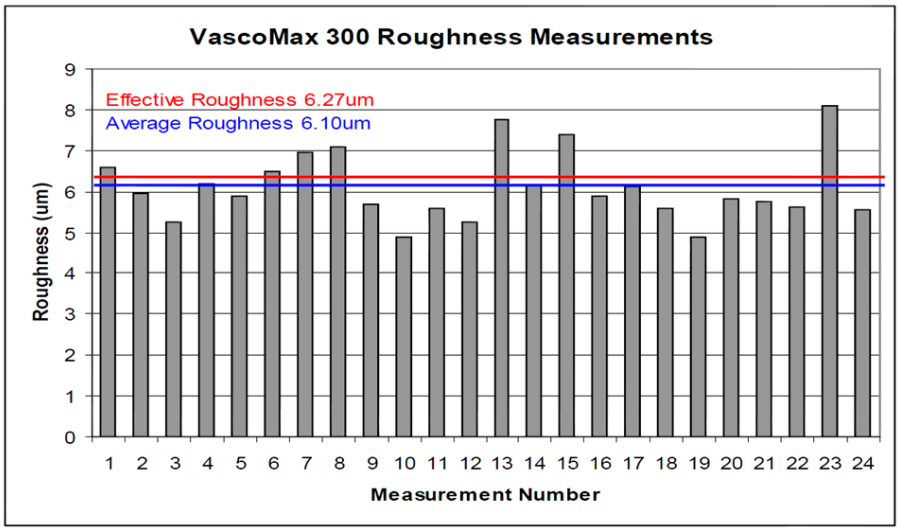

Figure 1.12: VascoMax Roughness[31]

0.5 µm to 1.5 µm will be used. This will also allow for the discovery of the relationship between gap spacing and wear for this HHSTT scenario. A convergence study has also been completed to uncover the influence of element size in the slipper wedges on the evolution of wear volumes and wear rates in the slipper. This study utilized the same finite element that B-H used namely, the linear, explicit C3D8R hexahedral, ”Hex” element with reduced integration.

II. Theory

2.1 Model Characteristics

The Abaqus[1] finite element model (FEM) is used to simulate the collision of a VascoMax 300 slipper with a leading edge of radius 6 μm with a AISI-1080 steel rail with asperities ranging between 1 μm to 5 μm. The collision of the slipper and asperities causes plastic deformation of the materials in contact, which in turn causes localized material heating contributing to material softening and strain induced hardening. The behavior of the modeled materials are governed by the JC plasticity model, the Johnson Cook fracture model, Coulomb friction model and the Mie-Grüneisen Equation of State (EOS). This is done to bring together four basic characteristics that are necessary for modeling wear. They are fracture dynamics, visco-plasticity, friction, and an a relation of pressure, volume and internal energy. The fracture dynamics governs how the material will behave under strain. The visco-plasticity model will capture the plasticity and strain hardening properties of the materials. The frictional model will ensure the modeled materials induce heating and frictional forces to one another. And finally, the equation of state for the materials will also need to be addressed to accurately model the material's behavior during shock interactions and temperature variations. To attempt to truly model wear, at a bare minimum, all the above mentioned characteristics need to be incorporated. In this chapter, these properties of the model will be discussed in detail and the parameters used will be listed. A more complete development related to both the flow equation and the actual failure of an element is presented in the dissertation by B-H[30].

2.1.1 Johnson-Cook Plasticity Model.

In this FEM, the JC plasticity model is used. This model incorporates rate dependent hardening and plastic hardening that is suitable for high strain rate deformation of metals[16]. Below is the equation defining the JC plasticity model equivalent stress. Where

$\bar{\varepsilon}^P$ is the accumulated plastic strain and T^* is the homologous temperature. A (initial yield stress), B (strain hardening coefficient), C (strain rate coefficient), n (strain hardening exponent), and m (thermal softening exponent) are material constants calculated from a limited number of laboratory tests[16].

$$\sigma_{eq} = [A + B \cdot \left(\bar{\varepsilon}^P\right)^n][1 + C \cdot \ln(\dot{\varepsilon}^*)][1 - (T^*)^m] \tag{2.1}$$

$$\dot{\varepsilon}^* = \frac{\dot{\varepsilon}}{\dot{\varepsilon}_0} \tag{2.2}$$

$$T^* = \frac{T - T_{room}}{T_{melt} - T_{room}} \tag{2.3}$$

Equation (2.1) above can be further broken down into three components, the strain hardening term in the left set of square brackets, plastic flow term in the middle set of square brackets, and temperature softening in the right set of square brackets. The first term, gives the stress in terms of strain and captures the strain hardening effects. The second term is the plastic flow term that governs the material plastic behavior after yield has occurred. The last term governs the material softening due to temperature changes. In this equation, it is assumed that elastic stress-strain is separated and expressed by Hooke's law.

The JC model also has a temperature dependence, as can be seen in the last term of equation (2.1). The dimensionless homologous temperature, found above in equation (2.3), is a ratio of differences between the current temperature, the room temperature, and the material melt temperature. This ratio, combined with the thermal softening exponent, captures the modeled stress changes due to thermal softening. Friction causes plastic deformation that causes internal heating. This temperature increase will alter the material behavior through the last term in the Johnson Cook plasticity model. Even though there

may not be global melt wear in a full size slipper, at these speeds, there will undoubtedly be local melt wear or thermal softening at the microscopic level at the asperity interface[24]. This local melting is not handled as a phase change in this model, rather when an element reaches it's melting point, that element is removed from the model based on the JC fracture criteria via the homologous temperature term. So it is important to capture the temperature effects at that contact interface.

Since this model is a function of strain rate, it only makes sense that the parameters used for this model match the strain rates for the given problem. The strain rates in the model were found to be on the order of 10^4 s^{-1} to 10^7 s^{-1}. These strain rates are consistent with the JC damage parameters obtained from Split-Hopkinson bar tests. The original, high strain rate, plasticity parameters were used for this study and compared to simulations utilizing the newer low strain rate plasticity parameters obtained from research done by Cinnamon et al.[15]. The JC plasticity parameters and can be found in the tables below.

Table 2.1: High Strain Rate Johnson-Cook Plasticity Parameters

Material	A (GPa)	B (GPa)	C	m	n	T_m (K)	T_0 (K)
AISI-1080 Steel	0.525	3.59	0.753	0.029	0.67	1670	293
VascoMax 300 Steel	2.17	0.124	0.03	0.8	0.37	1685	293

Table 2.2: Low Strain Rate Johnson-Cook Plasticity Parameters[15]

Material	A (GPa)	B (GPa)	C	m	n	T_m (K)	T_0 (K)
AISI-1080 Steel	0.525	3.59	0.753	0.029	0.668	1670	293
VascoMax 300 Steel	2.17	9.4	0.0046	0.7799	1.175	1685	293

For this FEM research, 293 K is chosen as the initial slipper and rail temperatures for both speed increments. This temperature is based on the research performed by Kathleen Le[20] at AFIT and by Lodygowski et al. Lodygowski's research highlights the fact that for these two materials sliding against one another for up to 0.5 s at 100 m s^{-1} the temperatures remain low on the order of 293 K.

Figure 2.1: Frictional Temperatures of AISI-1080 Steel

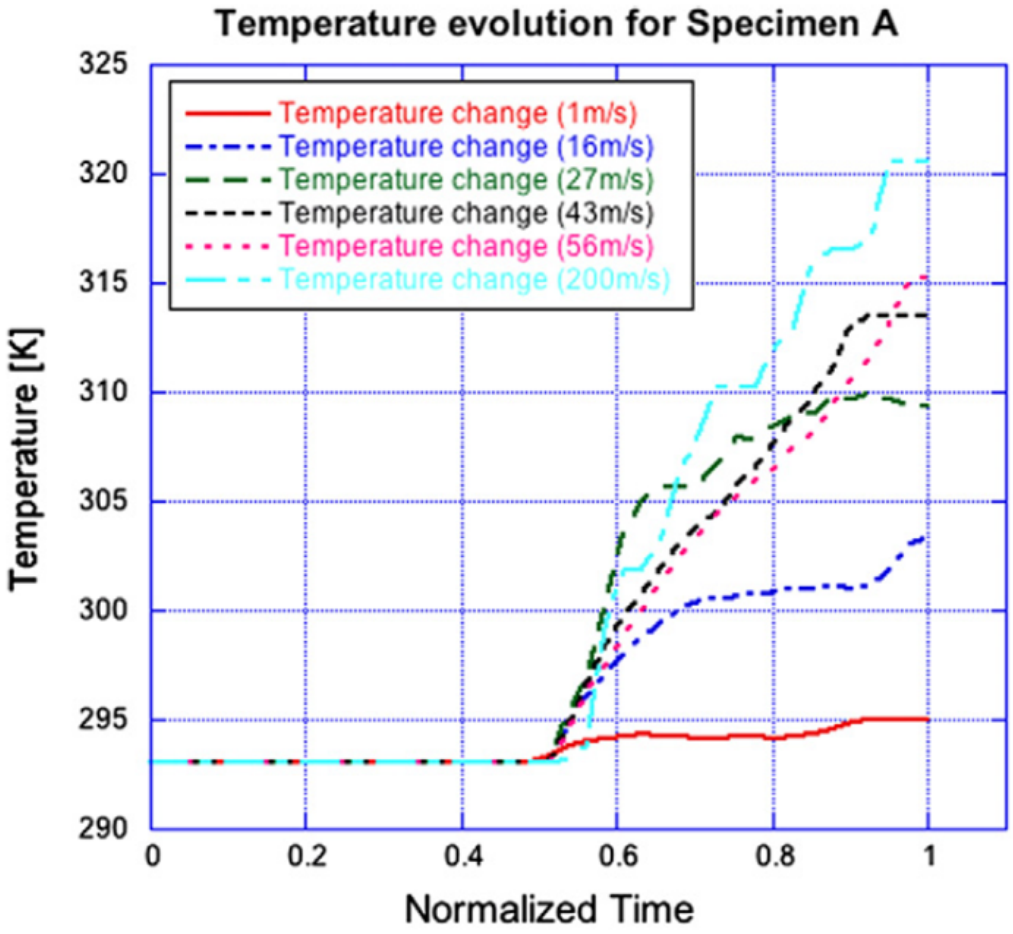

Figure 2.2: Frictional Temperatures of VascoMax 300

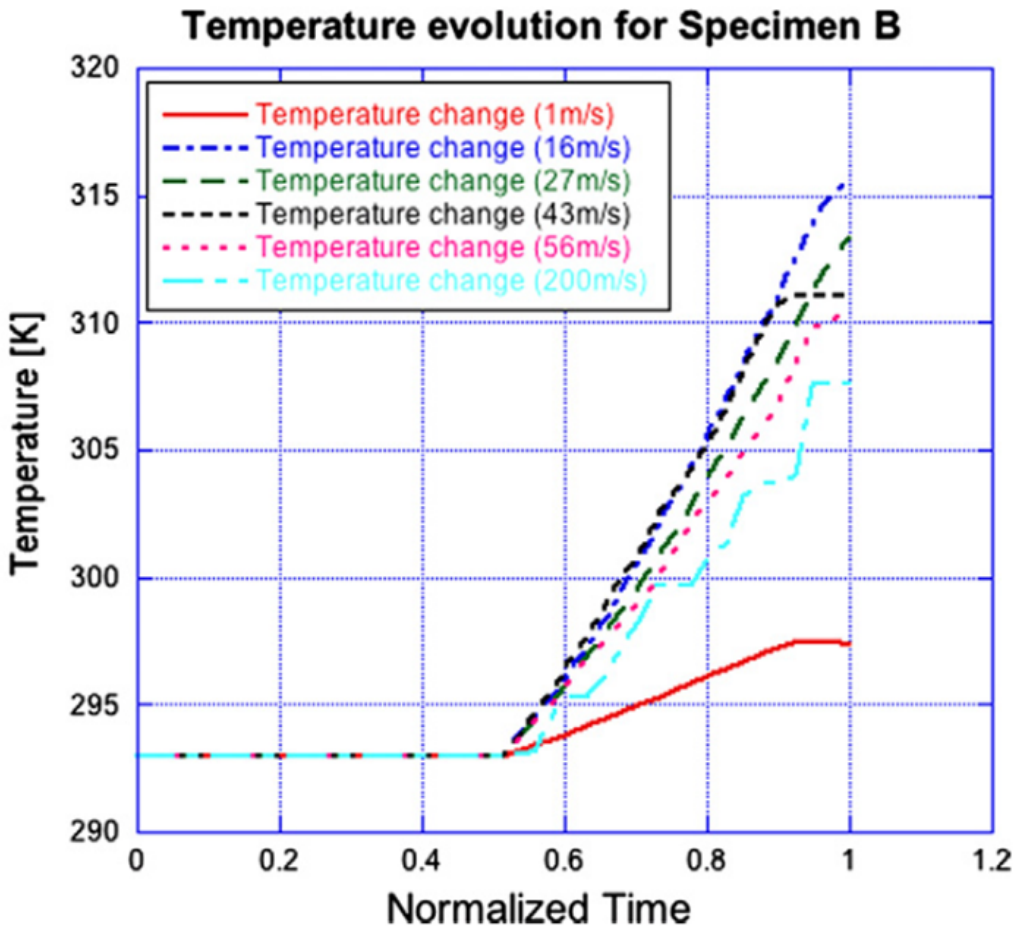

The above charts[2] from the research performed by Lodygowski et al[3], show that for the velocities and wear interval time, 0.25 s, considered herein that an initial temperature of 293 K is the correct choice for both the slipper and rail.

[2]Reprinted from International Journal of Plasticity, Vol 27, A. Lodygowski, G.Z. Voyiadjis, B. Deliktas, A. Palazotto, Non-local and numerical formulations for dry sliding friction and wear at high velocities/ Computational Modeling, Page No. 1019, 2011, with permission from Elsevier.

2.1.2 Equation of State.

The EOS is used to compute the temperatures that are developed by considering the plastic flow as it progresses through the material as a function of a given stress wave. It the defines the relationship between the pressure, density, and temperature. Material temperatures modified by the presence of a stress wave or shock wave are fed into the plasticity model through the homologous temperature parameter. Since this FEM is based on the B-H model, the Mie-Grüneisen EOS is utilized to maintain consistency between the lines of research. The equation governing Mie-Grüneisen EOS can be found below. Where Γ_0, c_0, and s are material constants, ρ_0 is the reference density, E_m is the internal energy per unit mass, and $\eta = 1 - \frac{\rho_0}{\rho}$ is the nominal volumetric compressive strain.

$$p = \frac{\rho_0 {c_0}^2 \eta}{(1 - s\eta)^2}\left(1 - \frac{\Gamma_0 \eta}{2}\right) + \Gamma_0 \rho_0 E_m \tag{2.4}$$

The relationship between the linear shock velocity U_s and the particle velocity U_p is defined by the material parameters c_0 and s as seen below.

$$U_s = c_0 + sU_p \tag{2.5}$$

The EOS is an important consideration when modeling impacts where there are shock wave interactions in a material that is plastically deforming. The Mie-Grüneisen EOS is necessary to determine the shock temperatures and the residual temperatures as well as predicting the material's shock response[26]. The EOS relates pressure, density and internal energy in the model. It can easily be seen how shock waves in the model can cause pressure, density, and internal energy changes which in turn change the local material temperatures further affecting the plasticity. The Mie-Grüneisen parameters used for this research can be found in the table below. These parameters were obtained from AFIT's CTH database. The EOS can be used even if there is no shock (discontinuity in a stress wave) present. One drawback to this EOS is that if there is melt i.e. a phase change, it does not take this into account. This may be important but not considered.

Table 2.3: Mie-Grüneisen Equation of State Parameters

Material	c_0 (km s^{-1})	s	Γ_0
AISI-1080 Steel	4.16	1.195	1.630
VascoMax 300 Steel	3.98	1.580	1.600

2.1.3 Johnson-Cook Fracture Dynamics.

The next area of discussion is the fracture dynamics. This FEM incorporates JC fracture dynamics. This phenomenological model was showcased in 1985, by Johnson and Cook[17]. In this work the fracture dynamics of materials are modeled on strain, strain rate, temperature and pressure[17]. The basic form of the model can be found below:

$$D = \sum \frac{\Delta\varepsilon}{\varepsilon^f} \tag{2.6}$$

Where $\Delta\varepsilon$ is the increment of equivalent plastic strain for an integration cycle and ε^f, defined below, is the strain at fracture. In the above equation, it can be discerned that the summation symbol accounts for the combined damage or damage history, as it applies to a material or a model element. This equation says that the ratio of the change in strain to the strain at failure is the determining factor to decide if damage should be initiated.

$$\varepsilon^f = [d_1 + d_2 \exp d_3\sigma^*][1 + d_4 \ln \dot{\varepsilon}^*][1 + d_5 T^*] \tag{2.7}$$

$$\sigma^* = \frac{\sigma_m}{\bar{\sigma}} \tag{2.8}$$

Where σ^* is the JC Pressure-Stress ratio and σ_m is the average of the three normal stresses and the below equation for $\bar{\sigma}$ is the Von Mises Equivalent Stress.

$$\bar{\sigma} = \sqrt{\frac{1}{2}\left[(\sigma_1 - \sigma_2)^2 + (\sigma_2 - \sigma_3)^2 + (\sigma_3 - \sigma_1)^2\right]} \tag{2.9}$$

The dimensionless strain rate, $\dot{\varepsilon}^*$, is given by the equations (2.10) and (2.11) below.

$$\dot{\varepsilon}^* = \frac{\dot{\varepsilon}}{\dot{\varepsilon}_0} \text{ for } \dot{\varepsilon}_0 = 1\,\text{s}^{-1} \tag{2.10}$$

$$\dot{\varepsilon} = \sqrt{\frac{2}{9}\left[(\dot{\varepsilon}_1 - \dot{\varepsilon}_2)^2 + (\dot{\varepsilon}_2 - \dot{\varepsilon}_3)^2 + (\dot{\varepsilon}_3 - \dot{\varepsilon}_1)^2\right]} \tag{2.11}$$

Since the JC fracture parameters for AISI-1080 steel and VascoMax 300 steel are not available, the parameters for AISI-1045 steel and Ti-6A1-V4 alloy were substituted respectively, based on the research of Johnson and Holmquist[18]. The parameters can be found in the table below.

Table 2.4: Johnson-Cook Dynamic Fracture Parameters

Material	d_1	d_2	d_3	d_4	d_5
AISI-1080 Steel (AISI-1045 Steel)	0.06	3.31	1.96	0.002	0.58
VascoMax 300 Steel (Ti-6Al-4V Alloy)	-0.09	0.27	0.48	0.014	3.87

In the FEM, the damage is initiated by the JC fracture model. Once damage has been initiated, the rate at which the damage progresses is set by the damage evolution parameter chosen by the user. The type of damage evolution is also set to “Displacement“, where damage evolution is defined as a function of the total plastic displacement after the fracture model has initiated damage[1].

Below in figure 2.3 is a depiction from the Abaqus User’s Manual of how the damage is handled in the model. At the point of yield, $D = 0$, damage is initiated and then the damage evolution parameter defines how quickly the damage will progress downward on the curve towards zero stiffness when the element is removed (if Element Deletion or a failure criteria is specified). When the value for D reaches 1 for an element, the

element no longer has any stiffness and is removed from the simulation leaving the elements surrounding it to shoulder the load. D captures the combined effect of all teh active damage mechanisms[1]. This is precisely how simulated wear is tabulated in this research. As the slipper elements are destroyed, when their D value reaches 1, their volume is added to the rest of the destroyed elements, to account for the material lost due to wear, yielding a simulated wear volume.

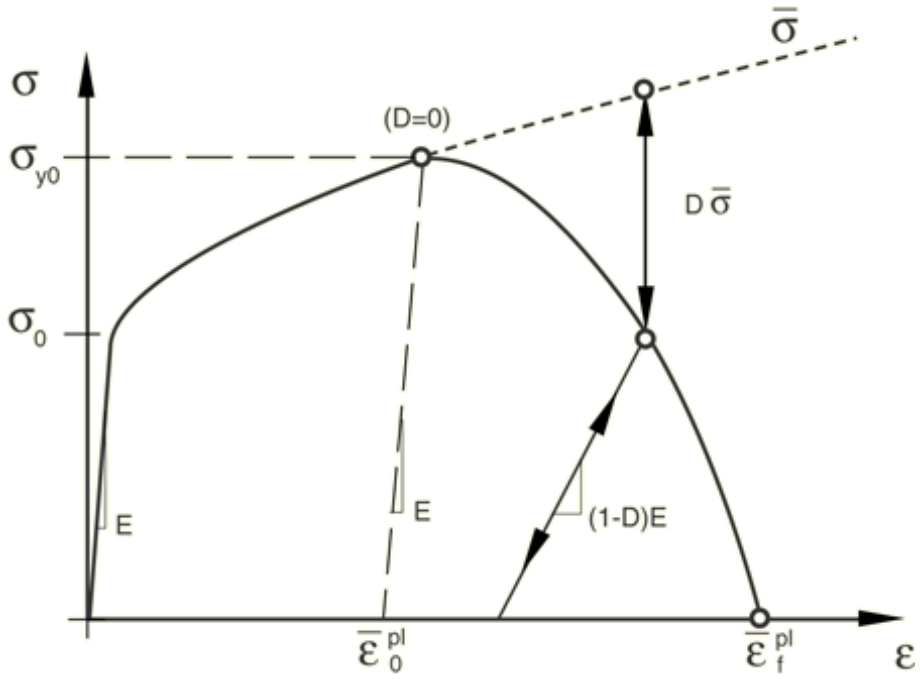

Figure 2.3: Damage Response for Ductile Materials[1]

The rate at which the element is removed can have far reaching implications for an impact model to be a realistic simulation. If elements are not removed in a timely manner, they will continue to stretch in a unrealistic manner as they loose stiffness too slowly.

Applying a damage evolution parameter such that the elements are failed and removed quickly will also be unrealistic, as sub-surface, interior, elements will be burdened with

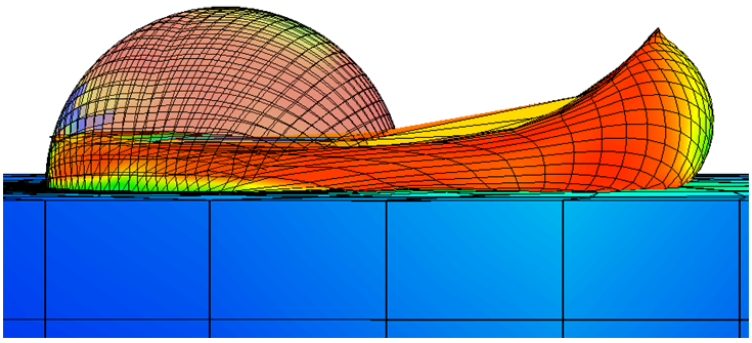

Figure 2.4: Unrealistic Stretch of Asperity Elements

the stress and strain that the surface elements should have experienced. A viable way to determine the damage evolution parameter is to ensure the model is removing the damaged elements in a timely manner and no unrealistic displacement is occurring. Figure 2.4, above highlights a model that is not failing elements correctly, the asperity elements are stretching well beyond where they should. The undeformed asperity can be seen on the left and the deformed, mushed to the right. Some of the elements have stretched well beyond 10 times their length!

2.1.4 Coulomb Friction Model.

Since there is contact and since wear is primarily a function of this contact, it becomes important to associate a frictional related function to the analysis. The contact algorithm for this FEM uses the Coulomb friction model. With the coefficient of friction, μ given by Montgomery's steel on steel friction research[27]. These values were deemed appropriate for this research since as Hale[11] states "The Montgomery frictional function is conservative at low pressure velocity". The table of values that are fed into the FEM for the coefficient of friction at a given speed, are taken from the B-H research and FEM[30].

Below in figure 2.5, is a chart plotted by Hale[11] that shows a curve fit to Montgomery's pin on disk data. This data is from of projectile steel on gun barrel steel

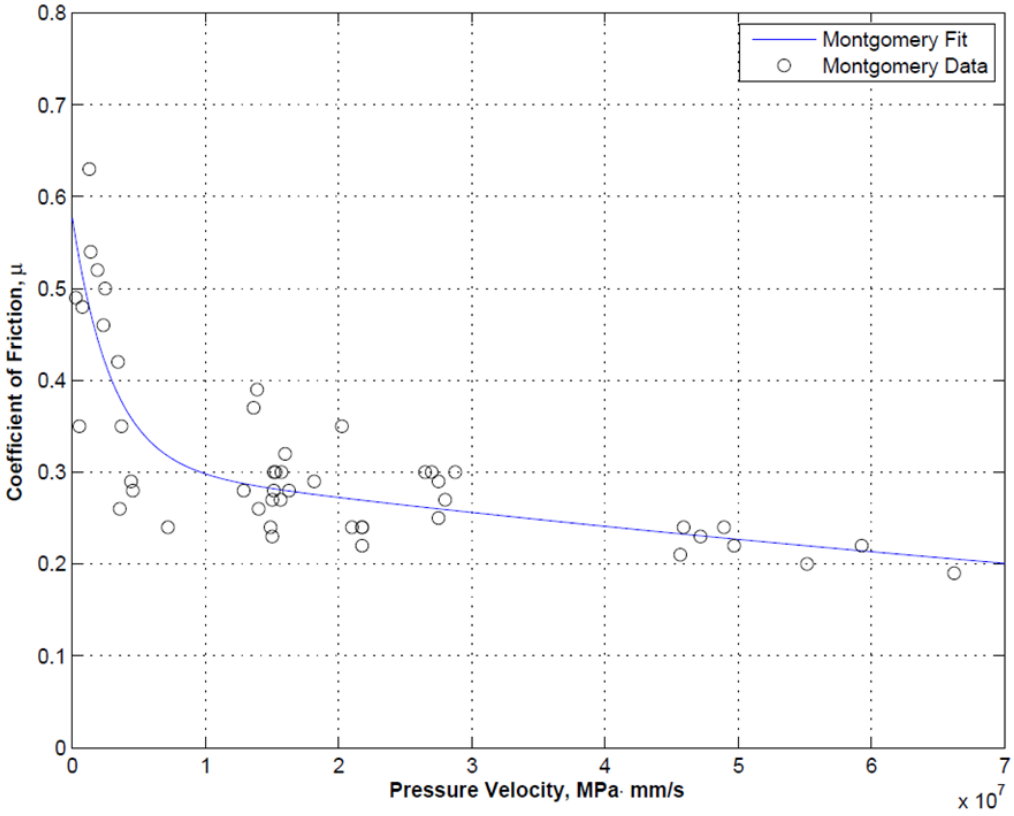

Figure 2.5: Plot of Montgomery Pin on Disk Data with Curve Fit[11]

for different pressure-velocity values. The function for this curve fit is shown below in equation (2.12) and the values from this coefficient of friction function are tabulated and utilized in the FEM.

$$F_f \leq \mu \cdot F_N \tag{2.12}$$

$$\mu\,(Pv) = \begin{cases} 0.2696e^{-3.409\times10^{-7}\cdot Pv} + 0.3074e^{-6.08\times10^{-9}\cdot Pv} & : 0 < Pv < 4.45\times10^{8} \\ 0.02 & : Pv \geq 4.45\times10^{8} \end{cases} \tag{2.13}$$

The general contact algorithm for this model will apply appropriate frictional force to the surfaces in contact with each other based on the computed normal forces. As the collision of materials within an element occurs, it becomes necessary to record the tangential and normal forces generated. These forces combined with the frictional model creates a state of imbalanced force-balance that must be maintained. This is done through the energy conservation equations and the EOS.

2.1.5 Specific Heat Capacity.

The original B-H model utilized static values for specific heats, i.e. only a single value was used for the simulations, however, two values for the VascoMax 300 specific heat were compared. A comparison will also be made between model results with the original, "static", specific heat parameter, and with the table of specific heat parameters. Below are tables showing the specific heat values to be used for comparison between the coarse and fine meshes at the $40\,\mathrm{m\,s^{-1}}$ and a gap spacing $0.5\,\mu\mathrm{m}$.

Table 2.5: VascoMax 300[12]

C_p $\mathrm{J\,g^{-1}\,K^{-1}}$	Temperature K
0.3603	297
0.4819	422
0.5992	589
0.8590	700

Table 2.6: AISI-1080 Steel[2]

C_p J g^{-1} K^{-1}	Temperature K
0.4902	373
0.5321	473
0.5489	523
0.5657	573
0.5866	623
0.6076	673
0.6704	773
0.7123	872
0.7710	972
2.0824	1022
0.6159	1072

Two meshes will be considered to help identify, attribute or separate damage reductions or increases between material parameter updates or mesh refinements. The two meshes considered for this study are the coarse and fine meshes. These two meshes being the extremes in the study will help shed some light on the effects varying the parameters will have when the mesh is refined.

III. Model

The modeling package chosen for this work is Abaqus[1], for a couple of reasons. This is the available software that can perform the necessary functions for this research, and this is the same package utilized by B-H[30] for the original model. Abaqus has a standard and an explicit finite element solver. The explicit solver is used for this model. The explicit solver is intended for large non-linear problems and as such the explicit integration method used is more efficient than the implicit integration methods for solving three dimensional contact problems that include impacts and high energy plastic events. As with high energy or high speed events between materials, stress waves and possible shock waves are propagated through materials. The explicit solver is much more efficient with these types of problems than the standard solver. One drawback to using the explicit solver is the fewer choices of element types. This research is not intended to prove out and explore different element types, but rather to better define the medium speed wear regime and compare that to previous modeled wear research. Therefore, the same element type will be used. These meshes and element types will be discussed later in detail. As mentioned earlier, Abaqus has the necessary material property models to solve complex problems involving visco-plasticity, fracture and contact at high speeds. The material behavior models were discussed in the Theory Chapter. Abaqus is also fairly easy to learn and use to build parts within the graphical user interface (GUI). The package can handle multiple materials, multiple parts and produce very nice visualizations and screen captures of the models.

3.1 Assemblies, Parts and Mesh Properties

The model herein is composed of twelve different parts. Six in the slipper assembly and six in the rail assembly. This is done to separate the parts that need a fine mesh (slipper

wedges and asperity blocks) from those that only need a coarse mesh (slipper block and rail block). This is to reduce the total number of elements and nodes as well as make post processing of the data easier as the different parts can be individually assessed separate from the whole assembly.

3.1.1 Assemblies.

The slipper assembly and five slipper wedges can be found below left. The leading edge of the slipper wedges is 6 µm and the width of each block is 5 times the size of it's counterpart asperity i.e. the slipper wedge for the 5 µm asperity is 25 µm wide. Slipper block is 75 µm cubed. This proved to be the most efficient way to construct this model. Other variations were developed with five part rail and five part slipper. These tended to be difficult to partition to reduce the number of elements and nodes even though, it was easier to tie the parts together.

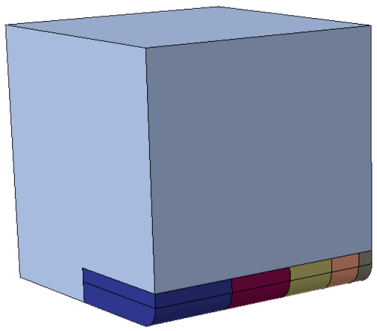

Figure 3.1: Slipper Assembly

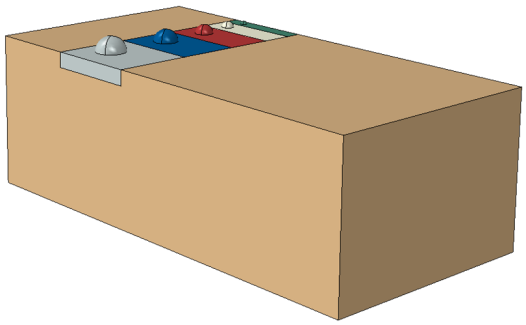

Figure 3.2: Rail Assembly

The rail assembly: rail block with asperity blocks can be found above right. The rail block is 75 µm wide, 75 µm deep, and 150 µm long. The dimensions of the assemblies in this model are based on those of the B-H model. The dimensions were chosen such that stress waves would not have time to reflect off of boundary conditions and interact with

the asperity/slipper collision. The present model is comprised of the two above assemblies. The model assembly can be seen below in figure 3.3.

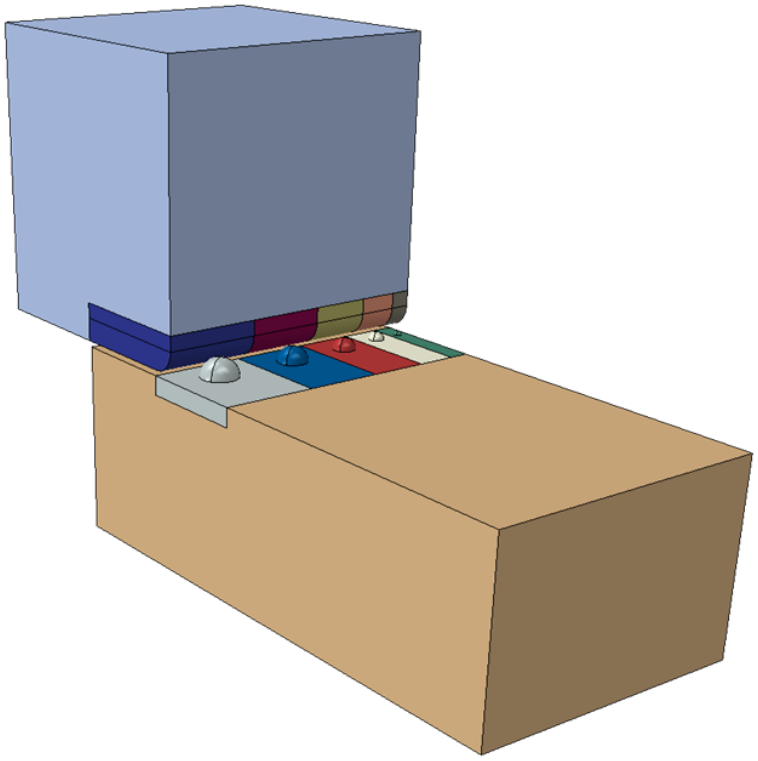

Figure 3.3: Model Assembly

Since this model is being run at lower speeds, a few design changes have been implemented as can be seen in figure 3.4 below. The asperities do not wear across the slipper as far therefore, the slipper wedges or wear surfaces in the slipper have been shortened. This allowed for a reduction of the number of elements and nodes simplifying the model. In the figure below, the fine mesh parts (wear area) are the darker areas. The coarse mesh parts (non-wear areas) are the light colored areas. These changes are further discussed in the Mesh Properties section.

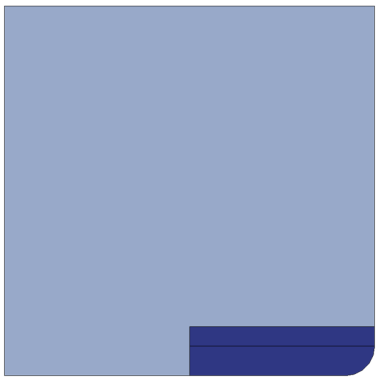

Figure 3.4: Present Slipper

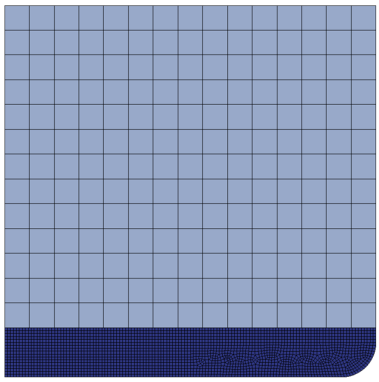

Figure 3.5: B-H Slipper

3.1.2 Mesh Properties.

This model has a total of 255938 nodes and 226929 elements whereas the B-H model had 402611 nodes and 359143 elements. All of the the elements are of the C3D8R type. This is a three dimensional, 8 noded linear hexahedral element utilizing reduced integration, seen below.

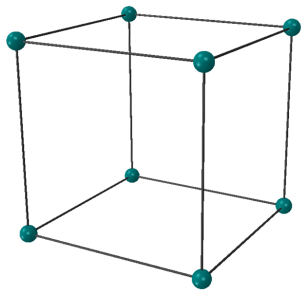

Figure 3.6: C3D8R Element Configuration

The B-H slipper wedges had 295648 nodes and 266797 elements. These modified wedges have 152652 nodes and 137038 elements.

Another modification to the model is how the asperities are partitioned. This was done to reduce the number of distorted or slender elements around the periphery of the asperity

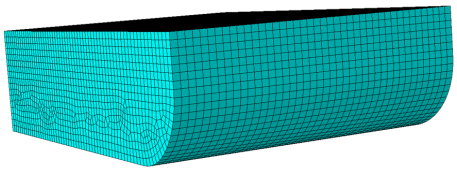

Figure 3.7: 5 μm Wedge

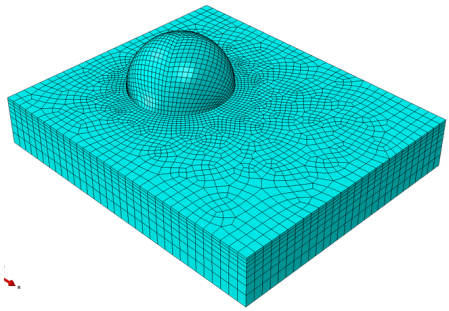

Figure 3.8: 5 μm Asperity Block

that were caused by forcing the linear hex elements to assume the hemispherical shape. The hexaderal element is not well suited for spherical surfaces. The new partitioning schema can be seen in the figure below right. This partition, the three intersecting lines and the circumference of the asperity, slices through the asperity block allowing for a better mesh arrangement and less distorted elements. The asperity hemisphere is also partitioned across the block top surface. The asperity blocks have the same dimensions as the B-H model. The asperity block bases are 30 μm long and 5 μm high and the widths varies as five times the asperity radius.

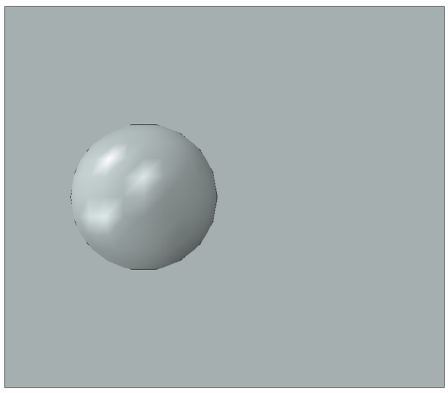

Figure 3.9: B-H 5 μm Asperity

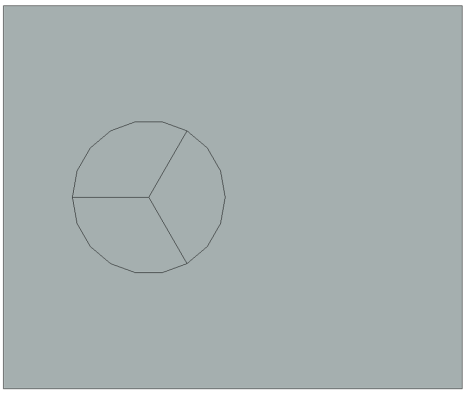

Figure 3.10: Present 5 μm Asperity

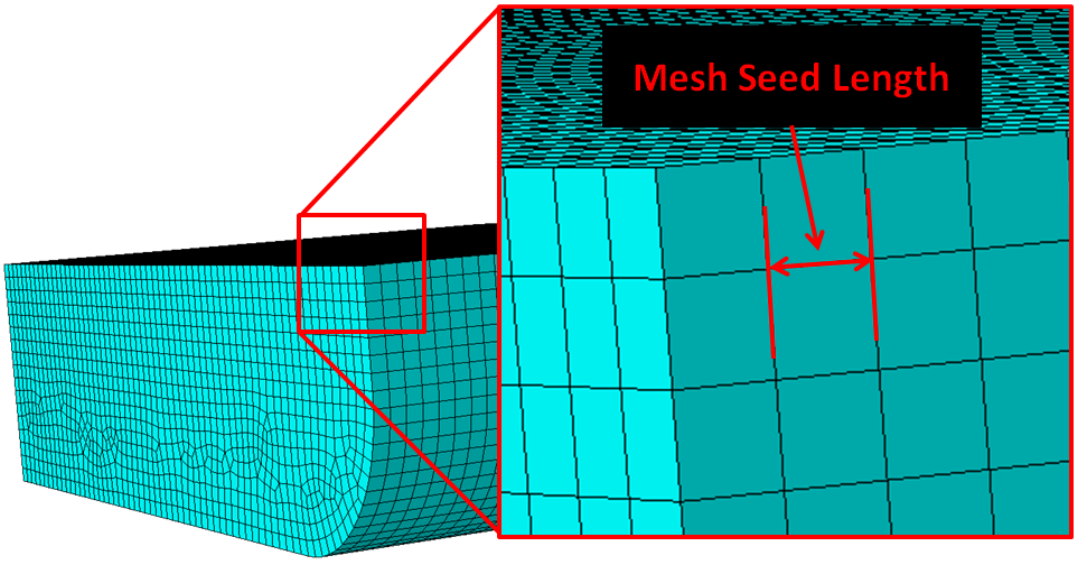

Figure 3.11: Mesh Seed Along Slipper Wedge

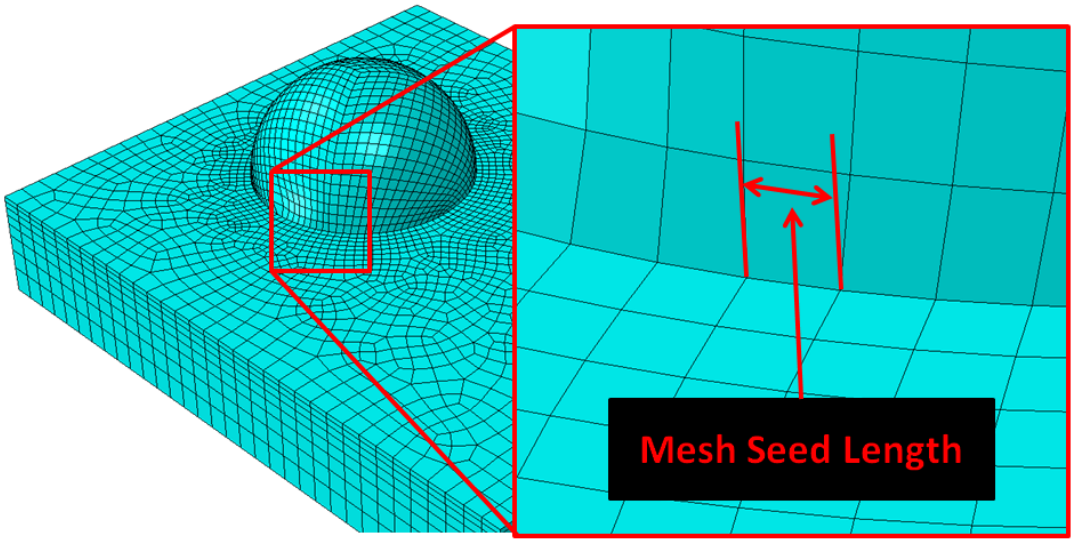

Figure 3.12: Mesh Seed Along Asperity Circumference

The original mesh seeding (the length elements) along the asperity edge are 0.3 μm. The coarse mesh on the slipper wedges have a mesh seed length of 0.6 μm, the fine mesh

has a length of 0.5 μm and the fine mesh has a mesh seed length of 0.4 μm. This mesh refinement is done to highlight any gains or losses in simulated wear volumes that are driven by mesh size. The mesh seed lengths for both the asperities and slipper wedges can be found in the table below and highlighted in the figures above. The mesh seed lengths on the asperities will not be changed between the simulations.

Table 3.1: Mesh Seed lengths for Slipper Wedges and Asperity Blocks

Part Instance	Coarse Mesh	Medium Mesh	Fine Mesh
Wedges	0.6 μm	0.5 μm	0.4 μm
Asperities	0.3 μm	0.3 μm	0.3 μm

Along with the mesh refinements, each speed increment will have three associated gaps between the slipper and the rail. This is done to capture the effects of asperity interactions at the micro-scale, as a way to account for the surface roughness coefficient between the two surfaces. B-H[30] first used this gap in his research for a number of reasons. The first is to mimic the effect of the two surfaces being in contact only at the discrete points defined by the asperities. The second reason is to provide an area where wear materials could go once worn from the surfaces. The third reason served as a calibration device for the model, to help match the wear to empirical results found by Wolfson[33]. By increasing or decreasing the gap the wear can be changed. The final reason is to avoid excessive shear at the asperity root. In the Hale model, the slipper slid directly on the rail effectively shearing the asperity off, this can be seen in Chapter 1 figure 1.4. Below in figure 3.13, the gap space between the slipper (top) and the rail (bottom) can be seen.

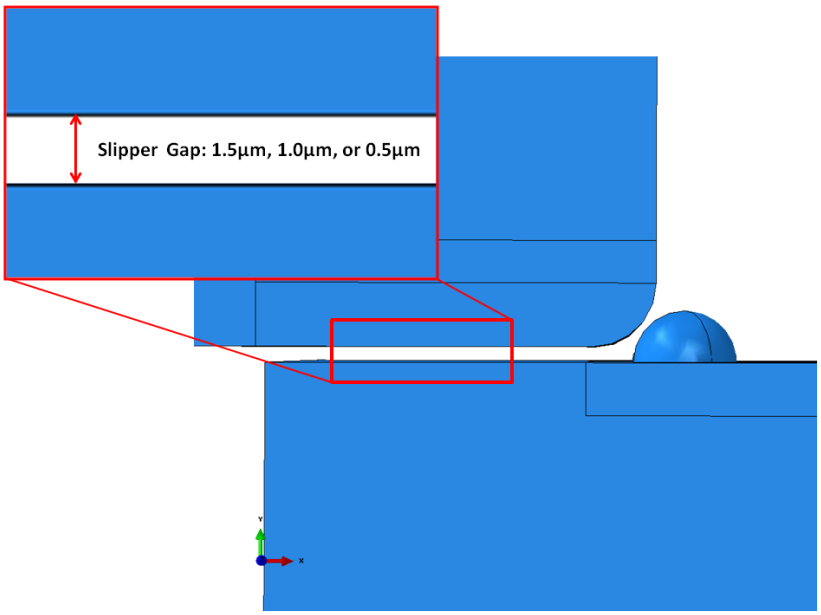

Figure 3.13: Model Gap Spacing

3.2 Materials

To simulate the HHSTT scenario, two materials need to be modeled. The rail and asperities composed of AISI-1080 steel and the slipper and slipper wedges composed of VascoMax 300 maraging steel. Below in the table are the Young's Modulus, density and melt temperature for the two materials in the model. The EOS, plasticity and fracture parameters used for these materials can be found in the Theory section.

Table 3.2: Material Properties

Material Property	1080 Steel	VascoMax 300
E	202.8 GPa	180.7 GPa
ν	0.27	0.283
T_{melt}	1670 K	1685 K

3.3 Steps and Predefined Fields

This model, just like any dynamic problem, has two steps an initial and final. The initial step assigns a predefined velocity field to the slipper to give the assembly motion prior to impact. The model also has a final step where contact begins to simulate the HHSTT slipper and rail interactions. The initial step defines the initial speed of all the nodes in the slipper assembly and the initial temperature of the slipper and rail assemblies. The final step changes where the slipper assembly velocity condition is applied, moving it from all the nodes to the back and top surfaces. The initial step applies initial conditions to the slipper before the slipper and rail make contact, the final step carries the initial conditions through the contact interactions. The initial conditions are slipper and rail temperature, slipper velocities, and a z-direction symmetry boundary condition (BC), $U3 = UR1 = UR2 = 0$ to ensure the model stays aligned in the x-direction (downtrack direction). For this speed regime, the slipper and rail are started at room temperature 293 K based on the research of Lodygowski, et al.[3] for the two speed increments explored in this research. This does not mean that the homologous temperature is zero all the time making the last term in the JC plasticity model 1. The model will actually calculate various local temperatures that will be utilized in the plasticity model via the EOS. For a high speed model, where the speed increment being explored, is in the middle of a sled run at a point in time where the slipper has already been heated due to aerodynamics and friction this initial temperature will be above room temperature[30].

Depending on the simulation, the slipper is assigned either $20\,\mathrm{m\,s^{-1}}$ or $40\,\mathrm{m\,s^{-1}}$ downtrack velocity and $-0.079\,\mathrm{m\,s^{-1}}$ or $-0.059\,\mathrm{m\,s^{-1}}$ vertically velocity, respectively. The down track velocities are chosen to better understand the wear in this speed regime. The vertical components of velocity were calculated as an average of the vertical velocities calculated from the DADS data for the given speed increment. A table of these increments

and velocities is shown below. A more detailed discussion on the calculation of these velocities is found in the Results and Analysis chapter.

Table 3.3: Speed Increments and Velocities

Speed Increment $m\,s^{-1}$	Speed Interval $m\,s^{-1}$	Vertical Velocity $m\,s^{-1}$
20	10 to 30	−0.079
40	30 to 50	−0.059

In the two figures below, 3.14 and 3.15, it can be seen how the initial and final velocities are applied between the two steps. In the figure on the left, the velocity vectors (downtrack and vertical velocities) are applied on all the parts of the slipper assembly. In the figure on the right for the final step, the velocities are applied only to the rear and top surfaces far away from the nodes and elements that will be impacting the asperities. This is done so that the velocities of nodes and elements in the slipper wedges are not augmented by the predefined velocity field, but rather by the impacting of the elements themselves. This way the velocities are transmitted through the slipper block and not artificially at the nodes in the wedges.

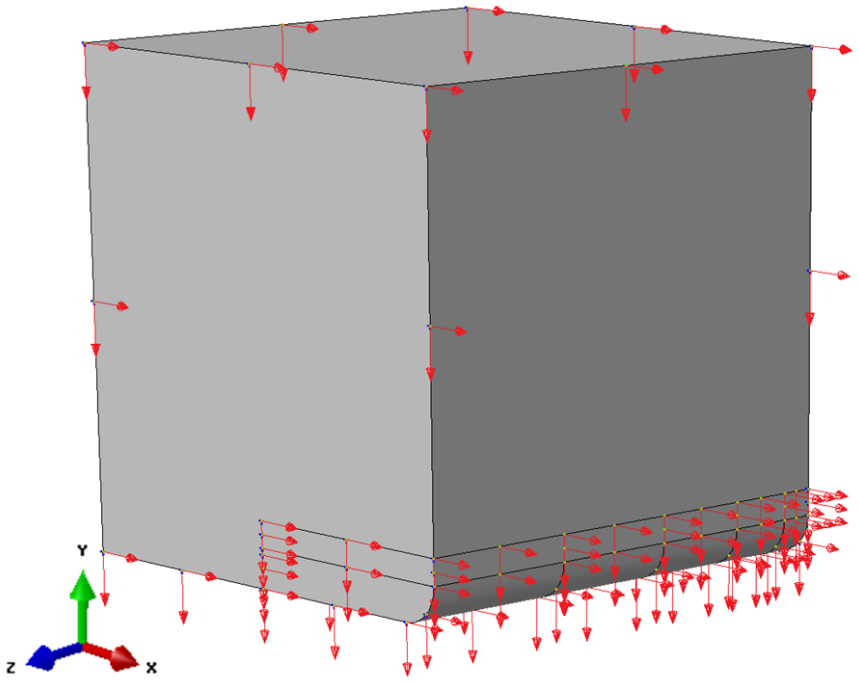

Figure 3.14: Predefined Velocities for Initial Step

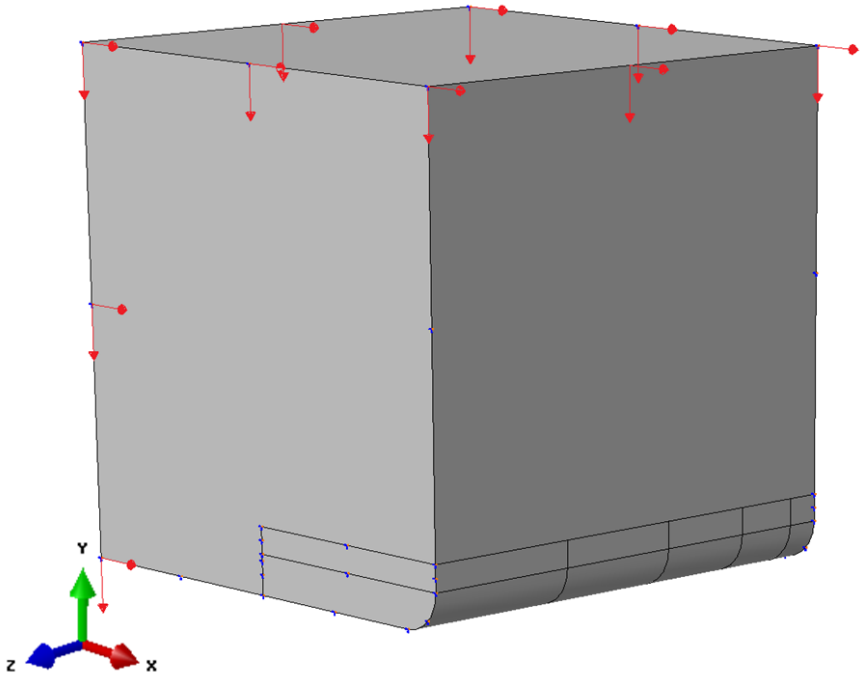

Figure 3.15: Predefined Velocities for Final Step

3.4 Contact Interactions: Coulomb/Montgomery Friction

As previously mentioned in the Theory Section, the Coulomb friction model is utilized with coefficients of friction updated in the simulation according to the speeds of surfaces that are in contact. The Montgomery coefficient of friction values are taken from an input table incorporated into the model. The general contact algorithm in Abaqus has been set to use this friction model based on the success of previous wear research[30][11]. It is a function dependent upon the pressure-velocity product. In fact, it is a function of the pressure-velocity product of the impacting elements between the slipper and the rail. This is where the general contact algorithm becomes important. A limited discussion is presented here but, a more extensive presentation can be found in the Abaqus documentation.

3.5 Constraints and Boundary Conditions

This model differs from the B-H model in how the parts are held together, but the boundary conditions to eliminate rotation and translation are the same.

3.5.1 Constraints.

In the B-H model, a rough interaction property is used to hold the parts together. This property is basically an extremely high frictional force (as called out in Abaqus) between the surfaces experiencing a tangential velocity. However, if the tangential velocities drop to zero, then this property no longer is in effect. The B-H model had high downtrack velocities and a vertical velocity of $-1\,\mathrm{m\,s^{-1}}$. With these higher speeds, there was always a normal force produced allowing the rough property interaction to hold the parts together. For the lower velocities of this study, the rough property interaction did not necessarily have a normal force for the rough property interaction to be maintained. The collision of the slipper blocks and asperity wedges did not produce enough upward force to ensure the parts held firmly together. An example of this type of failure can be seen below.

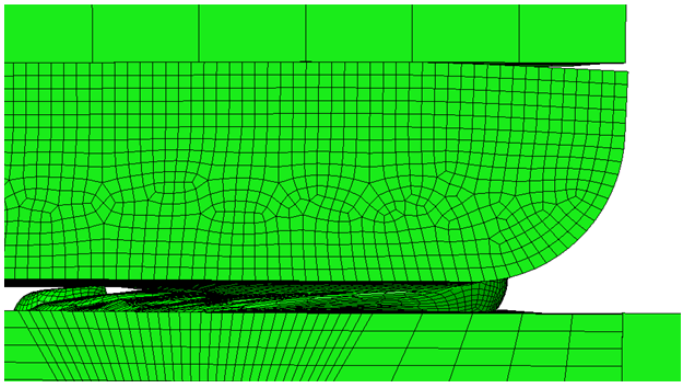

Figure 3.16: Release of Leading Edge of Slipper Wedge

In Figure 3.16 above, it can be seen how, in previous version of the model, the slipper wedges started to peel away from the slipper block during the collision. This issue necessitated the use of hard constraints to hold the assemblies together as seen in figure 3.17 below.

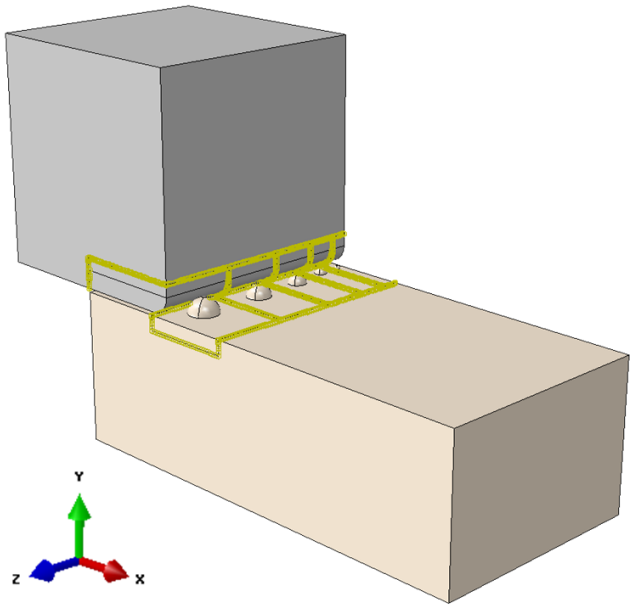

Figure 3.17: Assembly Constraints

The assemblies are held together with TIE constraints, as nodes on a smaller parts are tied to a surfaces on the larger parts. For example, the nodes on the tops of the slipper wedges are tied to a surface on the bottom of the slipper block and the nodes on the bottom of asperity blocks are tied to a surface on the rail block. Above in Figure 3.17, the TIE constraints for the two model assemblies holding part instances together can be seen as yellow edges.

3.5.2 Boundary Conditions.

This model has the same boundary conditions to those of the B-H model. The assembly also has a x-direction (downtrack) boundary condition applied to the forward and aft surfaces of the rail block to fix the rail in this direction as seen in the figure below.

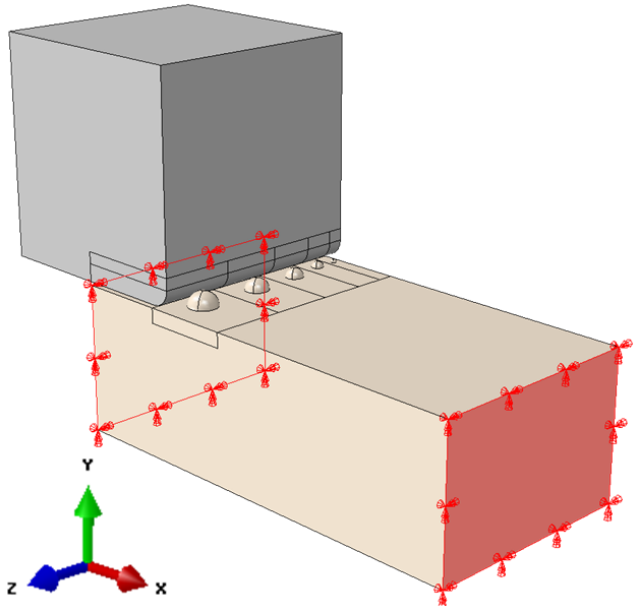

Figure 3.18: x-Boundary Condition

The assembly also has an encastre boundary condition applied to the bottom of the rail block, seen in Figure 3.19 below. This ensures the rail cannot rotate in any direction or translate in the y (vertical) direction.

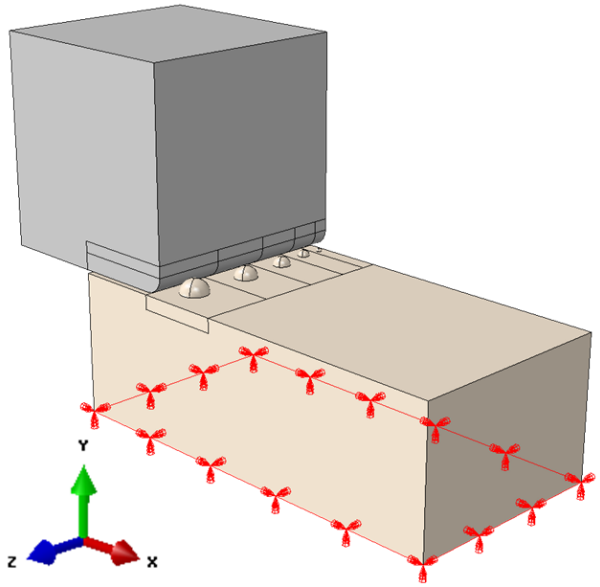

Figure 3.19: y-Boundary Condition

There is a z-direction (lateral) boundary condition applied to both sides of the slipper block, rail block and asperity blocks to ensure the slipper and rail stay aligned in the downtrack direction. See Figure 3.20 below.

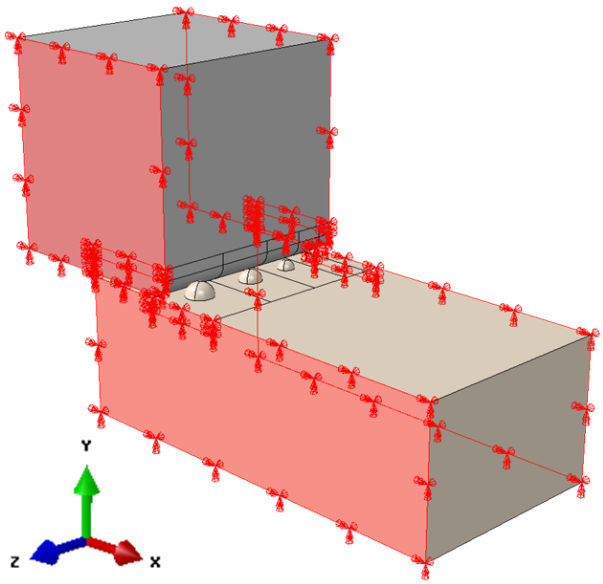

Figure 3.20: z-Boundary Condition

IV. Results and Analysis

The initial step in starting the analysis is the decomposition of the DADS data. For both speed increments, the increment duration, vertical velocity, average downward force, average contact percentage, and distance slid are computed. The velocities are directly used in the model, the average contact forces are used to compare wear results to empirical data. The contact percentages and distances slid are used to compute wear volumes and wear rates using the simulated wear volumes of the model output.

4.1 Input and Analysis Parameters

4.1.1 Velocities.

The DADS data from the 2008 sled test contained velocities from $0\,\mathrm{m\,s^{-1}}$ up to $1500\,\mathrm{m\,s^{-1}}$, for the first three stages. Below is a plot highlighting the velocity profile for the first three stages.

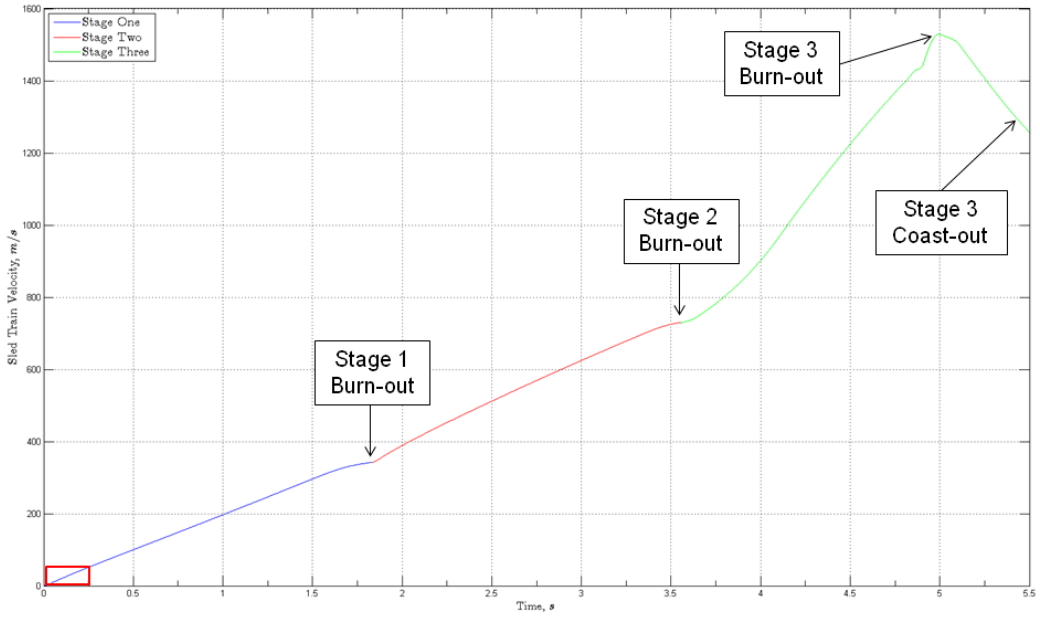

Figure 4.1: Sled Train Velocity Profile

It was decided early on that $20\,\mathrm{m\,s^{-1}}$ and $40\,\mathrm{m\,s^{-1}}$ were going to be the speed increments for this study. As can be seen in Figure 4.1 above that the sleds in the test traveled a lot faster than the two speed increments for this study. These two speed increments can be found on the far left side of the figure in the red box. The figures below show the $20\,\mathrm{m\,s^{-1}}$ and $40\,\mathrm{m\,s^{-1}}$ increments. An increment is the median velocity of an interval. For the $20\,\mathrm{m\,s^{-1}}$ increment, the interval is $10\,\mathrm{m\,s^{-1}}$ to $30\,\mathrm{m\,s^{-1}}$ as seen in Figure 4.2 below. For the $40\,\mathrm{m\,s^{-1}}$ increment, the interval is $30\,\mathrm{m\,s^{-1}}$ to $50\,\mathrm{m\,s^{-1}}$ as seen in Figure 4.3 below.

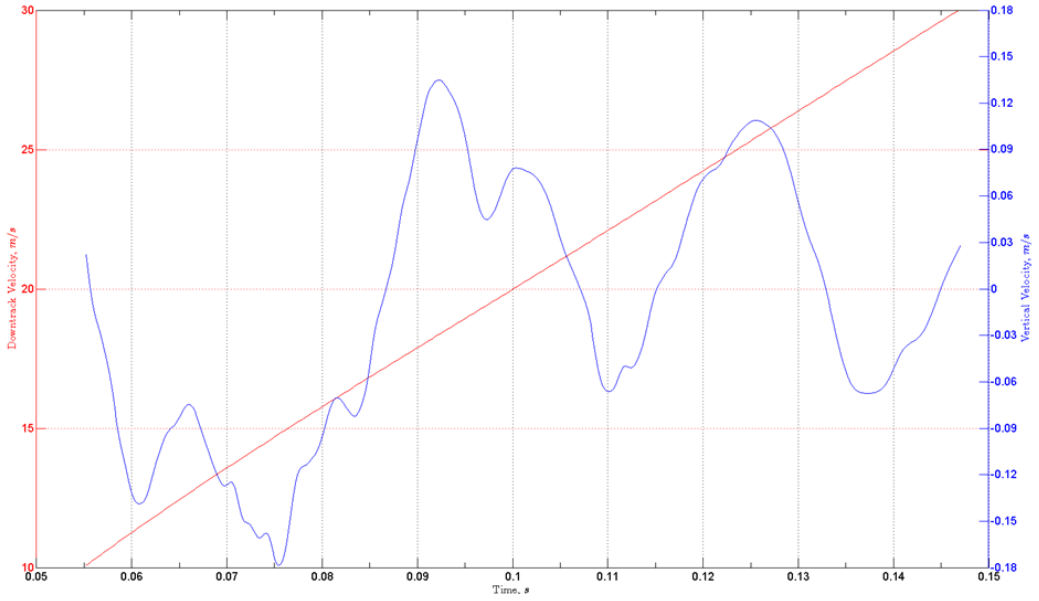

Figure 4.2: Downtrack and Vertical Velocities For $20\,\mathrm{m\,s^{-1}}$ Speed Increment

The vertical velocities are computed as the average of the velocities reported in the DADS data over the two speed increments. The variation in the vertical velocities for both speed increments can be seen in Figures 4.2 above and 4.3 below. The average vertical velocity for the $20\,\mathrm{m\,s^{-1}}$ and $40\,\mathrm{m\,s^{-1}}$ speed increments are $-0.079\,\mathrm{m\,s^{-1}}$ and $-0.059\,\mathrm{m\,s^{-1}}$, respectively.

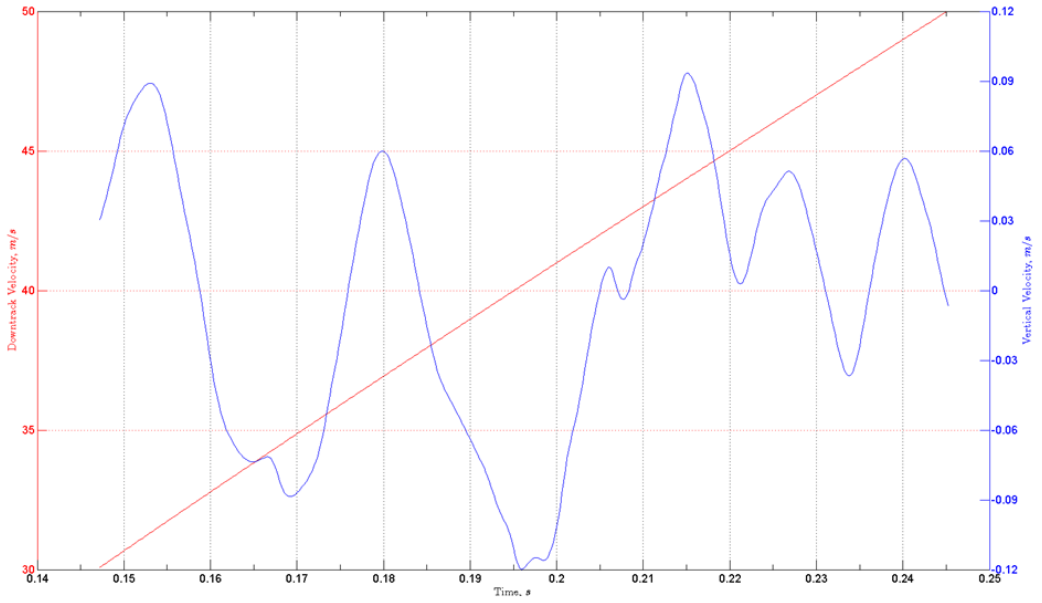

Figure 4.3: Downtrack and Vertical Velocities For 40 m s^{-1} Speed Increment

4.1.2 Contact Forces.

The rail cross section figure below shows the contact points, 3 and 4, for the aft right (AR) slipper. The contact points are where forces are generated between the rail and the underside of the slipper. When the slipper is lifted off the rail due to aerodynamic effects, the contact forces reduce to zero. Conversely, when the slipper is in contact with the rail, the slipper forces are positive. AR3 is on the outside, starboard, edge of the slipper.

To compute the average contact forces, the specific data for the relevant speed increment must be extracted from the DADS data. The increment intervals for the 20 m s^{-1} and 40 m s^{-1} contact increments are 0.055 s to 0.146 s and 0.148 s to 0.2452 s, respectively. These time intervals divide the plot below at the 0.147 s location. The first interval, to the left of 0.147 s, being the 20 m s^{-1} interval and the second interval, to the right 0.147 s, being the 40 m s^{-1} interval. As can be seen in the figure below, there is only one block of forces applied to the slipper during each interval.

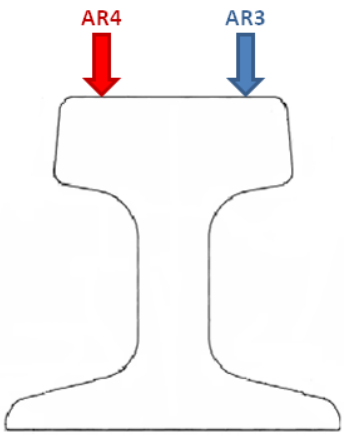

Figure 4.4: AR3 and AR4 Contact Points

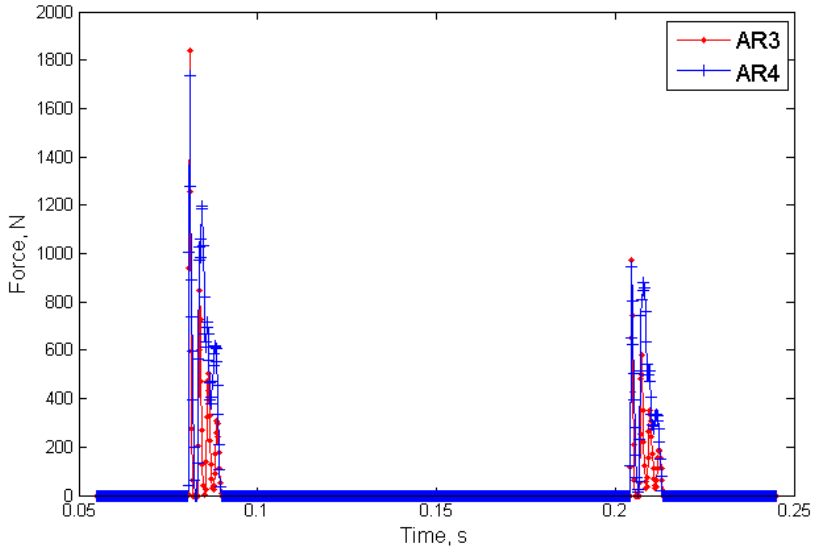

Figure 4.5: Contact Forces

To show the detail in the force curves, the total increment time was split at 0.147 s and the portions of the curves without contact forces were removed. The plots with more detail can be seen below.

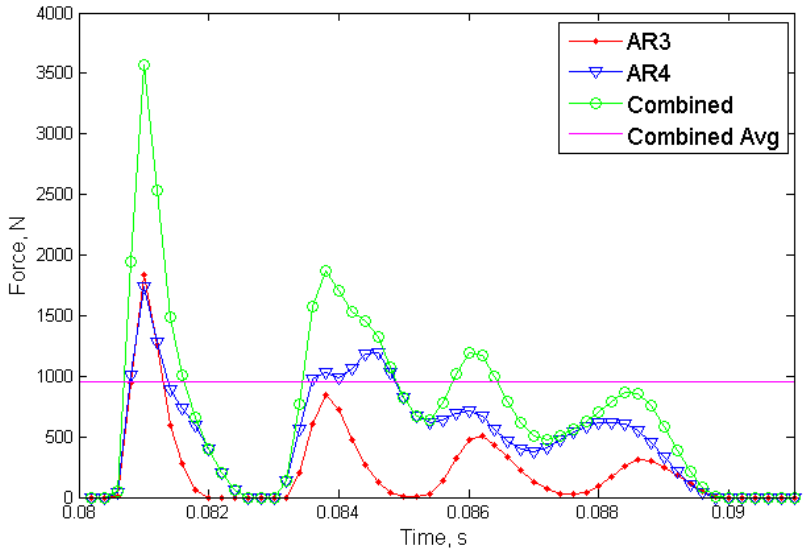

Figure 4.6: 20 m s^{-1} Contact Forces

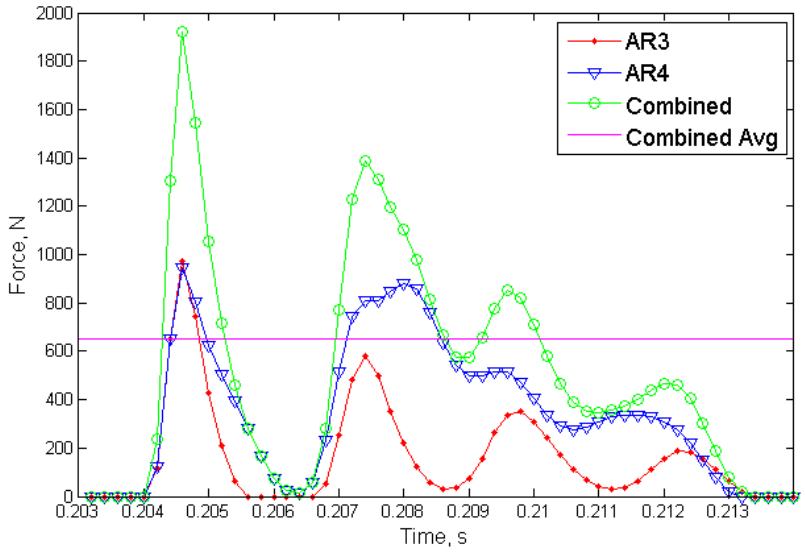

Figure 4.7: 40 m s^{-1} Contact Forces

The average force for each of these contact events can be found in table 4.1 below. The contact forces are calculated as the average of the combined AR3 and AR4 forces that are greater than zero. These forces are not directly utilized in the model, rather they are used

later to calculate normalized Pv values for both speed increments to be used to compare these wear results to those of Lim and Ashby's Wear Map[23].

4.1.3 Percentage Contact.

The contact percentage is calculated from the total time that the slipper is in contact with the rail, i.e. when the slipper forces are positive. When the slipper forces for either position 3 or 4 are positive, the slipper is assumed to be in contact with rail. The amount of time when the slipper is in contact with the rail is called the contact time. To calculate the percent contact, the contact time is divided by the total interval time. The DADS data is divided into 0.0002 s increments therefore, by taking the number of data points at which AR3 or AR4 is positive, for each speed increment, and multiplying it by 0.0002 s yields the increment contact times. It can be clearly seen in Figure 4.5 above that the slipper is not in contact with the rail a great deal. This is most likely do to the fact that the stage one thrust force is transmitted through stage two to stage three at a point above the center of mass causing the rear of the sled to lift off the rail. For the relatively low speeds in this research, corresponding to the very beginning of the sled run, stage one is thrusting throughout both speed increments. For the 20 m s^{-1} increment, there were 44 data points and 46 data points for the 40 m s^{-1} increment. Contact percentages are calculated below.

$$Cont\%_{20m/s} = \frac{44 \text{ points} \times 0.0002s}{0.146s - 0.0550s} = 9.6\% \tag{4.1}$$

$$Cont\%_{40m/s} = \frac{46 \text{ points} \times 0.0002s}{0.148s - 0.2452s} = 9.3\% \tag{4.2}$$

4.1.4 Distance Slid.

The distance slid is calculated from the speed increment multiplied by the total increment time. For the 20 m s^{-1} interval, 20 m s^{-1} is multiplied by the increment duration, 0.091 s. For the 40 m s^{-1} interval, 40 m s^{-1} is multiplied by the increment duration, 0.0972 s. The distances can be found in the last column of table 4.1 below.

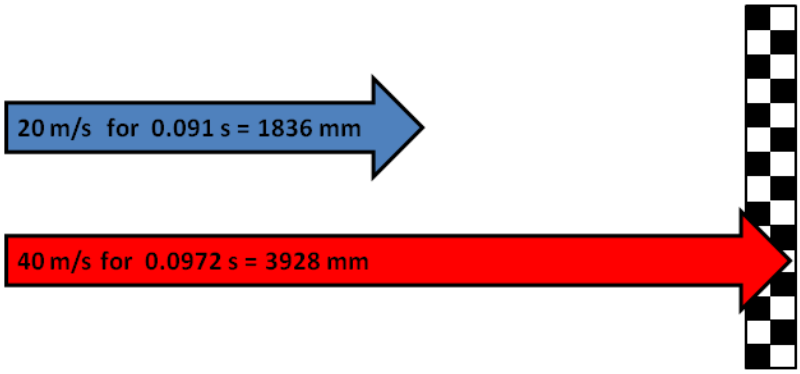

Figure 4.8: Distance Slid

Table 4.1: Input and Analysis Data for 20 m s^{-1} and 40 m s^{-1} Speed Increments

Speed Increment (m s^{-1})	Vertical Velocity (m s^{-1})	Average Force (N)	Percentage Contact (%)	Distance Slid (mm)	Increment Duration (s)
20	-0.079	952	9.6	1836	0.091
40	-0.059	652	9.3	3928	0.0972

The speed increments and vertical velocities are used in the FEM, while the average forces, contact percentages and distances slid are used for the results comparison analysis after the simulations have been completed.

4.1.5 Steady State Damage Response.

For the wear extrapolation methodology used it is important to ensure that a steady state damage response has been reached. This would ensure that a conservative wear number will be extrapolated to the real world wear surface. For this asperity model, the asperity can be thought of as a pin in a pin-on-disk experiment. A figure showing a pin on

disk test configuration can be found below. For this type of wear test, the pin is force fed onto a spinning disk and the rate at which the pin erodes, is measured.

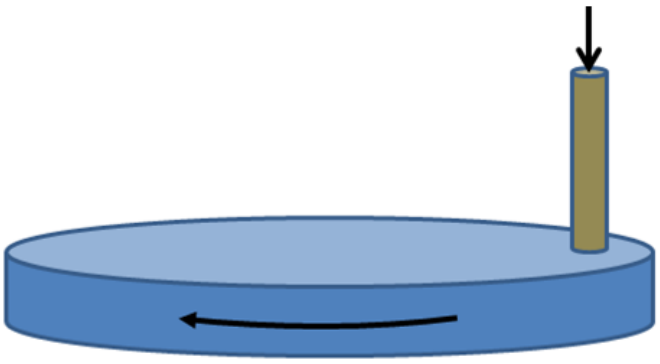

Figure 4.9: Pin-On-Disk Test Configuration

If the rail asperity is considered the pin and the slipper is considered the disk, essentially turning the model up-side-down, this wear problem is similar to the pin-on-disk test. With the pin or asperity in this case having a contact area that changes with time as it is worn down by the slipper, because the asperity is hemispherical. In Figure 4.10 below, the side view of the slipper and asperity can be seen at top and the corresponding top view of the contact area circle at the bottom.

In the above image, the slipper (blue) is traveling with a velocity, V_x, to the right and downward with a velocity, V_y. As this slipper travels across the asperity, the top of the asperity is worn down. This would cause the wear area of the asperity to increase over time defined by the equation (4.3) below. With the wear area of the pin/asperity increasing with time, the pressure exerted by the asperity on the slipper will decrease as the asperity is worn down. Extending this logic to the FEM, as the pin pressure decreases, fewer elements in the slipper will fail as time progresses. Therefore, the model over time should show a decreasing slope, asymptotic, trend in wear rate as the asperity is worn down.

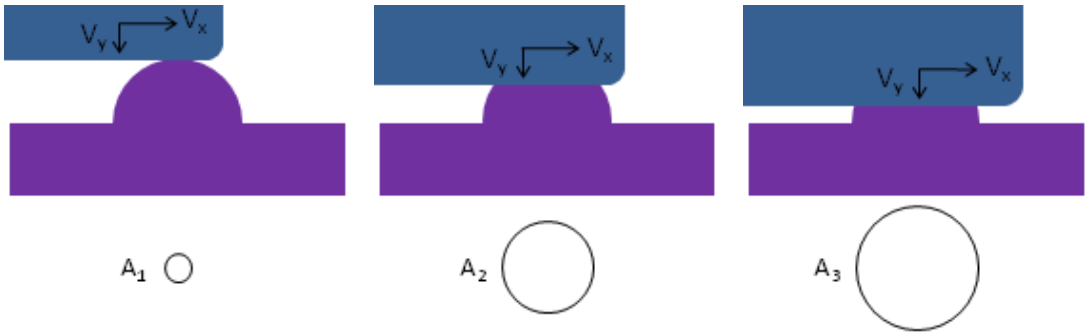

(a) Wear Area at Δt_1 (b) Wear Area at Δt_2 (c) Wear Area at Δt_3

Figure 4.10: Wear Area of An Asperity Top at Three Moments in Time

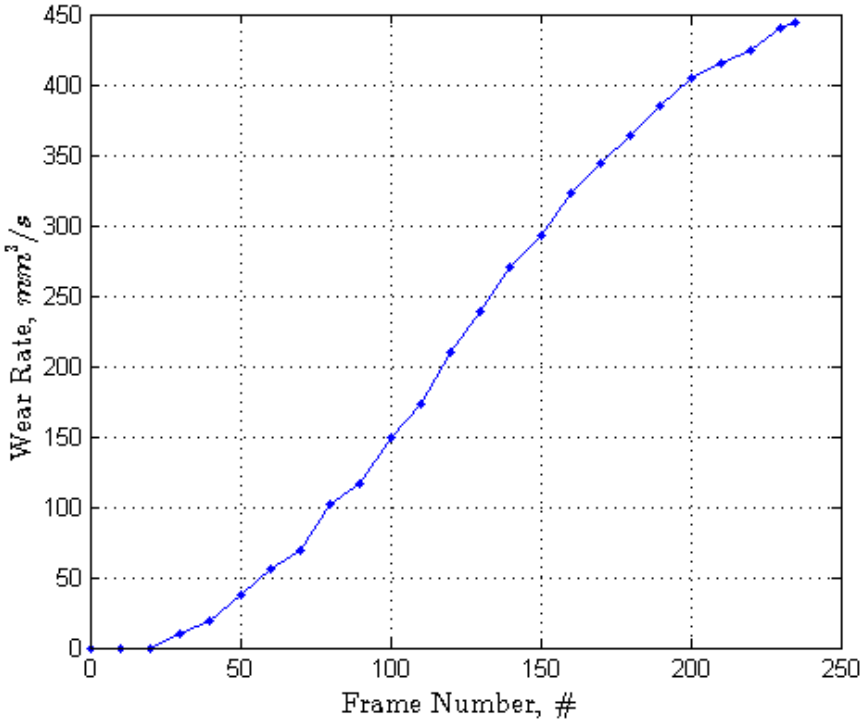

Figure 4.11: Steady State Damage at 20 m s^{-1}, 1.5 µm Gap Spacing, Fine Mesh

In Figure 4.11 above, the decreasing slope trend can be seen for the 20 m s^{-1} simulation with a 1.5 μm gap using the fine mesh. If the asperity is completely worn down, then the result would be two perfectly smooth surfaces, with a large contact area and low contact pressure, leading to a horizontal asymptote with essentially zero damage rate. The contact area calculation, can be found in the equation below.

$$A_c = \pi \cdot {r_c}^2 = \pi \cdot (r^2 - h^2) \tag{4.3}$$

Where r_c is the radius of the contact area, r is the radius of the asperity, and h is the height of the contact surface off the asperity root. Since the contact area is changing as a 2nd order function, it seems reasonable to assume that the trend in wear rate would follow the same 2nd order function. In the case of the plot above, the shape is higher than a 2nd order. This is because the slipper is not coming down on the asperity, but crashing into it, shearing off the top. In Figure 4.12 below, three images taken from the same model from which Figure 4.11 was created. These images show the impacted asperity at three different times. It is not until the asperity top is removed that the lower order function appears to govern the damage rate curve. As seen above, the wear rate is increasing up to about the 125th frame then decreasing thereafter. By the 125th frame, the asperity top has been removed as shown in the image below.

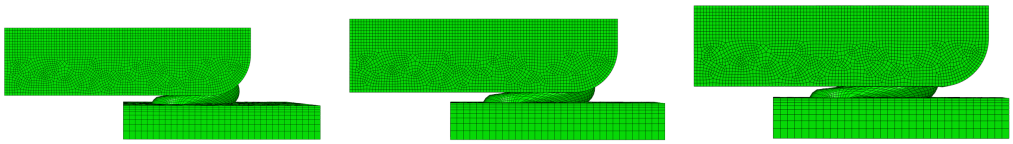

(a) Asperity at Frame 75 (b) Asperity at Frame 100 (c) Asperity at Frame 125

Figure 4.12: Asperity Top at Three Moments in Time

4.2 Simulation Wear Volumes

Simulated wear volumes are the raw tabulated volumes of elements that failed in the model's slipper wedges. The calculation of simulated wear volumes, V_{SA-r-v}, is carried out in the same manner as in the B-H research. The volumes of the failed elements in the slipper wedges corresponding to the five asperity radii are totaled yielding the simulated wear volumes. This is done for all three gap spacings, 0.5 μm, 1.0 μm, and 1.5 μm and for both speed increments, $20\,\mathrm{m\,s^{-1}}$ and $40\,\mathrm{m\,s^{-1}}$. This is repeated for the three wedge mesh refinements, coarse, medium, and fine. The mesh sizes, coarse, medium and fine, as explained in Chapter 3, relate to the length of an element in the slipper wedges where damage from asperities will be accumulated. The coarse mesh element length is on the average, 0.6 μm long, medium mesh element length is on the average 0.5 μm and fine mesh element length is on the average, 0.4 μm.

In the table below are the $20\,\mathrm{m\,s^{-1}}$ simulated wear volumes. Zeros indicate that model showed no wear for the given asperity radius, speed increment, and gap size combination. These values at first appear small however, these are the raw volumes from the model itself. In the next step, these volumes will be extrapolated up to a 1 mm × 1 mm area to apply the asperity distribution properties, then extrapolated again to apply the actual contact surface area of the slipper.

It can be readily seen that the 1 μm and 2 μm asperities never produced any wear damage on any of the meshes no matter the gap spacing. The fine mesh model with the 0.5 μm gap spacing had the most damage due to the 3 μm, 4 μm, and 5 μm asperities. Whereas the other simulations only showed damage from the 5 μm asperity. The simulated wear volumes appear to increase with mesh refinement.

The succeeding images show the damage on the slipper wedges for the various mesh refinements grouped by gap spacing for the $20\,\mathrm{m\,s^{-1}}$ simulations.

Table 4.2: $20\,\mathrm{m\,s^{-1}}$ Simulated Wear Volumes ($V_{SA-20m/s}$)

Mesh Refinement	Gap Spacing	Volumes $\times 10^{-8}\,\mathrm{mm^3}$				
Coarse	$0.5\mu m$	0.0	0.0	0.0	0.0	1.415
	$1.0\mu m$	0.0	0.0	0.0	0.0	1.691
	$1.5\mu m$	0.0	0.0	0.0	0.0	1.328
Medium	$0.5\mu m$	0.0	0.0	0.0	0.0	1.265
	$1.0\mu m$	0.0	0.0	0.0	0.0	1.697
	$1.5\mu m$	0.0	0.0	0.0	0.0	2.667
Fine	$0.5\mu m$	0.0	0.0	0.024	3.742	1.324
	$1.0\mu m$	0.0	0.0	0.0	0.0	4.263
	$1.5\mu m$	0.0	0.0	0.0	0.0	37.973
		1 μm	2 μm	3 μm	4 μm	5 μm
		Asperity Radaii				

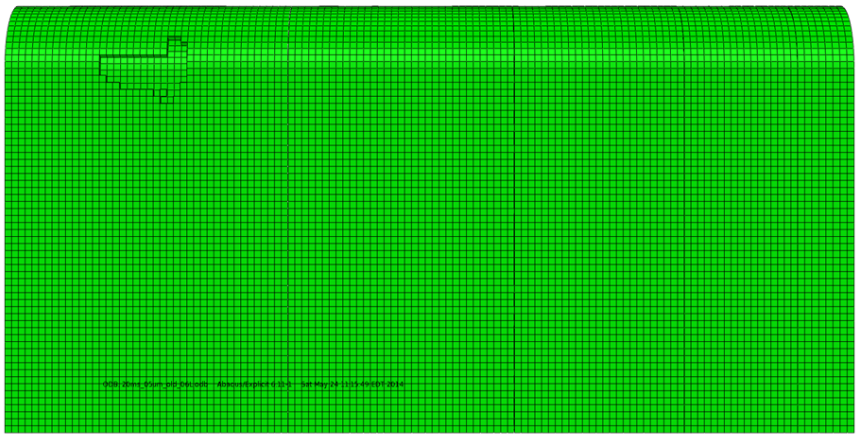

(a) Coarse Mesh

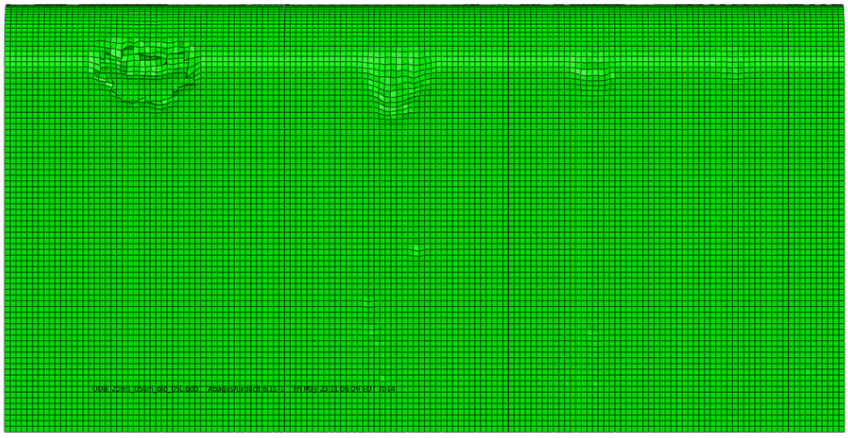

(b) Medium Mesh

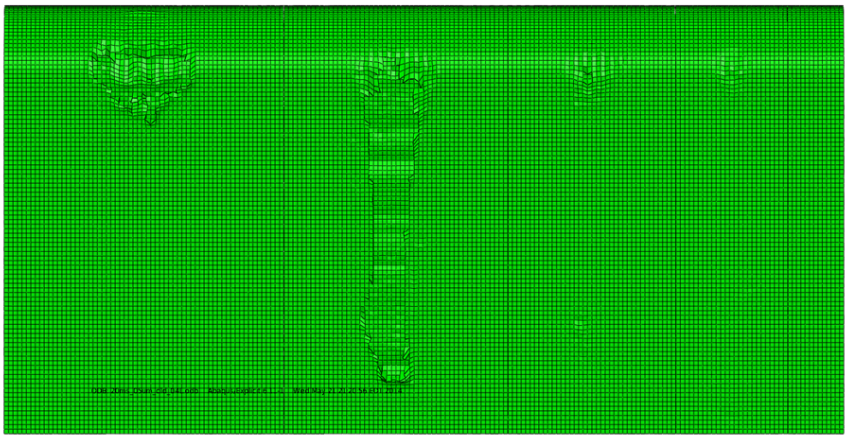

(c) Fine Mesh

Figure 4.13: Wear Patterns for 20 m s^{-1} Simulations with 0.5 µm Gap

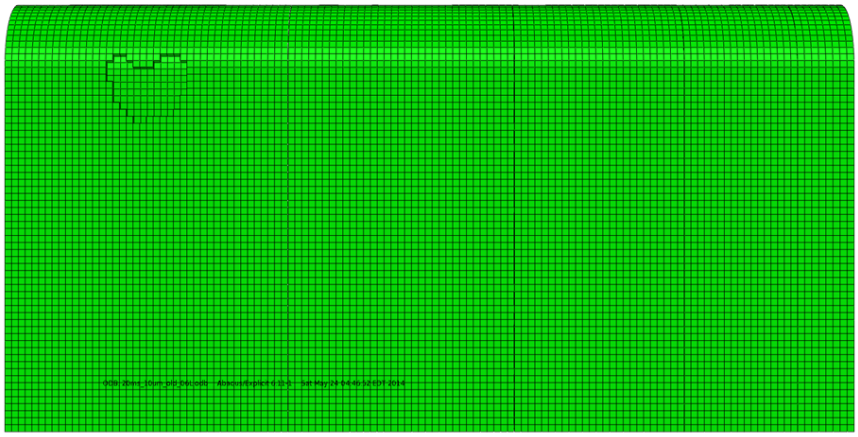

(a) Coarse Mesh

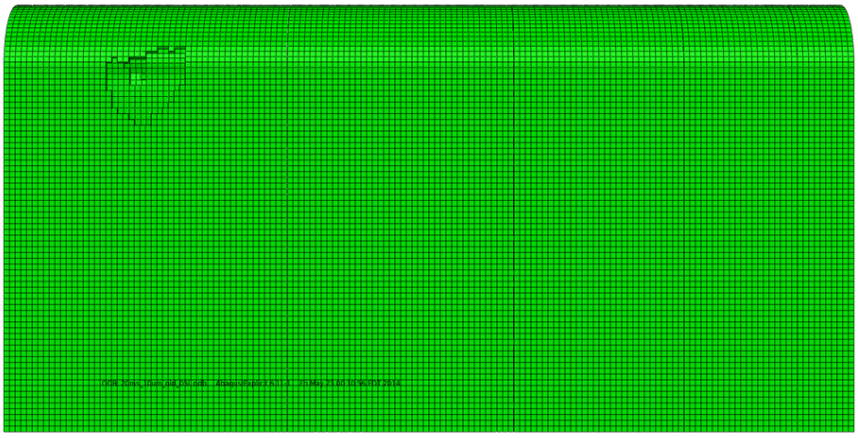

(b) Medium Mesh

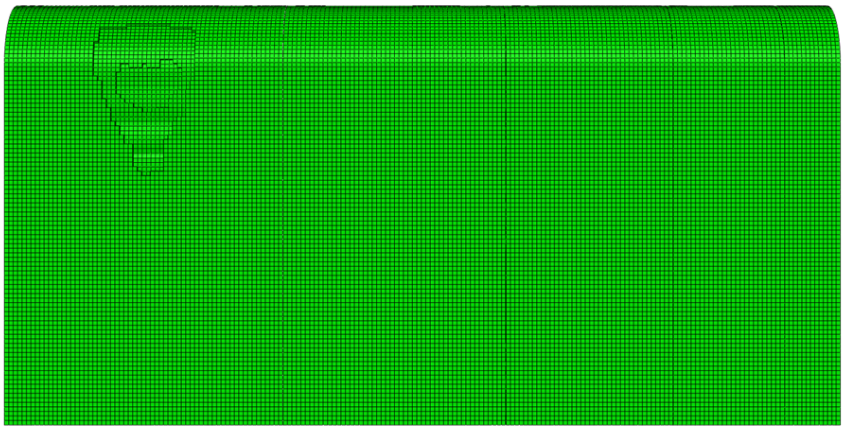

(c) Fine Mesh

Figure 4.14: Wear Patterns for 20 m s^{-1} Simulations with 1.0 µm Gap

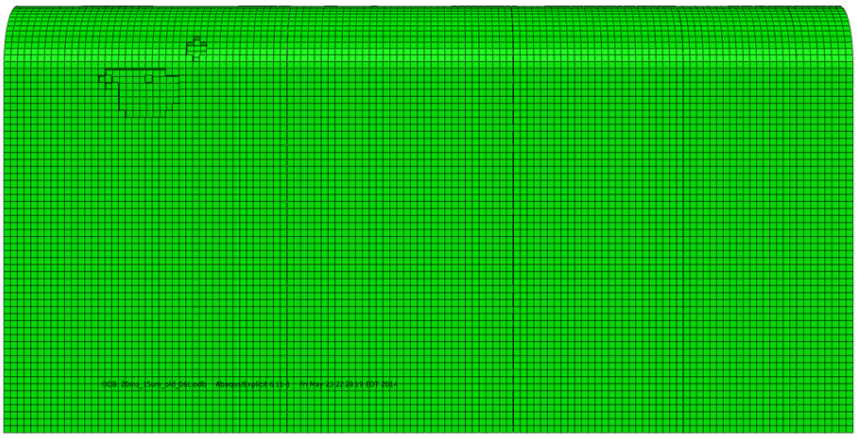

(a) Coarse Mesh

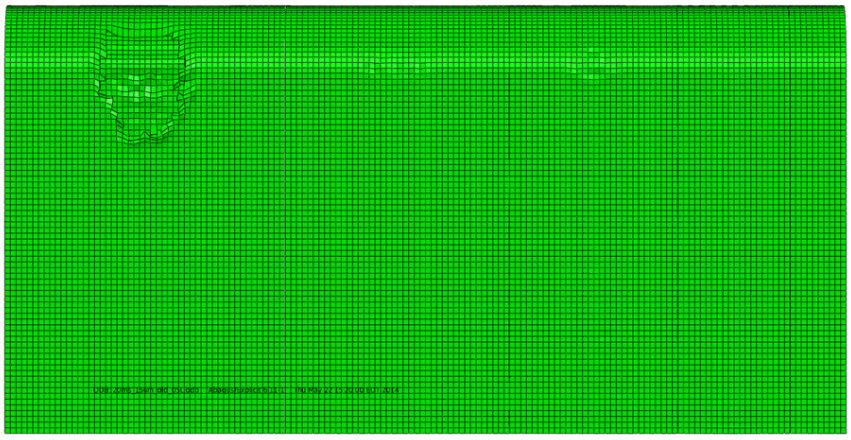

(b) Medium Mesh

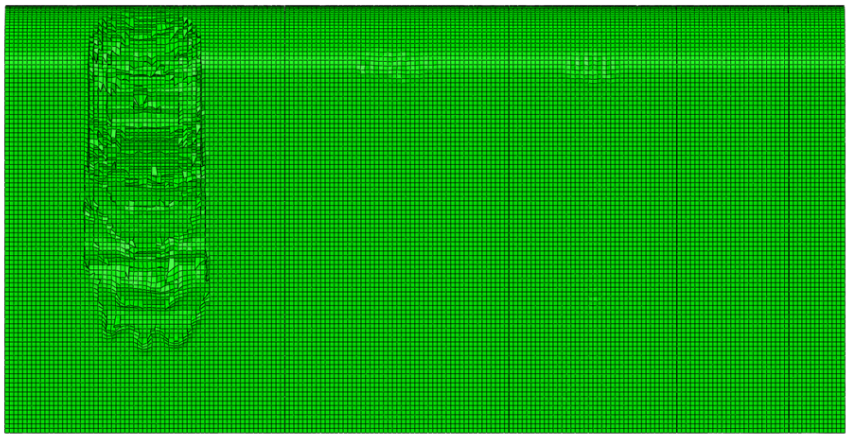

(c) Fine Mesh

Figure 4.15: Wear Patterns for 20 m s^{-1} Simulations with 1.5 µm Gap

The wear patterns, Figures 4.13 through 4.15 show the $20\,\mathrm{m\,s^{-1}}$ wear damage to the slipper wedges grouped by gap spacing for the three mesh refinements. It is interesting to note that damage caused on the wedges corresponding to the 3 μm and 4 μm asperities was only found on the fine mesh at the smallest gap spacing (Figure 4.13c). For the coarse and medium meshes, there was only damage done by the 5 μm asperity. As expected, the lower speed of this increment produced less damage.

Table 4.3: $40\,\mathrm{m\,s^{-1}}$ Simulated Wear Volumes ($V_{SA-40m/s}$)

Mesh Refinement	Gap Spacing	Volumes $\times 10^{-8}\,\mathrm{mm^3}$				
Coarse	$0.5\mu m$	0.0	0.0	0.0	1.289	1.911
	$1.0\mu m$	0.0	0.0	0.0	0.0	1.558
	$1.5\mu m$	0.0	0.0	0.0	0.0	0.496
Medium	$0.5\mu m$	0.0	0.0	0.0	0.0	2.156
	$1.0\mu m$	0.0	0.0	0.0	0.0	1.775
	$1.5\mu m$	0.0	0.0	0.0	0.0	2.672
Fine	$0.5\mu m$	0.0	0.0	0.152	2.314	2.149
	$1.0\mu m$	0.0	0.0	0.0	0.0	3.987
	$1.5\mu m$	0.0	0.0	0.0	0.0	16.315
		1 μm	2 μm	3 μm	4 μm	5 μm
		Asperity Radaii				

In the table above for the $40\,\mathrm{m\,s^{-1}}$ simulated wear volumes, it can be readily seen that the 1 μm and 2 μm asperities again, never produced any wear damage on any of the meshes no matter the gap spacing. The fine mesh model with the 0.5 μm gap spacing had the most damage due to the 3 μm, 4 μm, and 5 μm asperities. The other simulations only showed damage from the 5 μm asperity, with the exception of the 0.5 μm gap spacing on the coarse mesh which had damage due to the 4 μm asperity as well. The succeeding images show the damage on the slipper wedges for the various mesh refinements grouped by gap spacing for the $40\,\mathrm{m\,s^{-1}}$ simulations.

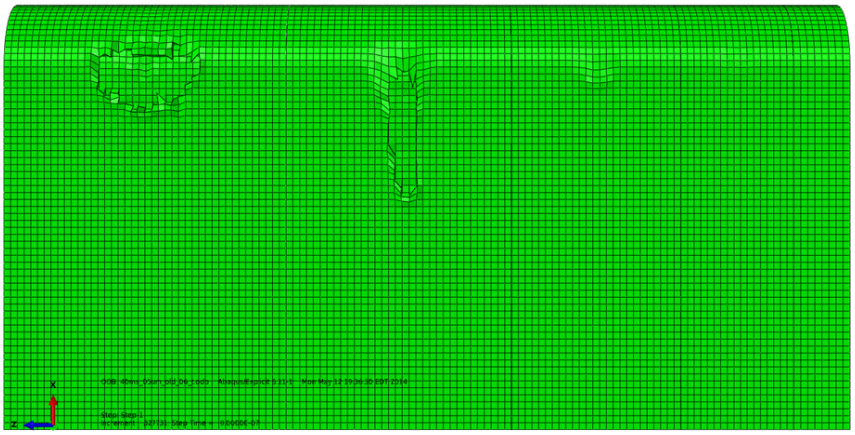

(a) Coarse Mesh

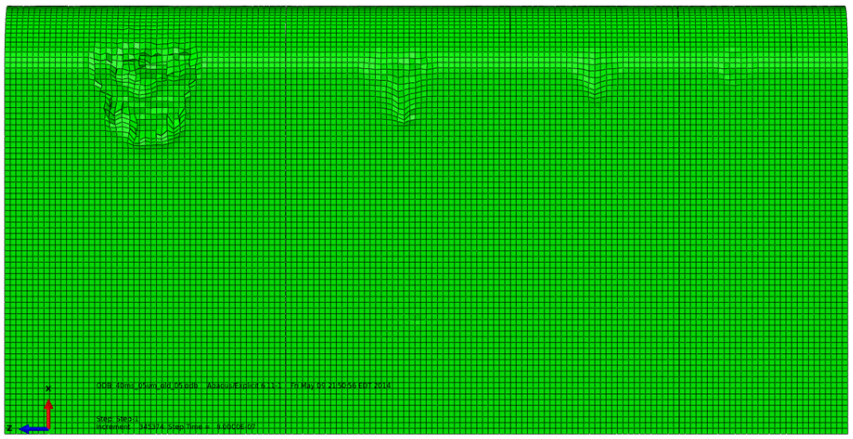

(b) Medium Mesh

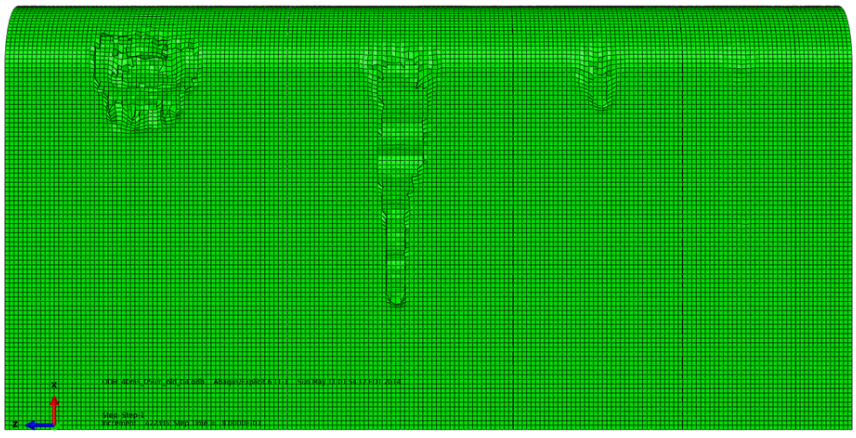

(c) Fine Mesh

Figure 4.16: Wear Patterns for 40 m s^{-1} Simulations with 0.5 µm Gap

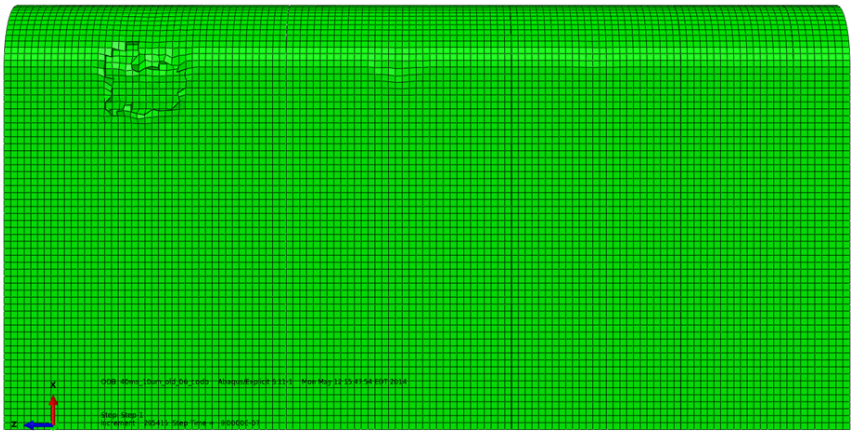

(a) Coarse Mesh

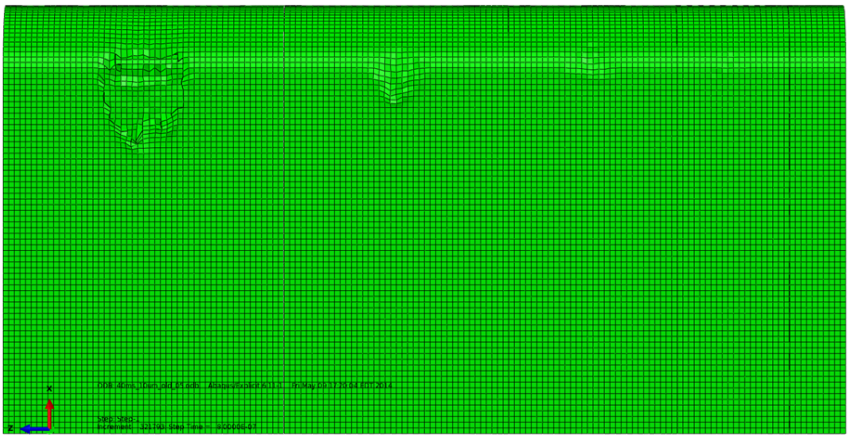

(b) Medium Mesh

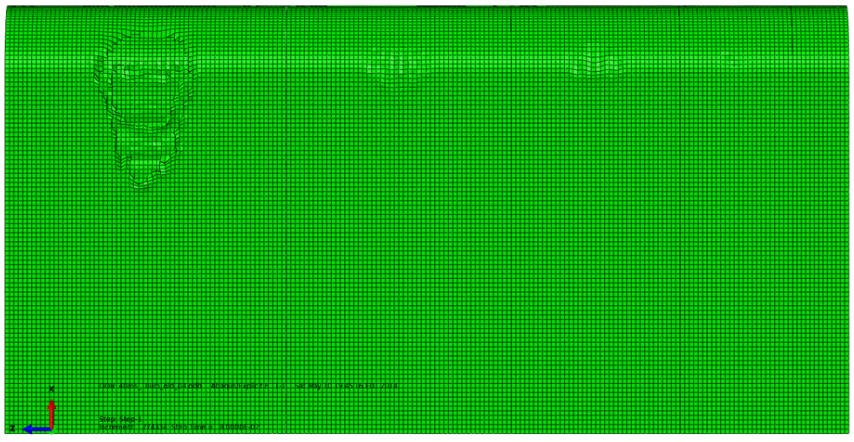

(c) Fine Mesh

Figure 4.17: Wear Patterns for 40 m s^{-1} Simulations with 1.0 µm Gap

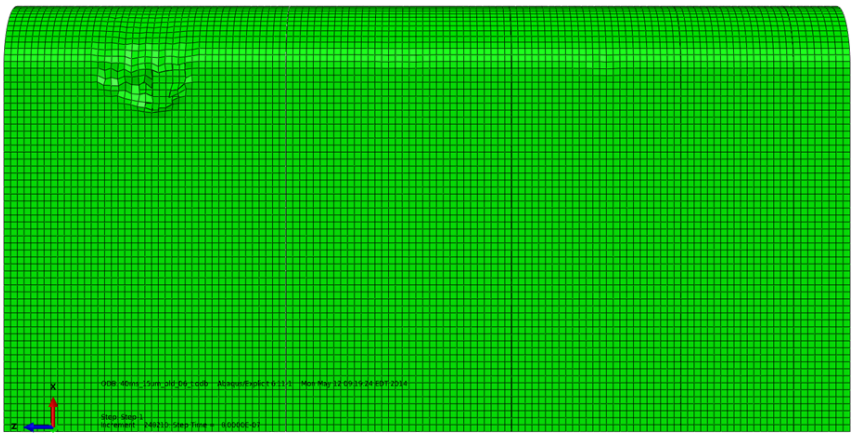

(a) Coarse Mesh

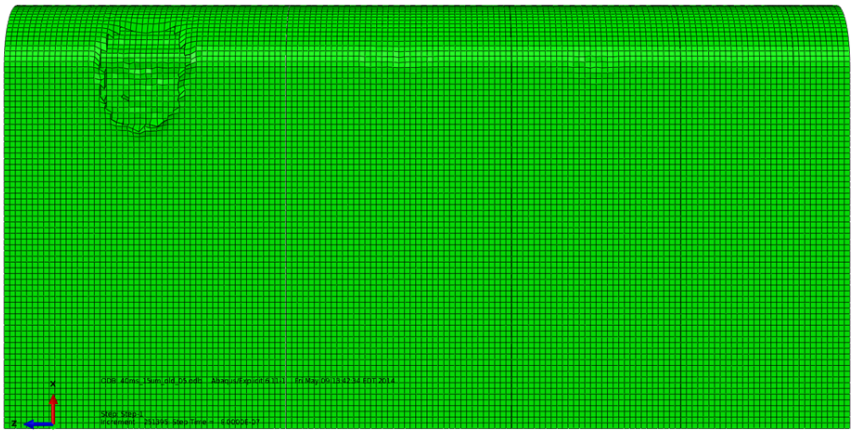

(b) Medium Mesh

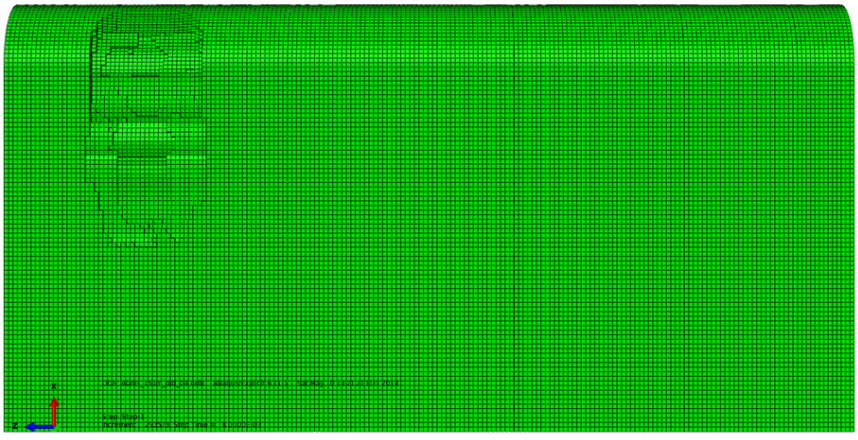

(c) Fine Mesh

Figure 4.18: Wear Patterns for 40 m s^{-1} Simulations with 1.5 µm Gap

The wear patterns, Figures 4.16 through 4.18 show the 40 m s^{-1} wear damage to the slipper wedges grouped by gap spacing for the three mesh refinements. It is interesting to note that the 4 µm asperity caused damage on the coarse and fine meshes for the 0.5 µm gap spacing but not on the medium mesh (Figure 4.17b). This would lead me to believe there may be a mesh dependence on how the damage evolution occurs in the elements. Another interesting feature is the shape and roughness of the damage on the fine mesh as compared to those of the other meshes. It appears that the fine mesh captured a lot more of the dynamic features of the impact and wear interaction than the other meshes.

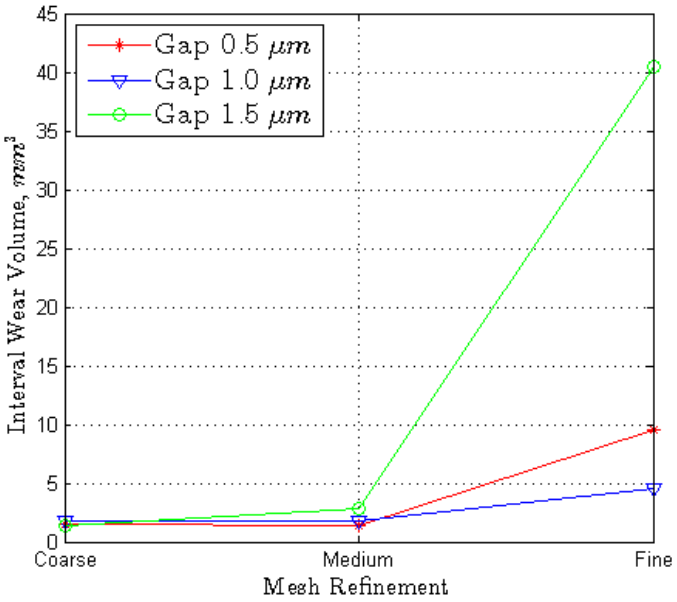

Figure 4.19: 20 m/s Wear Volume Trend as Function of Gap Size

The trend for the simulated wear volumes for the medium mesh tended to stay the same for all gap sizes whereas the trend for the fine mesh simulated wear volumes varied drastically as seen in Figures 4.19 and 4.20. The interval wear for the coarse mesh simulations at 20 m s^{-1} tended to stay the same between gaps spacings whereas the interval

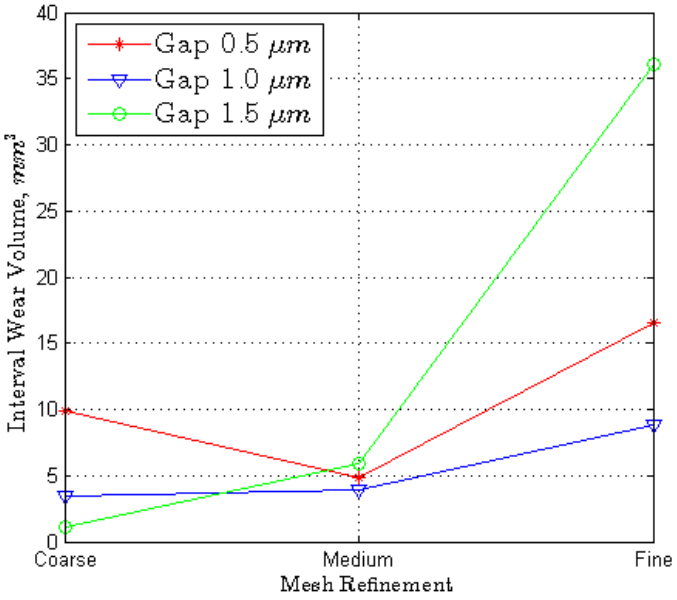

Figure 4.20: 40 m/s Wear Volume Trend as Function of Gap Size

wear for the same mesh at $40\,\mathrm{m\,s^{-1}}$ varied a bit as an inverse function of gap spacing. Meaning, as the gap was reduced, the wear volume increased. It is interesting to note that interval wear tended to increase with mesh refinement with the exception of the medium mesh at the 1.0 µm gap spacing. At this gap spacing, the interval wear decreased with the medium mesh and then increased with the fine mesh.

With the simulated wear volumes collected, the next step is to calculate the wear volume per unit area in the next section in preparation for extrapolating the wear to the under surface of the slipper.

4.2.1 Wear Volumes Per Unit Area.

The following equation[30] governs the process of calculating the wear volume per unit area, V_{uA-v}. Again, r is the radius of the asperity.

$$V_{uA-v} = \#Asp_{uA} \sum_{r=1}^{r=5} \times \%Asp_r \times V_{SA-r-v} \tag{4.4}$$

Since the asperity properties are known for a square millimeter, to normalize the wear volume per unit area requires that the square millimeter that the asperities are on, be slid a distance, D_s of 1 mm.

$$W_{uA-v} = V_{uA-v}/D_s \tag{4.5}$$

The values for $\#Asp_{uA}$ and $\#Asp_{uA}$, the number of asperities and the percent distribution of the dominant asperity sizes both per unit area, respectively, can be found in the table below.

Table 4.4: Asperity Parameters

$\# Asp_{uA}$	$\% Asp_r$				
$\#/mm^2$	$r = 1$	$r = 2$	$r = 3$	$r = 4$	$r = 5$
601	25.0	30.6	27.8	11.1	5.6

The interval wear volumes, W_{uA}, for each gap and speed increment are shown in Table 4.5 below. The largest wear volumes were not necessarily found in the simulations at $40\,m\,s^{-1}$ with the fine mesh. Surprisingly, the fine mesh with the largest gap size at $20\,m\,s^{-1}$ had the largest wear volume at $12.780 \times 10^{-6}\,mm^3/mm^3$. The same trend is seen for the $20\,m\,s^{-1}$ simulation with the same gap spacing with the coarse mesh.

Table 4.5: Wear Volumes Per Unit Area ($W_{uA}\times 10^{-6}\,mm^3/mm^3$)

Mesh	Speed Increment ($m\,s^{-1}$)	Gap Spacing		
		0.5 µm	1.0 µm	1.5 µm
Coarse	20	0.476	0.569	0.447
	40	1.503	0.524	0.167
Medium	20	0.426	0.571	0.898
	40	0.726	0.597	0.899
Fine	20	2.981	1.435	12.780
	40	2.520	1.342	5.491

It was expected that the 40 m s^{-1} simulations would have the higher amount of damage for all cases, when the simulated wear volumes are extrapolated to the asperity unit area, the 20 m s^{-1} simulations with the fine and coarse meshes with the two largest gap spacings have larger wear volumes than the 40 m s^{-1} simulations. For the fine mesh, the 20 m s^{-1} simulations always had larger wear volumes per unit area than the 40 m s^{-1} simulations. It could be that the higher downtrack velocity of the 40 m s^{-1} simulation shears off the asperity limiting the amount of damage to the slipper. Whereas the 20 m s^{-1} simulation cannot damage the asperity fast enough gaining much more damage because of it. In the next section, the wear volumes per asperity unit area will be extrapolated to the wear surface area of the real world slipper.

4.2.2 Interval Wear Volumes.

The equation governing the calculation of the interval wear volume can be found below[30].

$$V_d = \sum_{1}^{v} W_{uA_v} \times l_{c_v} \times w_{c_v} \times D_{s_v} \times \%Cont_v \tag{4.6}$$

The parameters for the length in contact, l_c, width in contact, w_c, distance slid, D_s and persent contact, $\%Cont_v$, can be found in the table below. B-H, utilized a modified length in contact for his calculation based on the front slipper, because of the pitching motion of the sled. In this research, the slipper will be assumed to be in contact with the rail across the full underside area of the slipper. As explained earlier, the sled was most likely pitching down from transmitted thrust forces being applied above the sled's center of mass, lifting the rear of the sled up. When the sled pitches back up, the rear slippers are assumed to slap down on the rail with the full contact area. The slipper is 200 mm in length and the under side contact width is 90 mm, see image below for contact width.

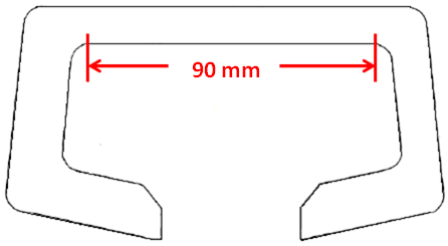

Figure 4.21: Width Of Slipper Wear Surface, w_c

Table 4.6: Parameters for Interval Wear Calculation

l_c (mm)	w_c (mm)	$D_{s_{20}}$ (mm)	$D_{s_{40}}$ (mm)	$\%Cont_{20}$ (%)	$\%Cont_{40}$ (%)
200	90	1836	3928	9.6	9.3

The interval wear volumes for the two speed increments, three gap spacings, and the three meshes can be found in Table 4.7 below.

Table 4.7: Interval Wear Volumes

Mesh	Speed Increment ($m\,s^{-1}$)	Gap Spacings		
		0.5 µm	1.0 µm	1.5 µm
Coarse	20	1.5	1.8	1.4
	40	9.9	3.4	1.1
Medium	20	1.4	1.8	2.8
	40	4.8	3.9	5.9
Fine	20	9.5	4.6	40.5
	40	16.6	8.8	36.1

4.2.3 Model Validation Through Wear Comparison.

With a multitude of wear simulations completed and the necessary data extracted, how does this compare to real world wear results? There are a three ways that this model can be validated. The first is to compare the wear results against another wear model.

The second method of validation is against the empirical wear results compiled by Lim and Ashby. By coupling the sliding velocities, $20\,\mathrm{m\,s^{-1}}$ and $40\,\mathrm{m\,s^{-1}}$, with the normalized the contact pressures as calculated from DADS data, the regime of wear can be pin-pointed on a the Lim and Ashby wear map. This part of the validation procedure is a reality check for this low speed model. Therefore, if the wear map indicates that this low speed model is experiencing seizure or melt wear, then something is wrong with the model. Lim and Ashby also published on their wear map the normalized wear volumes of various steels. The normalized wear volume values from this model should be similar, but not necessarily the same as, the other types of steels, i.e. these values should have the same order of magnitude.

The third and final validation check to increase the confidence level in the model's validity, is to calculate Archard's wear coefficients from the interval wear data. If the calculated wear coefficients fall with in the published range of Archard's wear coefficients, 5×10^{-5} when wear is mild and 5×10^{-3} when wear is severe[23], then the model is behaving as expected.

4.2.4 Model To Model Comparison.

To compare this wear research to that of B-H, the most accurate way is to match the model parameters as closely as possible. Meaning the speeds would need to be as close as possible with the same gap spacing with the same wear area, contact percentage and same mesh refinement (coarse mesh). For this comparison, the B-H simulation for a $25\,\mathrm{m\,s^{-1}}$ interval will be compared to the $20\,\mathrm{m\,s^{-1}}$ simulation with the same gap spacing. The B-H research predicted $13.9\,\mathrm{mm^3}$ using the parameters listed below in Table 4.8.

Table 4.8: B-H Parameters For 25 m s^{-1} Interval Wear Calculation

l_c (mm)	w_c (mm)	$D_{s_{25}}$ (mm)	$\%Cont_{25}$ (%)
11.1	90	6000	89.02

After applying these parameters to the simulated wear volume tabulated for the 20 m s^{-1} model in this research, the extrapolated interval wear is 2.38 mm^3. Approximately six times less wear than the B-H 25 m s^{-1} simulation. It is not surprising result since the B-H model had velocities of -1.0 m s^{-1} vertical and 25 m s^{-1} downtrack, whereas in this simulation, the vertical velocity is -0.079 m s^{-1} and the downtrack velocity is 20 m s^{-1}. The B-H research showed 1.50×10^{-6} mm^3/mm^2 for the 4 μm asperity where this model showed no wear for the same asperity. The wear that this model predicted for the 5 μm asperity is 1.328×10^{-8} mm^3 where the B-H model produced 1.02×10^{-6} mm^3 for the same asperity. It appears that the vertical velocity may play a key role in damage evolution. Below in Figures 4.22 and 4.23 are two images showing the comparison in the wear pattern for the slipper wedges that correspond to the 4 μm and 5 μm asperities. The images shown highlight the slipper wedge temperatures at the end of the simulation. It can be clearly seen that B-H slipper wedges had more of a temperature affected zone for the 4 μm and 5 μm asperities. The downward velocity may play more of a role than first expected. If the downward velocity creates a larger zone of increased temperatures, then it is possible that those elements degraded faster and were eliminated sooner in the B-H model, thereby increasing the amount of wear for that model. On the right side of Figure 4.23 is an image showing the Von Mises stress at the end of the simulation. The Mises stress pattern outlines the elements of the slipper wedge, corresponding to the 4 μm asperity, have been impacted. Without the higher downward velocity, not enough damage is generated in the wedge to cause the elements to be deleted from the model. In Figure 4.22, the average temperature of the affected zones for the B-H model is approximately 550 K and approximately 500 K

for the present model on the left side of Figure 4.23. It also appears, that not only is the temperature affected zone smaller, that it is also cooler.

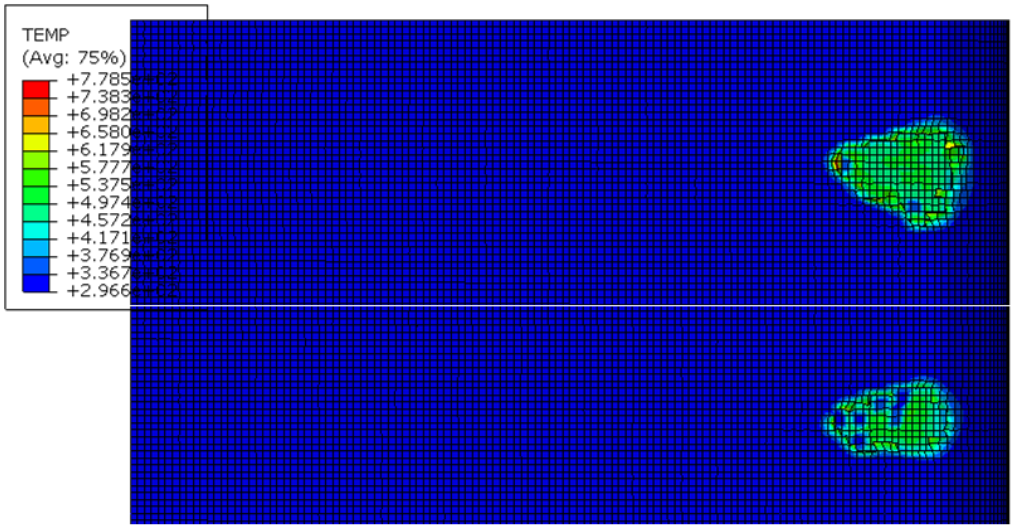

Figure 4.22: B-H 25 m s^{-1} Temperature Pattern[30]

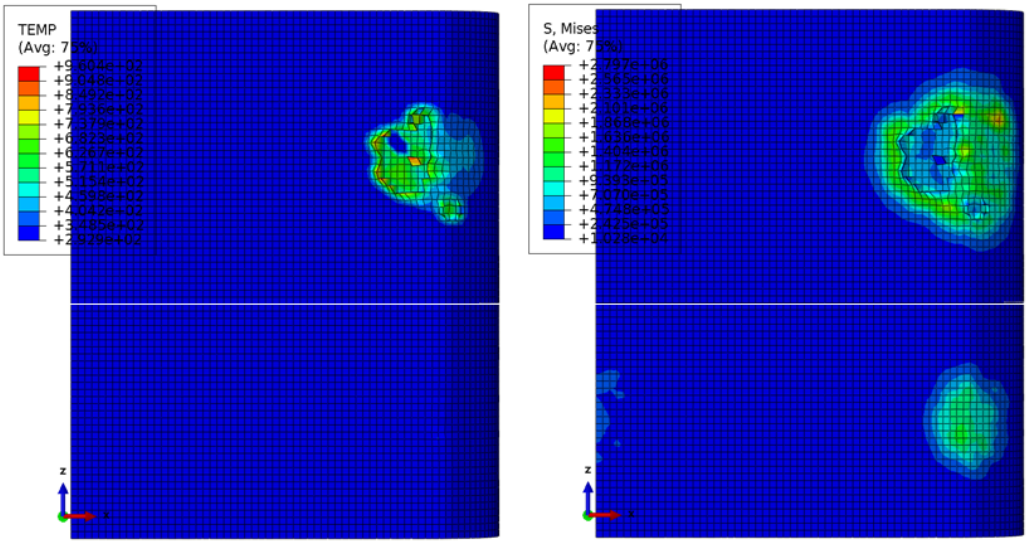

Figure 4.23: 20 m s^{-1} Temperature and Mises Stress Pattern

It is worth mentioning that since JC plasticity and fracture criterion are based on temperature, the downward velocity can play a significant role in wear evolution as increasing temperatures will tend to soften materials. This softening effect could be the difference between the model failing an element or not. The variation in temperatures is dramatic even though both these simulations are at the same gap spacing, mesh refinement and approximately the same downtrack velocity.

4.2.5 Lim and Ashby Comparison.

To compare this work to that of Lim and Ashby[23], a normalized pressure, $\tilde{F}$, for both speed increments needs to be calculated. The below figure is the Lim and Ashby wear map[3] highlighting the various wear regimes.

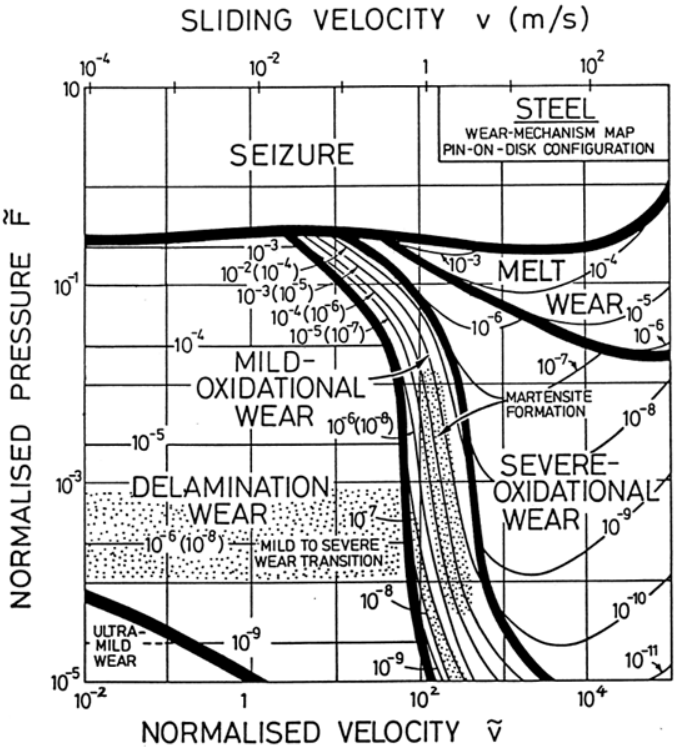

Figure 4.24: Wear Map

[3]Reprinted from Tribology International, Vol 31/edition number 1-3, S. C. Lim, Recent developments in wear mechanism maps/ Developments in various groups of wear maps, Page No. 90, Copyright (1998), with permission from Elsevier.

The normalized pressures are calculated using the equation below from the Lim and Ashby work. Where F_c is the contact force that was calculated earlier for both speed increments, A_c is the contact area and H_{vm} is the room temperature hardness of VascoMax 300. These parameters can be found in Table 4.9 below.

$$\tilde{F} = \frac{F_c}{A_c \cdot H_{vm}} \tag{4.7}$$

Table 4.9: Parameters To Calculate Normalized Pressures

Contact Length l_c (m)	Contact Width w_c (m)	Contact Area A_c (m^2)	VascoMax Hardness H_{vm} ($N\,m^{-2}$)
0.2	0.09	0.018	1.81×10^9

The values calculated for the normalized pressures can be found below in (4.8) and (4.9). These values will also be utilized later to calculate Archard's wear coefficient values for the wear volumes generated by this model.

$$\tilde{F}_{20m/s} = 5.84 \times 10^{-4} \tag{4.8}$$

$$\tilde{F}_{40m/s} = 8.00 \times 10^{-4} \tag{4.9}$$

The red oval in the Figure 4.25, shows the area bounded by a normalized pressures of about 10^{-4} to 10^{-3} and sliding velocities of $20\,\mathrm{m\,s^{-1}}$ to $40\,\mathrm{m\,s^{-1}}$. The red oval on the wear map[4] indicates that the wear experienced should be somewhere in the "mild oxidational wear" regime. A reasonable result for this low speed wear model.

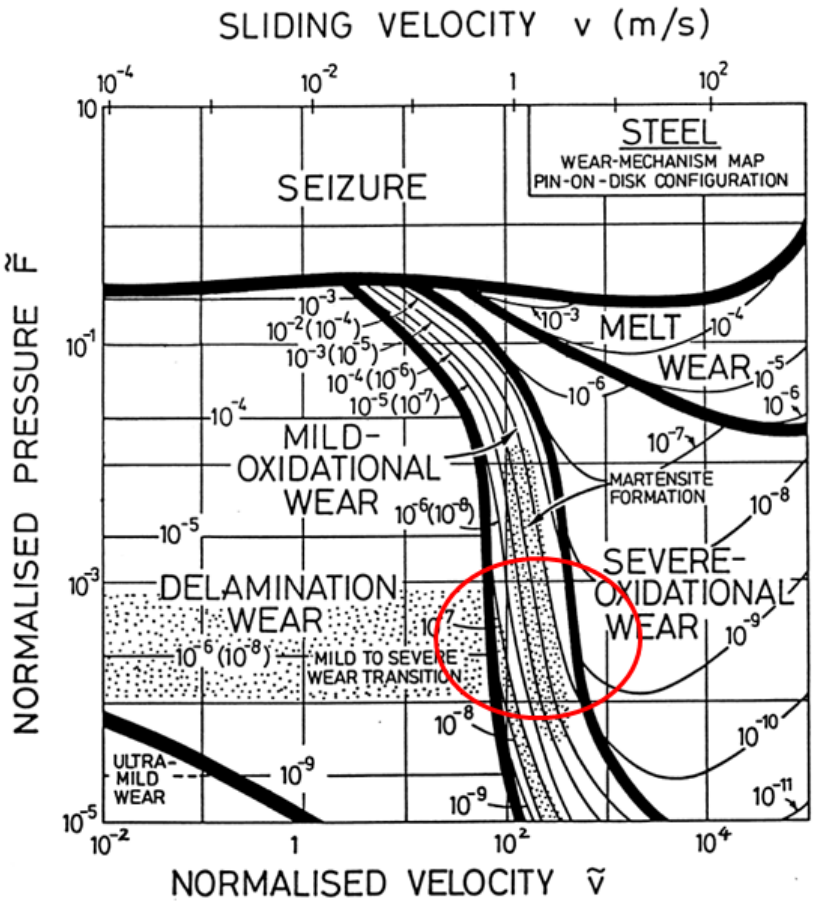

Figure 4.25: Wear Map Location

The next comparison to the Lim and Ashby results, is the rate values shown on their wear maps. But first, the normalized wear rates need to be calculated. The wear rate in

[4]Reprinted from Tribology International, Vol 31/edition number 1-3, S. C. Lim, Recent developments in wear mechanism maps/ Developments in various groups of wear maps, Page No. 90, Copyright (1998), with permission from Elsevier.

the Lim and Ashby work is the volumetric wear per distance slid. This quantity has the units of mm^2. By taking the interval wear values, V_{d-v}, from Table 4.7, and dividing by the distance slid, D_{s-v}, values from Table 4.6 and the contact area, A_c, from Table 4.9, the Lim and Ashby Normalized wear values, $\tilde{W}$ are calculated. The various normalized Lim and Ashby wear rates, governed by the two equations below, for the two selected increments and three gap sizes can be found in the Table 4.10 below.

$$W = \frac{V_d}{D_{s-v}} \tag{4.10}$$

$$\tilde{W} = \frac{W}{A_n} \tag{4.11}$$

Table 4.10: Normalized Wear Rates For Lim and Ashby Comparison

Mesh Refinement	Speed Increment ($m\,s^{-1}$)	Normalized Wear Rates		
Coarse	20	4.57e-8	5.46e-8	4.29e-8
	40	1.40e-7	4.88e-8	1.55e-8
Medium	20	4.09e-8	5.48e-8	8.62e-8
	40	6.75e-8	5.56e-8	8.36e-8
Fine	20	2.86e-7	1.38e-7	1.23e-6
	40	2.34e-7	1.25e-7	5.11e-7
		$0.5\mu m$	$1.0\mu m$	$1.5\mu m$
		Gap Spacing		

Now that the normalized wear rates are computed, to compare to the results published by Lim and Ashby the Log_{10} of the values need to be taken. These values can be found in the Table 4.11 below.

Table 4.11: Log_{10} of Normalized Wear Rates

Mesh Refinement	Speed Increment ($m\,s^{-1}$)	Normalized Wear Rates		
Coarse	20	-7.3	-7.3	-7.4
	40	-6.9	-7.3	-7.8
Medium	20	-7.4	-7.3	-7.1
	40	-7.2	-7.3	-7.1
Fine	20	-6.5	-6.9	-5.9
	40	-6.6	-6.9	-6.3
		$0.5\mu m$	$1.0\mu m$	$1.5\mu m$
		Gap Spacing		

The values in Table 4.11 range from -7.4 to -5.9 for the $20\,m\,s^{-1}$ speed increment and from -7.8 to -6.3 for the $40\,m\,s^{-1}$ speed increment. These values when compared to the low carbon steel data in the Figure[5] 4.26 shown below are very similar and in the same area as identified by the red oval earlier. It appears that the modeled wear for the VascoMax 300 steel slipper compares nicely to the Lim and Ashby Data for wear rates.

4.2.6 Archard's Wear Coefficient Comparison.

In 1953, British researcher John F. Archard developed a wear model based on wear, load and on the probability that an asperity in contact with another asperity would produce a wear particle. Lim and Ashby modified a simple form of Archard's wear model for it

[5]Reprinted from Acta metal, Vol 35/edition number 1, S. C. Lim and M. F. Ashby, Wear-Mechanism maps/ Empirical mechanism maps, Page No. 3, Copyright (1987), with permission from Elsevier.

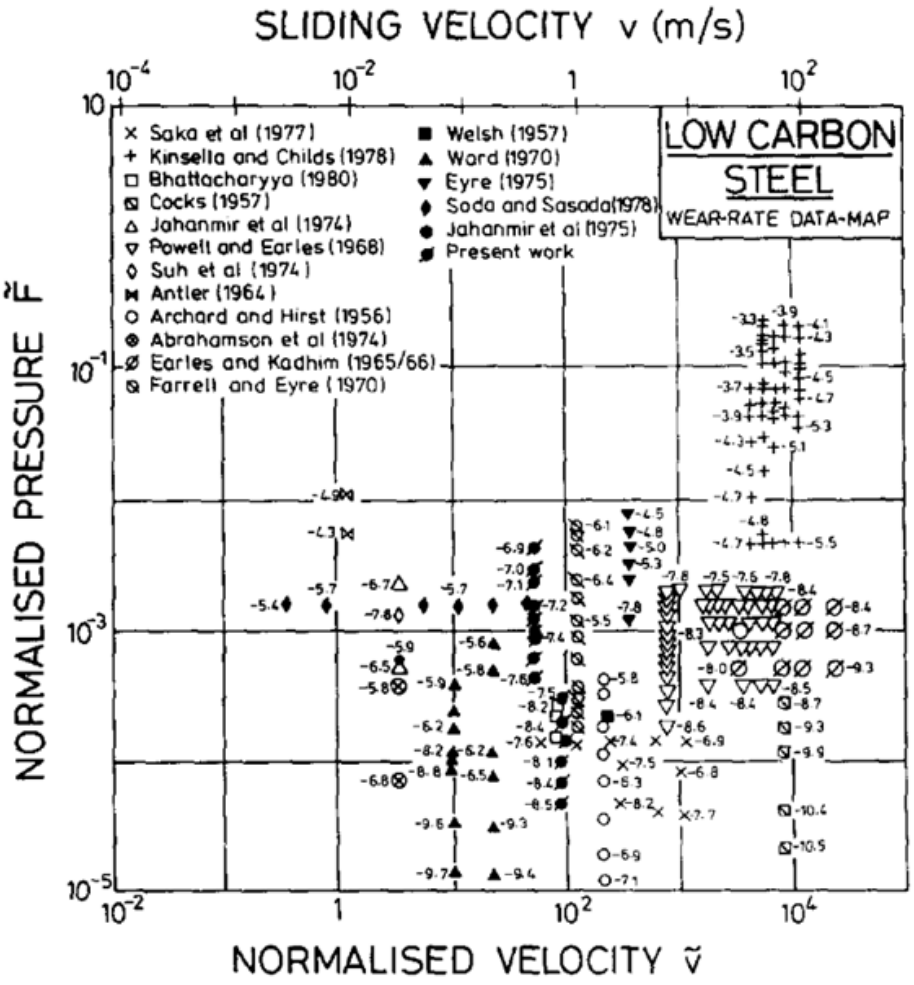

Figure 4.26: Low Carbon Steel Wear Map

to apply to different wear regimes and mechanisms. The simplest version of the Archar's wear coefficient utilizing the Lim and Ashby normalized parameters, $\tilde{W}$ and $\tilde{F}$ is shown below.

$$k_A = \frac{\tilde{W}}{\tilde{F}} \tag{4.12}$$

By applying the values for $\tilde{F}_{20m/s}$ and $\tilde{F}_{40m/s}$ to the above $\tilde{W}$ values for normalized wear, in Table 4.10, Archard's wear coefficients can be calculated according to the equation

above, taken from Lim and Ashby[23]. According to Archard[4] the range of reasonable values are 10^{-5} to 10^{-3}. With $k_A = 10^{-5}$ being mild wear and $k_A = 10^{-3}$ being severe wear. Below in Table 4.12, are the calculated values for Archard's wear coefficient.

Table 4.12: Archard's Wear Coefficients For Model Data

Mesh Refinement	Speed Increment ($m\,s^{-1}$)	Normalized Wear Rates		
Coarse	20	7.83e-5	9.36e-5	7.35e-5
	40	1.75e-4	6.10e-5	1.94e-5
Medium	20	7.00e-5	9.39e-5	1.48e-4
	40	8.44e-5	6.94e-5	1.05e-4
Fine	20	4.90e-4	2.36e-4	2.10e-3
	40	2.93e-4	1.56e-4	6.38e-4
		$0.5\mu m$	$1.0\mu m$	$1.5\mu m$
		Gap Spacing		

It can be seen from the above data, that Archard's wear coefficients range from 7×10^{-6} to 2×10^{-4} for the $20\,m\,s^{-1}$ speed increment and from 4×10^{-6} to 1×10^{-4} for the $40\,m\,s^{-1}$ speed increment. This result indicates that for this low speed model the Archard's wear coefficient values calculated from modeled wear volumes indicate a reasonable wear regime. This is a logical result for the given velocities and surface roughnesses modeled herein. This is another point of validation for this low speed wear model.

4.2.7 40 m/s Model With Updated Parameters.

In the B-H research, it was noted how dramatic of an effect the specific heat of the materials had on the amount of wear tabulated. In his research, two values for the Vasco-Max 300 specific heat were used, one for low temperature and one for high temperature. It

was assumed, since VascoMax 300 specific heat values were not available, that the values should be close to that of AISI-1080 steel. The two specific heat values used were for 293 K and 488 K, 4.9 $mm^2\,K^{-1}\,s^{-2}$ and 7.0 $mm^2\,K^{-1}\,s^{-2}$, respectively. All of the B-H simulations were done twice, first with the low C_p value for VascoMax and then with the high C_p value.

For area of research, the fine and coarse mesh models were set at 40 $m\,s^{-1}$ with a gap spacing of 0.5 μm. The variations included updating the single, "static", specific heat values with tables, substituting the high strain rate JC plasticity parameters with low strain rate parameters, and then applying both updates. The three different scenarios were simulated by modifying the input files from the previous runs with the results compared to the original simulation results. The JC plasticity parameters and updated specific heat tables can be found earlier in Chapter 2. The results of applying these updates can be found in table 4.13 below.

Table 4.13: Interval Wear Comparison for Material Parameter Updates

Updated Parameters	Fine Mesh Model	Coarse Mesh Model
Original Results	16.6	9.9
Cp Table Update	6.0	4.4
JC Plasticity Update	2.4	1.4
Cp tables and JC Plasticity	2.8	3.3

Not only did applying the updates singly reduce the amount of wear, the combined effect did so as well. Updating the specific heat capacities had an even larger effect than updating the plasticity parameters. When both modifications were applied, the end result was lower than those of just the specific heat capacity update alone. This result shows

that it is imperative that if wear is to be modeled as accurately as possible, having the best possible material parameters is a must and can have far reaching implications as the previous modeling efforts may have overestimated wear damage, unnecessarily driving design changes that were based on those wear models. Below are the wear pattern images for both the fine mesh and coarse mesh models.

Figure 4.27: Fine Mesh with Updated C_p Table

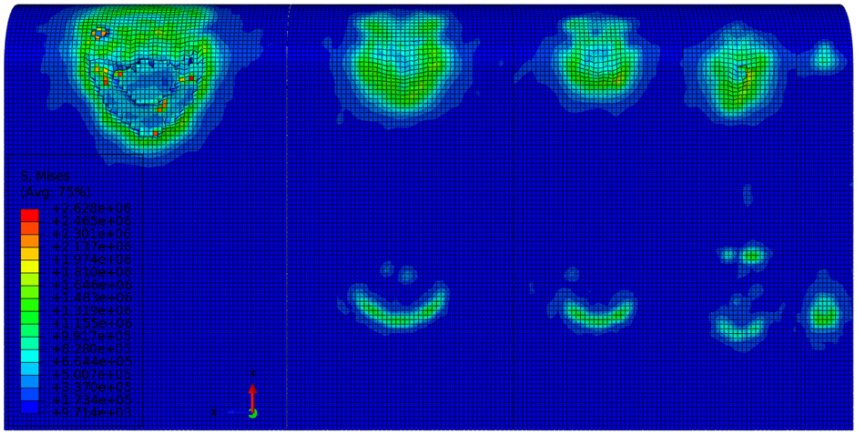

Figure 4.28: Fine Mesh with Updated Plasticity Parameters

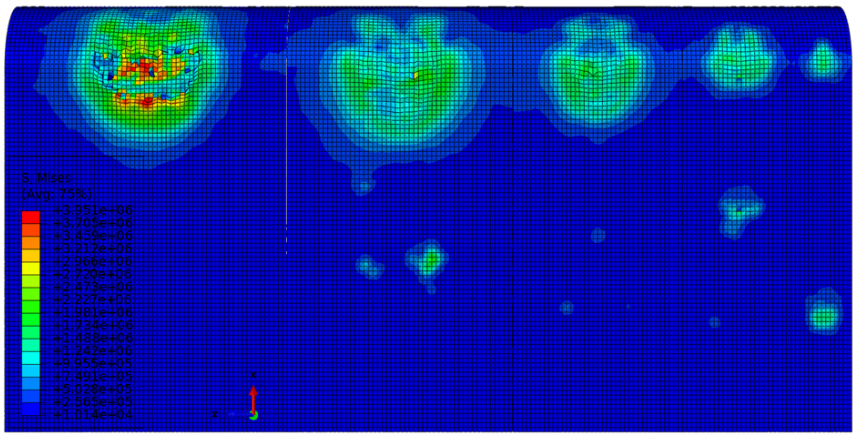

In Figure 4.27 above it can be seen that there is more damage from the 5 µm asperity with the specific heat capacity table applied than in the model, Figure 4.28, where the updated plasticity parameters are applied. The stresses appear higher in the contact area between the asperity and the slipper wedge for the model with the updated plasticity parameters than the model with the updated specific heat capacity tables.

Figure 4.29: Fine Mesh with Updated C_p Tables and Plasticity Parameters

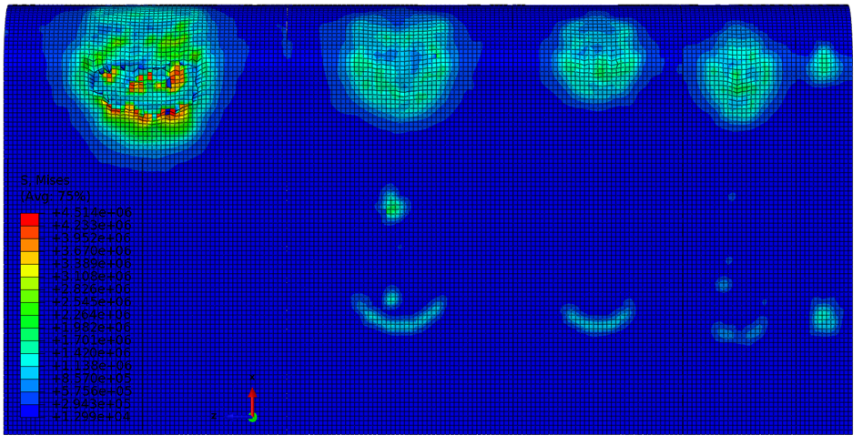

In the Von Mises stress figure of the model with both updates applied, Figure 4.29, the image appears to be a hybrid of both previous images. The stresses are higher but there is less damage than the model with updated specific heat capacity tables.

The coarse mesh model with the same updates showed the same trends in interval wear volume as the fine mesh model. There was just less damage for the coarse mesh model as compared to the fine mesh model. There was more damage in the model with the updated specific heat capacity tables than the model with the updated plasticity parameters. Both models with updates had less damage than the original model. When the coarse mesh model is compared to the fine mesh model, both with the plasticity update applied, the stresses in the latter are higher.

Figure 4.30: Coarse Mesh with Updated C_p Tables

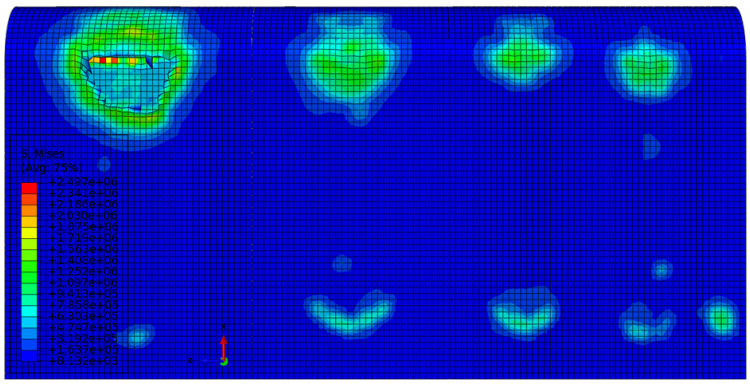

Figure 4.31: Coarse Mesh with Updated Plasticity Parameters

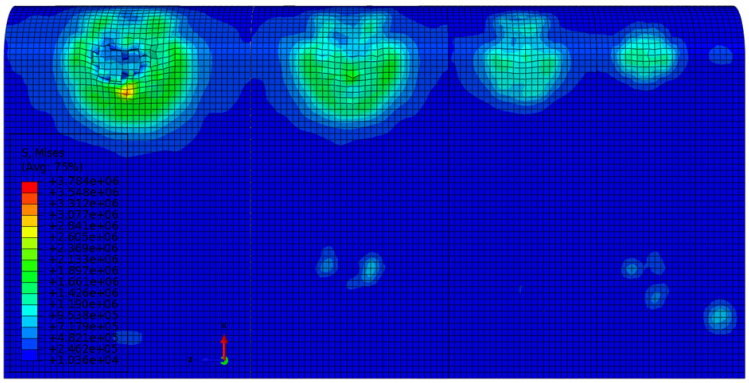

Figure 4.32: Coarse Mesh with Updated C_p Tables and Plasticity Parameters

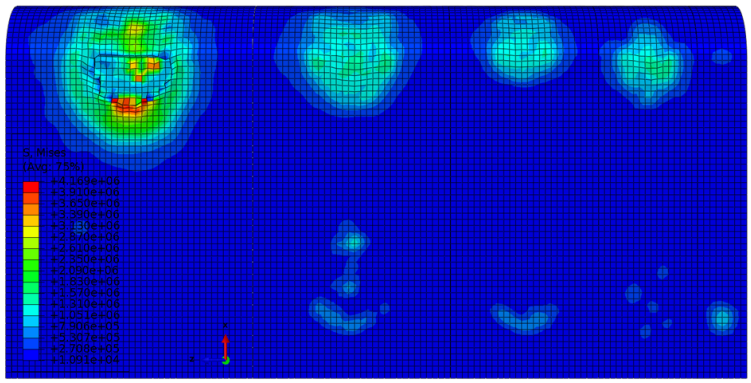

It has been shown how incredible an effect changing the material parameters could have what if something as simple as smoothing out the asperity root with a fillet? A model with filleted asperities was run at $40\,\mathrm{m\,s^{-1}}$ at three gap spacings with the fine mesh. A detailed discussion of the results of this model can be found in Appendix A.

V. Conclusions and Recommendations

5.1 Research Overview

The purpose of this chapter is to outline the conclusions of this micro-scale finite element mechanical wear modeling effort based on a HHSTT 2008 hypersonic rocket sled test. The purpose of studying this type of mission is two fold. First, in the Track's controlled test environment, accurate and abundant test data is available to study and apply to modeling and simulation. Second, a rocket sled mission offers the opportunity to study the extremes of wear modeling with both high and low speeds as well as access to testing a variety of slipper materials in this severe wear environment. For this work, A VascoMax 300 slipper was modeled impacting AISI-1080 steel rail asperities. The two speed increments studied were $20\,\mathrm{m\,s^{-1}}$ and $40\,\mathrm{m\,s^{-1}}$. Within these two speed increments, five asperity sizes were used to mimic the surface roughness of the rail. The surface characteristics of the VascoMax slipper was simulated with leading edge radius of $6\,\mu\mathrm{m}$. For each of the speed increments, three different finite element meshes were matched up, coarse, medium and fine. The mesh refinements are based on the size of the elements used in the slipper wedge meshes. For all these simulations, three gap spacings, $0.5\,\mu\mathrm{m}$, $1.0\,\mu\mathrm{m}$, and $1.5\,\mu\mathrm{m}$, between the slipper and rail were explored to better model the surface roughness interaction of the two materials. Totaling a number of eighteen simulations run for the bulk of this work. In addition to the eighteen, six more simulations were completed that explored the variation in the damage of the fine and coarse meshes when the material properties, such as specific heat capacity tables and Johnson-Cook plasticity parameters, were updated to be more realistic.

5.2 Conclusions of Research

In this work, it was found that of the two speed increments, the one with the higher speed, $40\,\mathrm{m\,s^{-1}}$, usually had more wear, i.e. higher wear volumes, than the slower. The two exceptions to this statement are the two $20\,\mathrm{m\,s^{-1}}$ simulations at the $1.5\,\mu\mathrm{m}$ gap spacing with the coarse and fine meshes. The $20\,\mathrm{m\,s^{-1}}$ simulations for these had larger interval wear amounts. As the meshes were refined the amount of damage tended to increase. In one instance, for the $1.0\,\mu\mathrm{m}$ gap spacing, the damage trended down for the medium mesh then back up again for the fine mesh. This model was compared to the results of a predecessor model. The Buentello Hernandez model predicted $13.9\,\mathrm{mm^3}$ while this model predicted $2.38\,\mathrm{mm^3}$ six times less wear. This lower value for wear volume, was expected to be less then the Buentello Hernandez result since the downtrack and vertical velocities are higher for the Buentello Hernandez model. The higher velocities would be expected to cause more wear damage. It appears that the down ward velocity plays an important role in the damage evolution in the model.

The results of this effort were compared to empirical research compiled by Lim and Ashby[23]. The model was found to be very much ”in the ball park” with respect to the amount of damage incurred for the given speeds and the damage extrapolation method used that was developed by Buentello[30]. By utilizing the normalized pressures for both the $20\,\mathrm{m\,s^{-1}}$ and $40\,\mathrm{m\,s^{-1}}$ speed increments, and the speed increments themselves, a wear regime was pinpointed on the Lim and Ashby wear map. Taking this analysis a step further, the wear volumes collected from this model were normalized as Lim and Ashby normalized the empirical wear results. What was discovered, was that the values matched the wear map results very well to those of other types of steels. The log_{10} of the normalized interval wear volumes yielded wear rates that ranged from -5.9 to -7.4 for the $20\,\mathrm{m\,s^{-1}}$ speed increment and from -6.3 to -7.8 for the $40\,\mathrm{m\,s^{-1}}$ speed increment. The final step in this Lim and Ashby comparison of numerical wear to empirical wear entailed utilizing the

normalized interval wear volumes and the normalized pressures to calculate Archard wear coefficient values. The values ranged from 7×10^{-5} f to 2×10^{-3} for the for the $20\,\mathrm{m\,s^{-1}}$ speed increment and from 2×10^{-5} to 6×10^{-4} for the $40\,\mathrm{m\,s^{-1}}$ speed increment.

Additional simulations were carried out comparing the fine and coarse mesh models at $40\,\mathrm{m\,s^{-1}}$ and a $0.5\,\mu\mathrm{m}$ gap spacing with updated material parameters. This speed and gap spacing was chosen based on the fact that these simulations exhibited the most wear of all the runs. These simulation were carried out in three different ways. First, the static specific heat capacities were updated with a table of values. Second, the static specific heat capacity values were kept and the Johnson-Cook plasticity parameters were exchanged with low strain rate versions, more applicable to this modeling effort. Lastly, both the specific heat capacity tables and the low strain rate Johnson-Cook plasticity parameters were used. What was discovered was startling the amount of wear damage dramatically changed, the fine mesh model reported $6\,\mathrm{mm^3}$ of wear for the updated specific heat capacity parameters while the coarse mesh reported $4.4\,\mathrm{mm^3}$. With the updated Johnson Cook plasticity parameters the fine mesh model reported $2.4\,\mathrm{mm^3}$ and the coarse mesh model reported $1.4\,\mathrm{mm^3}$. When the updates were combined, the fine mesh model reported $2.8\,\mathrm{mm^3}$ and the coarse mesh model reported $3.3\,\mathrm{mm^3}$ of wear as opposed to the original model results of $16.6\,\mathrm{mm^3}$ for the fine mesh model and $9.9\,\mathrm{mm^3}$ for the coarse mesh model.

5.3 Significance of Research

The significance of this wear modeling effort are two fold. First, the high speed model created by Buentello Hernandez[30] was validated at low speeds by comparing the simulated results against empirical wear results. Second, it was highlighted that by having accurate material properties such as plasticity parameters and specific heat capacity tables, the amount of simulated wear can be better known. Leading to potentially more efficient design solutions with reduced material usage, lowered cost and simplified manufacturing processes.

5.4 Recommendations For Future Work

There are three recommendations for future work:

- Develop a more accurate specific heat capacity function for VascoMax 300
- Combine the effects of updated material parameters with an asperity root fillet to more accurately predict wear.
- Perform a more in-depth convergence study to uncover the association between wear damage and mesh refinement

The combined effects of these recommendations would allow for a more refined and accurate wear model.

5.5 Summary of Research

In summary, a low speed portion of a 2008 Holloman High Speed Test Track hypersonic sled test mission was modeled to discover wear rates at $20\,\mathrm{m\,s^{-1}}$ and $40\,\mathrm{m\,s^{-1}}$. Three gap spacings between the slipper and rail were used to mimic the surface roughness of the materials modeled as discovered with laser profilometry[31]. Within the two speed increments and three gap spacings, three different mesh refinements were also explored. It was found that the model's results were found to agree quite well with the results reported by Lim and Ashby as the wear rates of the VascoMax 300 steel slippers matched the wear rates of other steels found in the same area on the Lim and Ashby wear map. The Archard's wear coefficients were calculated using the wear volumes reported by the model and they all fell in the range specified by Archard, 10^{-5} to 10^{-3}. The importance of accurate material properties was shown through the use of updated specific heat capacity tables and Johnson Cook plasticity parameters, leading to fundamentally different wear results. A fundamental behavioral difference was found depending on how the asperities were modeled, as just a hemispherical feature or with a root fillet to smooth out any potential singularities.

Appendix: Cavallaro-Baker Model

After the primary evaluations were carried out, Dr. William Baker suggested that a fillet at the base of the asperity was more practical and thus an extra study was carried out to see the effect this modification had to the total wear. The $40\,\mathrm{m\,s^{-1}}$, fine mesh model was modified and the three different gaps spacings were used. The differences between the two different asperity blocks can be found below. A $1\,\mu\mathrm{m}$ radius fillet tangent to both the asperity hemisphere and the asperity block was used. The difference between the two models can be seen in Figures A.1 and A.2 below.

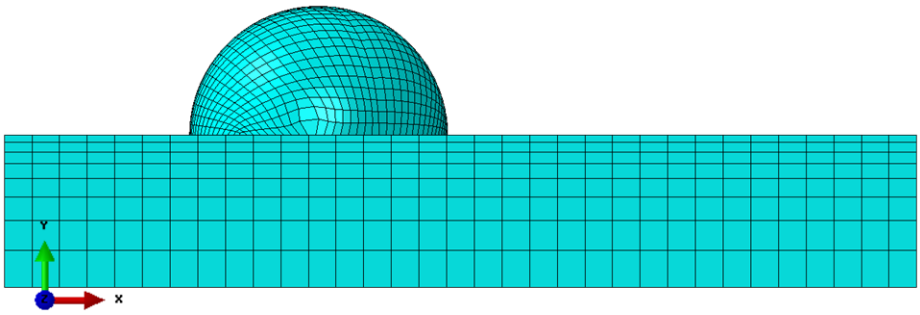

Figure A.1: Original Model Asperity

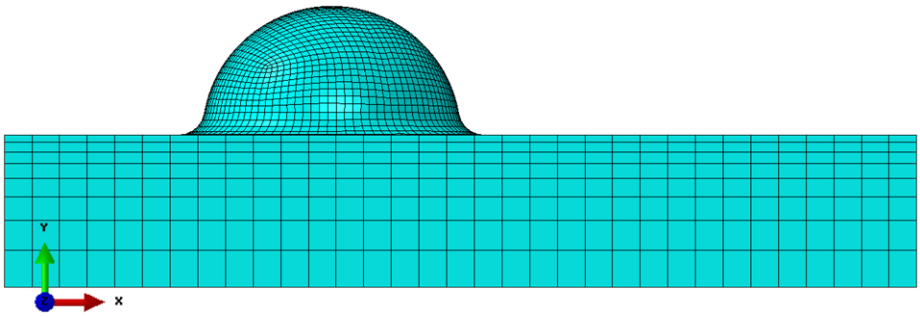

Figure A.2: Baker Model Asperity

In the succeeding images a side by side comparison by frame number can be seen. Each frame is equal to 8 ns. What is shown is the asperity deformation for the 40 m s^{-1} simulation with the fine mesh and a gap spacing of 1.5 µm without the slipper wedges complicating the view. The difference in the behavior of the two models can clearly be seen by frame 30, Figures A.5 and A.6, below.

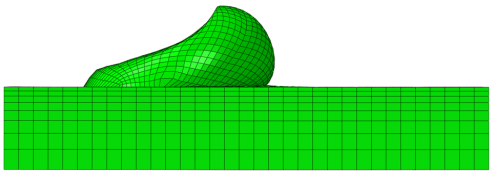

Figure A.3: Original Asp Frame 20

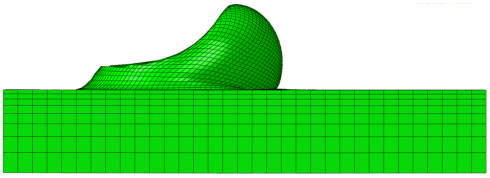

Figure A.4: Baker Asp Frame 20

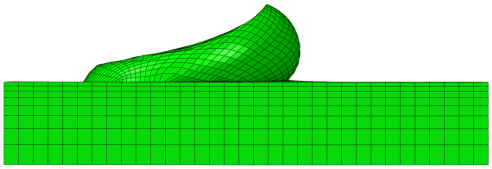

Figure A.5: Original Asp Frame 30

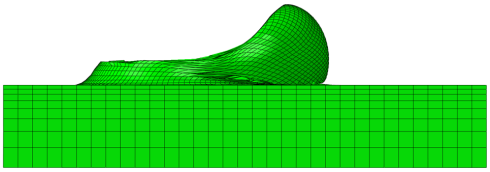

Figure A.6: Baker Asp Frame 30

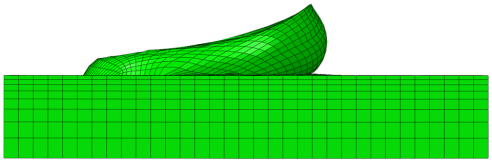

Figure A.7: Original Asp Frame 40

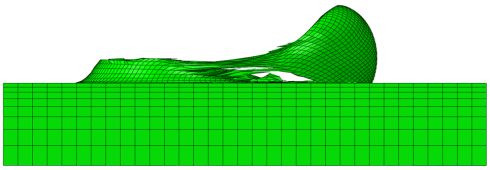

Figure A.8: Baker Asp Frame 40

The 5 µm asperity appears to fracture and the asperity is sheared off at a much earlier time than previously seen. In Figure A.6 above, the fracture in the asperity can be clearly

seen below the asperity top. By the 40th frame, the asperity has pretty much been ripped clean off. In frame 50 shown below in Figure A.10, pieces of the fracturing asperity have become separated from the main asperity body. This trend continues to frame 100 while the original asperity appears to just deform to the right.

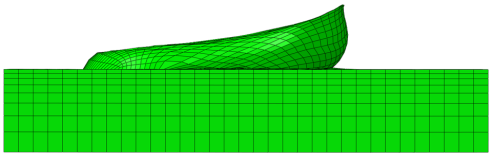

Figure A.9: Original Asp Frame 50

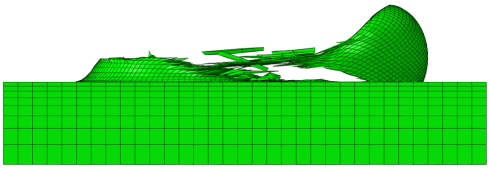

Figure A.10: Baker Asp Frame 50

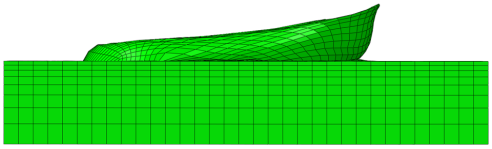

Figure A.11: Original Asp Frame 60

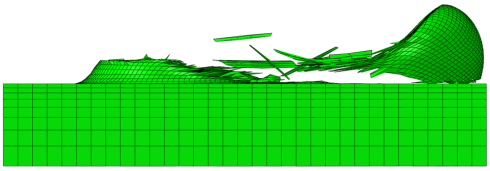

Figure A.12: Baker Asp Frame 60

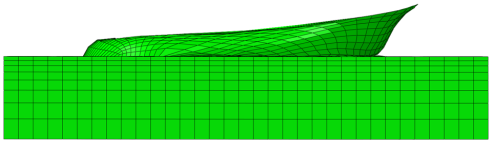

Figure A.13: Original Asp Frame 70

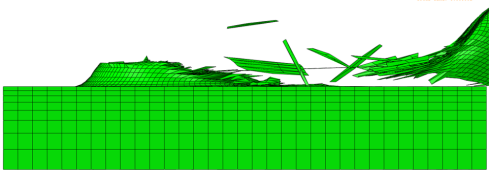

Figure A.14: Baker Asp Frame 70

It is interesting to note that in the original model, the asperity 5 μm asperity always produced damage no matter the speed, gap spacing or mesh refinement. For the Baker

asperity simulation, no damage was caused by the largest asperity. There was only minor damage found, caused by the 3 µm asperity.

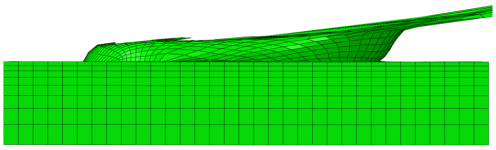

Figure A.15: Original Asp Frame 80

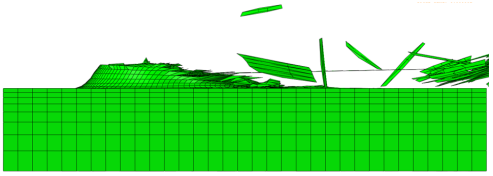

Figure A.16: Baker Asp Frame 80

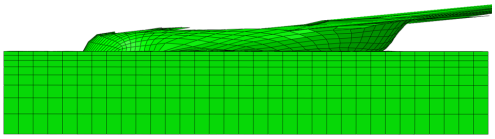

Figure A.17: Original Asp Frame 90

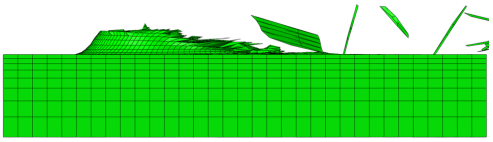

Figure A.18: Baker Asp Frame 90

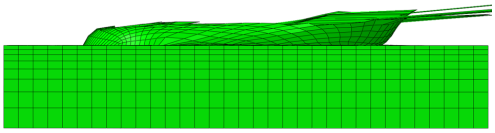

Figure A.19: Original Asp Frame 100

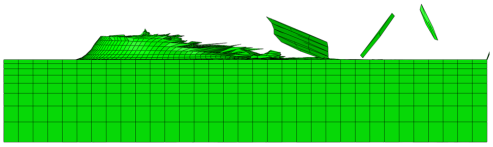

Figure A.20: Baker Asp Frame 100

The 40 m s^{-1}, fine mesh wear patterns for the three gap spacings can be found below. With this version of the model, it is difficult to call the Baker damage an actual wear patter. As there is not real pattern of damage in the slipper, only a smattering of damaged elements. The damage to the slipper wedges can be found in the red lined areas. The root radius of the asperity in the Baker model appears to have stiffened the asperity to a point where it's

damage and degradation is rather quick. Leading to very little damage in the slipper. Below are figures comparing the wear patterns.

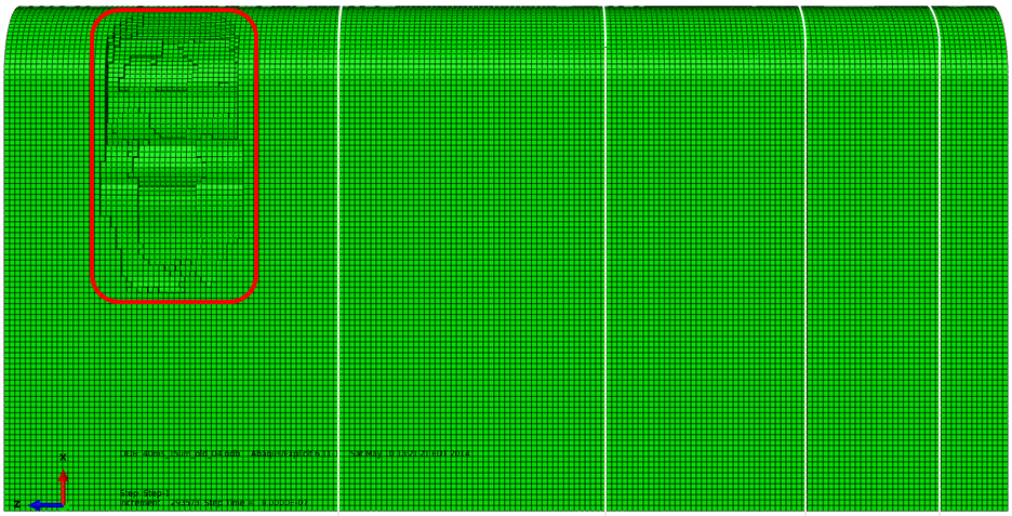

Figure A.21: Original Wear Pattern For 40 m s^{-1}, 1.5 µm Gap, and Fine Mesh

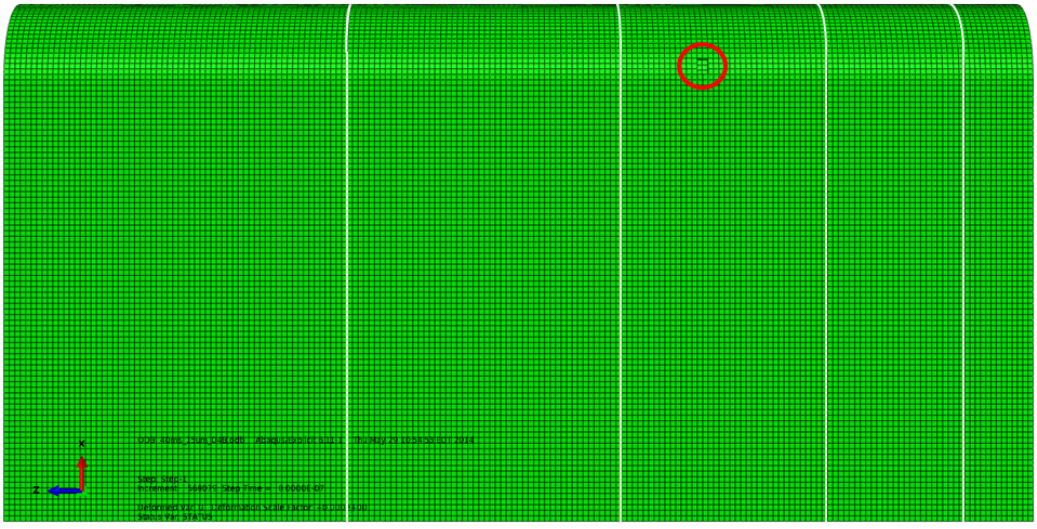

Figure A.22: Baker Wear Pattern For 40 m s^{-1}, 1.5 µm Gap, and Fine Mesh

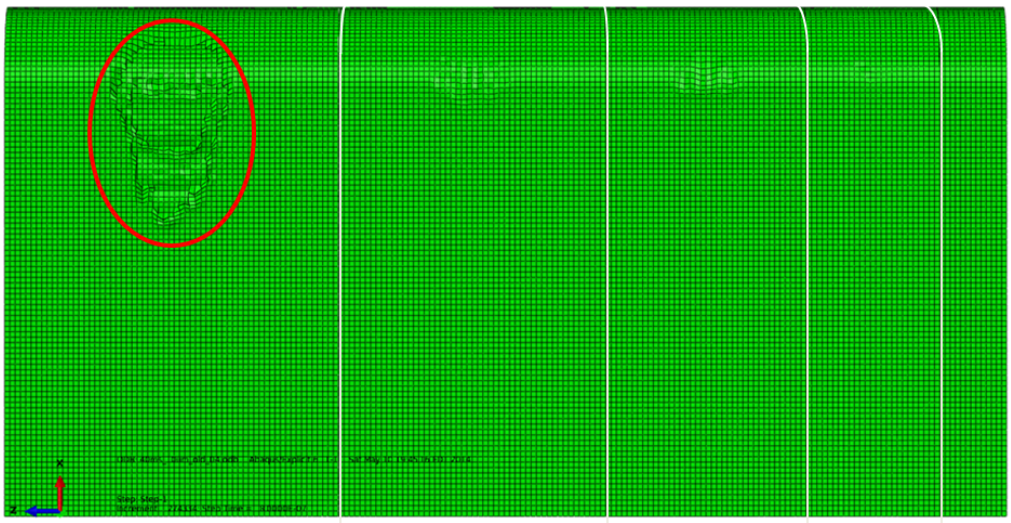

Figure A.23: Original Wear Pattern For 40 m s^{-1}, 1.0 µm Gap, and Fine Mesh

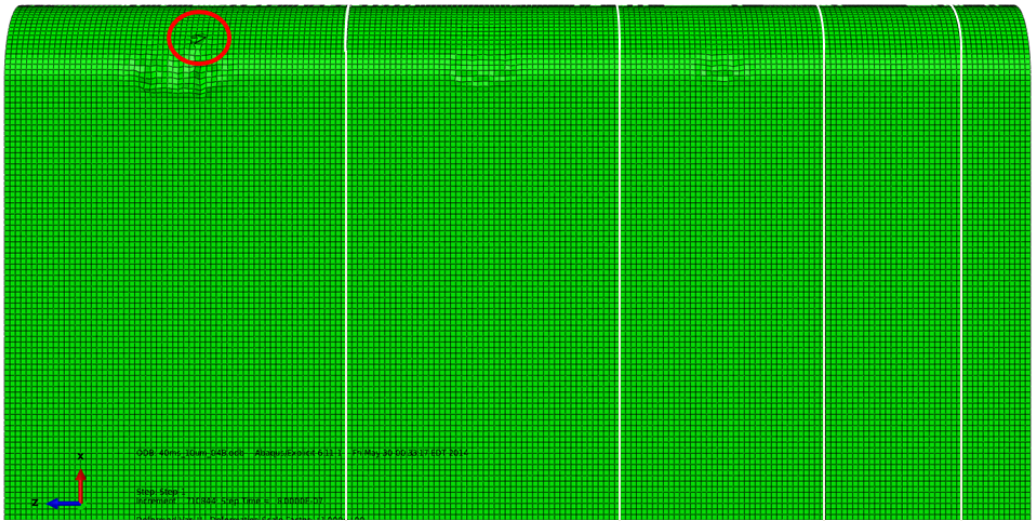

Figure A.24: Baker Wear Pattern For 40 m s^{-1}, 1.0 µm Gap, and Fine Mesh

The interval wear volumes (total wear) for the Baker model can be found in Table A.1 below. It is interesting to note that the original model predicted interval wear volumes of 36.1 mm^3, 8.8 mm^3 and 16.5 mm^3 for the three gap spacings of 1.5 µm, 1.0 µm and 0.5 µm, respectively at 40 m s^{-1}. The Baker model's wear prediction is much lower than the original

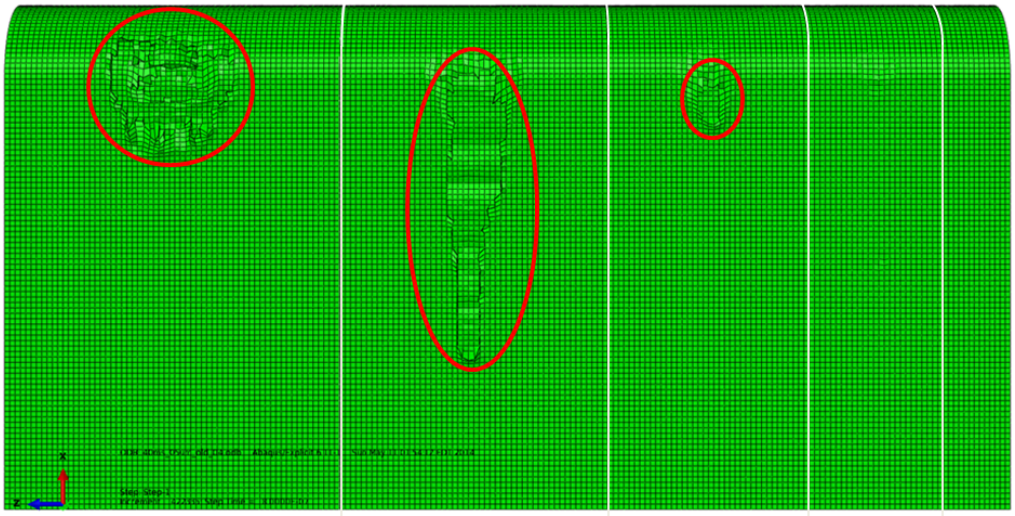

Figure A.25: Original Wear Pattern For 40 m s^{-1}, 0.5 µm Gap, and Fine Mesh

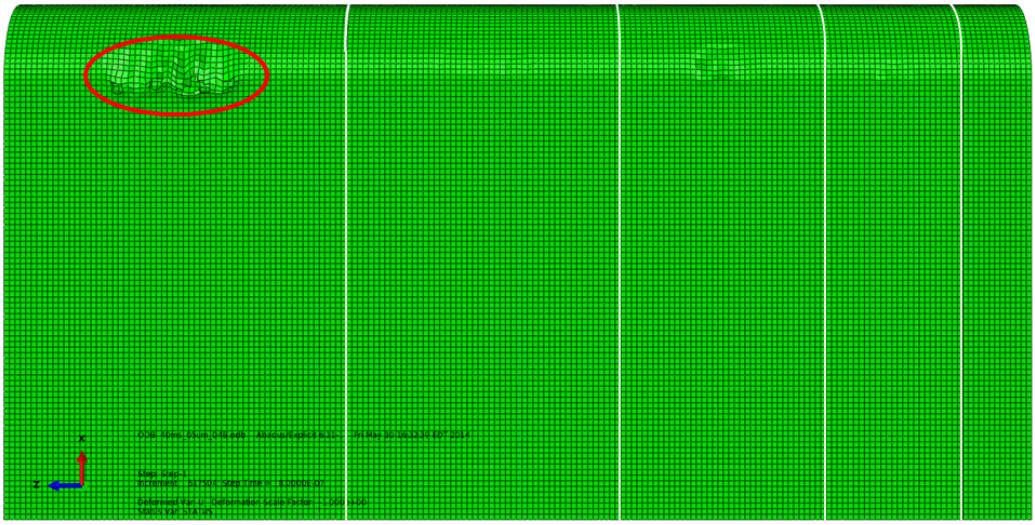

Figure A.26: Baker Wear Pattern For 40 m s^{-1}, 0.5 µm Gap, and Fine Mesh

model. This result allowed for an even lower bound on the low speed regime wear damage from the 1.0 µm gap spacing in this model.

Table A.1: Baker-Cavallaro Model Interval Wear Volumes (mm^3)

Gap Spacing		
1.5 μm	1.0 μm	0.5 μm
0.40	0.02	0.35

This frame images show the elements stretching many times their original length highlights an important area that requires more work. The stretching of the elements can be easily seen in the splinters of asperity material in Figures A.16 and A.18. This feature in the asperity behavior indicates that a mesh refinement, beyond what has been done herein, is necessary.

Bibliography

[1] *Abaqus/CAE User's Manual 6.11*.

[2] "AISI 1080 Steel, annealed at 790C (1450F), furnace cooled 11C (20F) per hour to 650C (1200F), air cooled, 25 mm (1 in.) round". Web Site, 2014. URL http://www.matweb.com/search/datasheet.aspx?matguid=e5ec3009558b4165bfb0c4463434d064&ckck=1.

[3] A. Lodygowski, B. Deliktas A. Palazotto, G.Z. Voyiadjis. "Non-local and numerical formulations for dry sliding friction and wear at high velocities". *International Journal of Plasticity*, 27:1004–1024, 2011.

[4] Archard, J. F. "Contact and Rubbing of Flat Surfaces". *Journal of Applied Physics*, 24(8):981988, 1953.

[5] Archard, J. F. *Elastic Deformation and the Laws of Friction*. 1957.

[6] Bhushan, Bharat. *Introduction To Tribology*. John Wiley & Sons, Inc., 2002.

[7] Bowden, F.P. and D. Tabor. *The friction and lubrication of solids*. Oxford, Clarendon Press, 1950.

[8] Braun, O.M. and A.G. Naumovets. "Nanotribology: Microscopic Mechanisms of Friction". *Institute of Physics, National Academy of Sciences of Ukraine*, 2005.

[9] Fischer-Cripps, Anthony C. *Nanoindention*. Springer, 2011.

[10] Gregory J. Cameron, USAF, Captain. *AN EVALUATION OF HIGH VELOCITY WEAR*. Master's thesis, AIR FORCE INSTITUTE OF TECHNOLOGY, 2007.

[11] Hale, Chad. S. *CONSIDERATION OF WEAR RATES AT HIGH VELOCITY*. Ph.D. thesis, AIR FORCE INSTITUTE OF TECHNOLOGY, 2010.

[12] Hall, A. M. and C. J. Slunder. *THE METALLURGY, BEHAVIOR, AND APPLICATION OF THE 18-PERCENT NICKEL MARAGING STEELS*. Technical report, Battelle Memorial Institute under contract for NASA, 1968.

[13] HHSTT. "U.S. Air Force Fact Sheet: 846 TS - THE NEED FOR SPEED". URL http://www.holloman.af.mil/library/factsheets/factsheet_print.asp?fsID=11723&page=1.

[14] Huber, David A. *The use of various failure criteria as applied to high speed wear*. Master's thesis, AIR FORCE INSTITUTE OF TECHNOLOGY, 2011.

[15] J. D. Cinnamon, Z. Kennan, A.N. Palazotto. "Material characterization and development of a constitutive relationship for hypervelocity impact of 1080 Steel and VascoMax300". *International Journal of Impact Engineering*, 33:180–189, 2006.

[16] Johnson, Gordon R. and W.H. Cook. *A Constitutive Model and Data for Metal Subjected to Large Strains, High Strain Rate and High Temperatures*. Technical report, Honywell Inc, 1983.

[17] Johnson, Gordon R. and William. "FRACTURE CHARACTERISTICS OF THREE METALS SUBJECTED TO VARIOUS STRAINS, STRAIN RATES, TEMPERATURES AND PRESSURES". *EngineeringFracture Mechanics*, 21:31–48, 1985.

[18] Johnson, G.R. and T.J. Holmquist. *Test Data and Computational Strength and Fracture Model Constants for 23 Materials Subjected to Large Strains, High Strain Rates, and High Temperatures*. Technical report, Los Alamos National Laboratory, LA-11463-MS, 1989.

[19] J.T. Burwell, C.D. Strang. "On the Empiracal Law of Adhesive Wear". *Applied Physics*, 23:18–28, 1952.

[20] Kathleen H. Le, USAF, Captain. *A STUDY OF THE THERMAL ENVIRONMENT DEVELOPED BY A TRAVELING SLIPPER AT HIGH VELOCITY*. Master's thesis, AIR FORCE INSTITUTE OF TECHNOLOGY, 2013.

[21] Laird, D. J. *The Investigation of Hypervelocity Gouging*. Ph.D. thesis, Air Force Institute of Technology, 2002.

[22] Lim, S. C. "Recent developments in wear-mechanism maps". *Tribology International*, 31:1–3, 1998.

[23] Lim, S. C. and M. F. Ashby. "WEAR-MECHANISM MAPS". *Acta Metall*, 35:1–24, 1987.

[24] Makoto Okada, Vikas Prakash Kazuhisa Miyoshi, Nai-Shang Liou. "Tribology of high-speed metal-on-metal sliding at near-melt and fully-melt interfacial temperatures". *Wear*, 249:672–686, 2001.

[25] Maneesh Mishra, Roland Bennewitz, Philip Egberts and Izabela Szlufarska. "Friction model for single-asperity elastic-plastic contacts". *PHYSICAL REVIEW*, B86:045452: 1–8, 2012.

[26] Meyers, Marc A. *Dynamic Behavior of Materials*. John Wiley & Sons, Inc., 1994.

[27] Montgomery, R. S. "Friction and Wear at High Sliding Speeds". *Wear*, 36:275–298, 1976.

[28] Pil-Ryung Cha, David J. Srolovitz and T. Kyle Vanderlick. "Molecular dynamics simulation of single asperity contact". *Acta MATERIALIA*, 52:3983–3996, 2004.

[29] Quinn, Terence F. J. *Physical Analysis for Tribology*. Cambridge University Press, 1991.

[30] Rodolfo G. Buentello-Hernandez, USAF, Major. *3D Finite Element Modeling Of Sliding Wear*. Ph.D. thesis, Air Force Institute of Technology, 2013.

[31] Voyiadjis, A. Lodygowski, G.Z. and B. Deliktas. *Non-Local Coupling of Friction and Damage I High Velocity Wear*. Technical report, Louisiana State University, 2009.

[32] Wedberg, Dan. *Modelling of High Strain Rate Plasticity and Metal Cutting*. Ph.D. thesis, Lulea University of Technology, 2013.

[33] Wolfson, M. R. *Wear, Solid Lubrication, and Bearing Material Investigation for High-Speed Track Applications.* Technical report, Test Track Division, Air Force Missile Development Center, Holloman AFB, New Mexico, 1960.

REPORT DOCUMENTATION PAGE

Form Approved
OMB No. 0704–0188

1. REPORT DATE *(DD–MM–YYYY)*	2. REPORT TYPE	3. DATES COVERED *(From — To)*
19–06–2014	Master's Thesis	Aug 2012–Jun 2014

4. TITLE AND SUBTITLE

A Study of Slipper and Rail Wear Interaction at Low Speed

5a. CONTRACT NUMBER

5b. GRANT NUMBER

5c. PROGRAM ELEMENT NUMBER

6. AUTHOR(S)

Cavallaro, Greg V., Major, USAF

5d. PROJECT NUMBER

5e. TASK NUMBER

5f. WORK UNIT NUMBER

7. PERFORMING ORGANIZATION NAME(S) AND ADDRESS(ES)

Air Force Institute of Technology
Graduate School of Engineering and Management (AFIT/EN)
2950 Hobson Way
WPAFB, OH 45433-7765

8. PERFORMING ORGANIZATION REPORT NUMBER

AFIT-ENY-T-14-J-31

9. SPONSORING / MONITORING AGENCY NAME(S) AND ADDRESS(ES)

Dr. Michael Kendra
Program Officer, Test and Evaluation
Air Force Office of Scientific Research
875 N. Randolph St., Suite 325
Arlington VA 22203

10. SPONSOR/MONITOR'S ACRONYM(S)

11. SPONSOR/MONITOR'S REPORT NUMBER(S)

12. DISTRIBUTION / AVAILABILITY STATEMENT

DISTRIBUTION STATEMENT A:
APPROVED FOR PUBLIC RELEASE; DISTRIBUTION UNLIMITED

13. SUPPLEMENTARY NOTES

14. ABSTRACT

The wear research presented in the work consists of results gathered from adapting a FEM based on a Holloman High Speed Test Track (HHSTT) mission executed in January 2008. The FEM consists of a VascoMax slipper sliding on a stationary AISI-1080 steel rail. The slipper is slid along the rail at speeds of 20 m/s and 40 m/s with complementary vertical velocities of -0.079 m/s and -0.059 m/s, respectively. The surface roughness caused by features such as asperities and valleys of the materials, is simulated in this model by five asperities, $1\,\mu m$ to $5\,\mu m$ on the rail and a slipper with a leading edge radius of $6\,\mu m$. The free space between the surfaces, caused by the interaction of the asperities and valleys, is approximated by three gap spacings of $0.5\,\mu m$, $1.0\,\mu m$, and $1.5\,\mu m$. This study also explores three different Mesh refinements in the wearing portion of slipper to uncover any mesh dependence affecting the amount of wear. Additional simulations were completed to highlight the effects of using more accurate material definitions, tables of specific heat capacities were used instead of static values and more applicable, lower strain rate Johnson Cook plasticity parameters were. In a final three simulations, asperities with a smooth root fillet are used to highlight the model behavioral differences due to this simple change.

15. SUBJECT TERMS

Wear Modeling, Abaqus, VascoMax, Holloman High Speed Test Track, wear rate, mechanical wear

16. SECURITY CLASSIFICATION OF:			17. LIMITATION OF ABSTRACT	18. NUMBER OF PAGES	19a. NAME OF RESPONSIBLE PERSON
a. REPORT	b. ABSTRACT	c. THIS PAGE			Dr. Anthony. N. Palazotto
U	U	U	UU	114	19b. TELEPHONE NUMBER *(include area code)* 937-255-3636, ext 4599